



UNIVERSITÀ DEGLI STUDI DI ROMA “TOR VERGATA”

FACOLTÀ DI SCIENZE MATEMATICHE FISICHE NATURALI
DIPARTIMENTO DI FISICA
DOTTORATO DI RICERCA IN ASTRONOMIA
CICLO XXII

X-ray overview of INTEGRAL Blazars

Silvia Gianni

A. A. 2009/2010

Tutori:

Dr. Angela Bazzano

Coordinatore:

Prof. Pasquale Mazzotta

Dr. Alessandra De Rosa

Contents

1	Active Galactic Nuclei	6
1.1	Introduction	6
1.2	General properties	8
1.3	Unification model	10
1.4	Classification	13
1.5	Spectral Energy Distribution (SED)	16
1.6	The X-ray spectrum: features and physical interpretation	20
1.7	Why is the study in the X-ray energy range important?	23
2	Blazars	25
2.1	Introduction	25
2.2	The Blazar peculiarities	26
2.3	The Blazars spectral features and radiative processes	27
2.4	Open questions	31
2.5	Aim of this work: a broad-band study of Blazars	33
3	INTEGRAL: INTErnational Gamma Ray Astrophysical Laboratory	35
3.1	Introduction	35
3.2	The INTEGRAL mission: an overview	35
3.3	The INTEGRAL Observatory	36
3.3.1	Observing modes	37
3.4	The instruments on-board INTEGRAL	38
3.4.1	Coded mask telescopes	38
3.4.2	The gamma-ray imager IBIS	40
3.4.3	The spectrometer SPI	42
3.4.4	The X-ray monitor JEM-X	43
3.4.5	The optical monitor OMC	43
3.5	A comparison with some X-ray detectors	44
4	Broad-band study of the Blazars observed with INTEGRAL	50
4.1	Introduction	50
4.2	The INTEGRAL/IBIS selected sample	50

4.3	The hard X-ray data reduction	53
4.3.1	The INTEGRAL/IBIS and Swift/BAT data	53
4.4	The soft X-ray data reduction	53
4.4.1	The XMM-Newton and Swift/XRT data	53
4.5	The XMM and XRT timing analysis	56
4.6	Broad-band spectral analysis: 0.2 – 100 keV	59
4.7	Parameter distributions and correlations	73
4.7.1	Absorption column density distribution	74
4.7.2	Photon-index distribution	77
5	Discussion	81
5.1	Introduction	81
5.2	Absorption properties	81
5.3	Emission properties	84
5.3.1	The case of 4C 04.42	86
5.3.2	The case of 3C 273	87
5.4	Compton Reflection features and the analysis of the variability	88
5.5	Conclusions	88
5.6	Future developments	90

Abstract

Radio Loud (RL) quasars represent a small percentage ($\sim 10\%$) of all Active Galactic Nuclei (AGN) with a strong radio emission. We aimed to study the X-ray and hard X-ray emission from a subclass of these objects: the Blazars. The Blazar objects are AGNs with a jet of plasma (largely formed by electrons and protons) emitting at low angles with respect the line-of-sight. This class of AGN include BL Lacertae objects (BL Lac) and Flat-Spectrum Radio Quasars (FSRQ). The intrinsic differences between two types of sources are been found in their optical spectra and in the intensity of their emission: a BL Lac source does not show any optical emission lines ($EW < 5\text{\AA}$) and this class of objects is essentially a low-power blazar ($L_{Bol} \sim 10^{46} - 10^{47} \text{ erg s}^{-1}$), whereas a FSRQ source shows significant emission line equivalent widths and corresponding to a high-power blazar ($L_{Bol} \sim 10^{48} \text{ erg s}^{-1}$).

In general, the spectrum of an AGN in the X-rays band is usually well described by a power-law with a specific flux (i.e. per unit energy interval) of the form $N(E) \propto E^{-\Gamma}$, where E is the energy, N(E) is the number of photons in units of $\text{s}^{-1} \text{ cm}^{-2} \text{ keV}^{-1}$ and Γ is called the *photon index*.

Despite this general view, X-ray spectra of the Blazars show some deviations from the simple power-law. These spectral signatures appear in the soft X-ray band with a curvature (a flattening or a steepening of the spectrum). In addition, the presence of Compton reflection components - most notably the Fe K-alpha emission line and the Compton reflection "hump" peaked at about 20 – 30 keV - in RL objects is still debated. To date a clear physical interpretation of these features has not yet been found.

We report in this work the results of a broad-band (0.2 – 100 keV) study of X-ray emission from a selected sample of 11 Blazars detected by INTEGRAL: 1ES 0033+595, 3C 273, 3C 279, 4C 04.42, BL Lac, IGR J22517+2218, PKS 0537-286, PKS 1830-211, PKS 2149-306, QSO B0836-710 and Swift J1656.3-3302. The INTEGRAL observatory, because of the large field of view and high spectral resolution of its instruments, is ideal to study the high energy emission (above 10 keV).

Present PhD work was aimed to the investigation of this hard X-rays selected sample, by taking advantage of the availability of the INTEGRAL, Swift and XMM-Newton data. After data reduction procedure, we performed a detailed temporal and spectral analysis for all sources in the sample.

The scientific results can be summarized as follows:

- the broad-band spectra of all selected sources - but two, the FSRQs 4C 04.42 and 3C 273 - are well reproduced with a power-law model absorbed by an amount of gas in excess to the Galactic one ($N_H \sim 10^{20} - 10^{23} \text{ cm}^{-2}$). This result provides plain evidence to the fact

that by using the INTEGRAL high-energies data the highly absorbed sources can be more easily detected. Moreover, the absorption seems to be a signature of a cold intrinsic absorber, confirming and extending previous results quoted in the literature. Present work provides a further confirmation of the existence of a N_H -redshift trend;

- with regard to continuum emission we found that the broad-band analysis of our sample of Blazars revealed a harder spectrum with a photon-index of the order of $\Gamma \sim 1.4$, with respect to the mean value of the spectral index obtained by Page et al. (2005) with XMM data of a statistically sizeable sample of RL objects. Such a difference could be due to the hard X-ray selection of our INTEGRAL sample that is clearly biased towards flatter values of the photon index as shown by previous results;
- in our analysis we have find two case (4C 04.42 and 3C 273) of excess of soft X-ray counts with respect to the simple power-law model (in other words a steepening of the spectrum), indicating the possible presence of a soft X-ray emission;
- we have not found any evidence of reflection components (Reflection "hump" and iron emission line).

The thesis structure is as follows:

In Chapters 1 and 2 we summarize the observational properties common to all AGN subclasses emphasizing in particular the Blazar class), we give a general description of their spectral energy distribution and then we discuss their emission mechanisms in the high energy band and the open questions related to the spectra of the RL objects.

In Chapter 3 we deal with the INTEGRAL mission overview and a comparison with some X-ray detectors such as, Swift/BAT, Swift/XRT and XMM-Newton.

In Chapter 4 we report on the data reduction method and analysis of the Blazar selected sample.

Finally, in Chapter 5 we discuss the results and give our conclusions.

Chapter 1

Active Galactic Nuclei

1.1 Introduction

Astronomers have been aware of the existence of *Active Galactic Nuclei* (commonly abbreviated as AGN) since the beginning of the 20th century, even though they could not recognize them as such. At that time their extragalactic nature was unknown, as it was for galaxies in general which were called nebulae.

Before discussing the historical evolution of our knowledge of these astrophysical objects, it is worth emphasizing that the objects of this class can have very different emission properties, however, they all share a striking characteristic which distinguishes them from all the other galaxies in the Universe: the emission from the nucleus largely outshines that of the whole galaxy. So AGNs are among the most powerful sources of energy in the Universe and they shine over the whole electromagnetic spectrum, from the radio to the gamma rays and in almost all of this huge energy range, AGN are the brightest sources in the sky.

It is quite important to note that the choice of the definition ‘*Active Galactic Nucleus*’ is due to the empirical evidence that the activity of these objects is mainly confined in the central regions.

The starting date of the observational study of AGN may be set in 1908 thanks to the work of E. A. Fath on spiral nebulae. These objects showed absorption lines in their optical spectra and, since the same lines had also been observed in star clusters, their emission was interpreted analogously in terms of the integrated light from a large number of stars, too distant to be resolved individually. However, one nebula, NGC 1068, revealed some high-ionization emission lines in its optical spectrum.

Later, in 1943, Carl Seyfert discovered that these emission line objects constituted a small fraction of the galaxies in general. He also argued that they showed emission lines wider than the absorption lines in normal galaxies, with a wide range of ionization, originating in a small, bright nucleus of

stellar appearance in the host galaxy. The discovery of these AGNs traditionally dates back to this work and they were thus called *Seyfert galaxies* ever since.

Radio galaxies have been known since the mid-1950s when the *Third Cambridge Catalog* (3C) was created. Cygnus A was the first detected radio source outside the solar system, however, its optical identification with an elliptical galaxy had to wait until 1954 (Baade & Minkowski 1954) followed by the identification of other strong radio sources soon after.

In 1962 a lunar occultation of the radio source 3C 273 allowed an accurate determination of its radio position and consequently the identification of its optical counterpart. This turned out to be of stellar-like appearance, but its optical spectrum contained several strong emission lines unlike stellar spectra where only absorption lines are detected. For this reason 3C 273 and similar objects were called *quasars* which stands for *quasi-stellar radio sources* (*QSR*).

It was only in 1963 that quasars spectra were interpreted in terms of cosmological redshift by Maarten Schmidt who identified the lines observed in 3C 273 as Hydrogen Balmer lines severely redshifted ($z=0.158$). So these objects were recognized to be extragalactic, at extremely large distances from our Galaxy (Schmidt 1963). Moreover, since, at such distances, even the brightest normal galaxies would not be visible, this led to conclude that quasars had luminosities never seen before (~ 100 times larger than a bright spiral galaxy). Later on, with the discovery of many stellar-like objects, which lacked strong radio emission, it was understood that this is not a general feature of quasars, but only for about the 10 - 15% of them.

The new objects were named *Quasi-Stellar Objects* (*QSO*), a term used for radio-quiet¹ and radio-loud quasars, which differ for their radio emission. The terms *radio-loud* and *radio-quiet quasars* are used when an explicit distinction is necessary.

With the advent of the Einstein Observatory in 1980 it was realized that a general feature of quasars is their X-ray emission and that this waveband carries useful information on the energy production mechanisms, on the circumnuclear matter and on the internal structure of AGN.

A final remark is necessary on *BL Lac objects*, the most peculiar members of the AGN class, characterized by lack of strong emission or absorption lines. BL Lacertae (or BL Lac) was at first believed to be a variable star in the constellation of Lacerta due to its stellar appearance. In 1968 its radio counterpart was found (MacLeod & Andrew 1968, Schmidt 1968) and in 1969 the optical continuum was found to be featureless without either emission or absorption lines (Visvanathan 1969). Together with its variability and high degree of polarization, this established the unusual nature of

¹For a quantitative definition of radio-loudness see section 1.4.

BL Lac. In 1974 Adams identified a faint nebulosity around it with color and brightness distribution consistent with that of an elliptical galaxy, thus proving its extragalactic nature. When similar sources were discovered afterwards they inherited the name BL Lac objects from it.

As far as it concerns the interpretation of the ‘phenomenon’ AGNs, only in relatively recent years attempts have been made to unify them in a coherent picture (see section 1.3). According to this unified view all AGN subclasses share a common mechanism of energy production, the accretion of matter onto a supermassive black hole in their center. Their different observational properties arise, to a large degree, from their intrinsically anisotropic geometry and radiation pattern, from absorption as well as from relativistic effects.

In this chapter we will describe the observational properties common to all AGN subclasses, then we will treat in detail the properties of each subclass and the related AGN taxonomy, we will briefly summarize the historical background concerning the discovery and the study of AGN and, finally, we will give a general description of the spectral energy distribution of an AGN and we will discuss the emission mechanisms in each band.

1.2 General properties

The separately discovered types of AGN actually share some remarkable properties which eventually led to grouping them together into a common class. In the following we list these general properties and discuss them briefly.

The first remarkable property of all AGN is the emission of radiation over the entire electromagnetic spectrum with bolometric luminosities $L \geq 10^{44}$ erg s⁻¹, sometimes reaching $L \sim 10^{47} - 10^{48}$ erg s⁻¹. In comparison, normal galaxies have $L \leq 10^{42}$ erg s⁻¹ and the bulk of their luminosity is emitted in the visible band, essentially produced by stars.

The second remarkable property is the high variability of their emission observed at all frequencies (e.g. Mushotzky, Done & Pounds 1993), on time scales ranging from years down to hours. Such short time scales imply that the region from which the luminosity is emitted is very compact. If R is the linear dimension of this region and Δt_{var} is some characteristic variability timescale, a simple light travel time argument demands that $R \leq c\Delta t_{var}$ for the variability to be observed (where c is the speed of light). From the measured Δt_{var} in AGN it is usually found that $R \leq 0.1pc$, i.e. the emission region is contained well within the nucleus of the galaxy (a fact that justifies the name of AGN).

The spectra of AGN over the whole electromagnetic band are essentially

of non-thermal origin (however, see also the section on the SED of AGN), contrary to normal galaxies where the spectrum is given by the integration of the stars thermal spectra. In a given waveband the AGN spectra can usually be well described by a power law with flux density or specific flux (i.e. per unit frequency interval) of the form $f(\nu) \propto \nu^{-\alpha}$ usually measured in units $\text{erg s}^{-1} \text{cm}^{-2} \text{Hz}^{-1}$ where α is called the *spectral index*. An equivalent parameterization of the spectrum of an AGN, preferred at high energies, is given by $N(E) \propto E^{-\Gamma}$, where E is the energy, $N(E)$ is the number of photons in units of $\text{s}^{-1} \text{cm}^{-2} \text{keV}^{-1}$ and Γ is called the *photon index*. The spectral index is related to the photon index by $\Gamma = \alpha + 1$.

Together with the non-thermal continuum, the optical spectrum of an AGN usually shows strong emission lines. Both permitted and forbidden narrow emission lines are observed, whereas only permitted broad emission lines have been seen. The widths of the emission lines yield information on the velocity properties of the emitting material. Interpreting the line widths in terms of Doppler broadening, velocity dispersions of the order of $\sigma \sim 300 - 400 \text{ km s}^{-1}$ are found in the case of narrow lines and an order of magnitude higher, i.e. $\sigma \sim 3000 - 4000 \text{ km s}^{-1}$, for the broad lines (Peterson 1993).

Some AGN also reveal strong radio emission in the form of spectacular jets and extended lobes (e.g. Urry & Padovani 1995). These radio structures can reach distances from the center of the AGN of the order of $\sim 100 \text{ kpc}$ up to $\sim 1 \text{ Mpc}$, well beyond the optical extension of the host galaxy. However, the majority of AGN seem to be radio-quiet.

All properties listed above are indicators of powerful physical mechanisms acting at the centers of active galaxies producing such highly energetic phenomena in a very compact region. Clearly, nuclear processes in the cores of stars cannot account for the enormous AGN energy output and in section 1.5 the current model for the central engine of an AGN will be discussed.

The fraction of galaxies which show these peculiar properties is only $\sim 1\%$ of the total population and only $\sim 0.1\%$ has jets and a still smaller fraction of them has jet directed close to the line of sight. However, they are outstanding and intriguing objects providing insight into yet unexplored physical processes. As extremely luminous and distant objects they are also unique probes of the Universe at early stages and thus useful cosmological tools.

A key question regarding the galaxy evolution is: does every galaxy pass through an activity phase or can only a small fraction of galaxies become active, for example due to special environmental conditions?

In the following section we will give a unification scheme, which relates the observed properties to both geometrical and physical causes, while in

the section 1.4 a more detailed classification scheme for the AGN, based on their observed radio and optical properties and useful to understand the AGN terminology, will be presented.

1.3 Unification model

Any model for the AGN must be able to explain the peculiar properties discussed in the previous paragraph. The fundamental question is: what kind of source is capable to produce such a large amount of energy from such a compact region?

Initially, astronomers tried to explain the AGN energy source in terms of very massive stars evolving into super-supernovae, populations of massive O stars, and collections of supernovae. All these scenarios failed to account for the high emission efficiency implied by the AGN luminosity. In fact, any spherical object held together by gravitational forces must radiate below a well defined luminosity limit dependent on its mass, called the Eddington luminosity. Beyond the Eddington limit the radiation pressure would be larger than the gravitational force and the object would be disrupted.

The Eddington limit is obtained imposing the equilibrium between the gravitational force acting on the protons (neglecting the small contribution from the electrons) and the radiation pressure acting on the electrons (assuming that the interaction between the radiation and the protons is negligible). This yields:

$$L \leq L_E = \frac{4\pi c G m_H M}{\sigma_T} = 1.26 \times 10^{38} M/M_\odot \quad (1.1)$$

where σ_T is the Thomson cross section. For a typical AGN luminosity of $10^{12} L_\odot$ ($\sim 4 \cdot 10^{45}$ erg s^{-1}) this implies a lower limit for the mass of the star of $M \geq 3 \times 10^7 M_\odot$. If we write for the AGN luminosity:

$$L = \epsilon M c^2 \Delta t^{-1} \quad (1.2)$$

where ϵ is the efficiency of the energy production mechanism, $\Delta t \sim 10^8$ yrs is the typical lifetime of an AGN and we take $L \approx L_E$, substituting Eq. 1.1 into Eq. 1.2, we get $\epsilon \approx 0.4$, independent of the AGN mass.

This value largely exceeds that for thermonuclear processes in stars (Fabian 1979) and demands other mechanisms for the energy production. In 1963 Hoyle & Fowler proposed that the energy source in AGN was of gravitational origin from the collapse of very massive objects in analogy to what happens in the early stages of star formation. Later on this idea was developed into the so called black hole-accretion disk paradigm which was already working well for the X-ray binaries in our Galaxy (e.g. Rees 1984).

According to this model the core of an AGN is a Super Massive Black Hole SMBH ($M_{BH} \sim 10^6 - 10^9 M_{\odot}$) onto which matter is accreted by its strong gravitational force.

Because of angular moment conservation, the falling material creates an accretion disk around the black hole which radiates and converts gravitational potential in thermal energy. It is thought that it is the high efficiency (from the general relativity it is known that the efficiency of such a mechanism can be $\sim 10\%$ in the case of a Schwarzschild black hole) of the conversion of matter in energy in this accreting mass process that enables the AGNs to produce extraordinary large luminosities (until $10^{47} \text{ erg s}^{-1}$) inside small volumes (within a sphere whose radius is equal to about $10 R_G$, that corresponds to $5 \times 10^{-5} \text{ pc}$ for a black hole with mass of $10^8 M_{\odot}$, where R_G is the gravitational radius² of the black hole).

Assuming the geometrically thin, optically thick disk model proposed by Shakura (1973), each element of the disk face radiates roughly as a black-body and the total emission, extended from the optical to the X-ray band, is a convolution of black-body spectra with different temperatures, emitted at different radii.

Since the gravitational force by the central black hole with mass M , acting on the gas falling onto the central engine, must balance or exceed the outward radiation force, one can link the luminosity L emitted by the central engine to its mass M . Under the hypothesis of a spherical symmetry from relation 1.1, a lower limit on the mass of the hypothetical SMBH is obtained considering that the AGN is emitting light at the Eddington limit, i.e. the limit where the radiative pressure is balancing the gravitational potential: $M \geq 8 \times 10^5 L_{44} M_{\odot}$, where L_{44} is the luminosity in units of $10^{44} \text{ ergs}^{-1}$, typical value for a luminous Seyfert galaxy. For a typical quasar with luminosity $L \sim 10^{46} \text{ ergs}^{-1}$, a central mass of $10^8 M_{\odot}$ is required. We remark that there is mounting evidence for the existence of supermassive black holes at the center of many normal galaxies (Kormendy & Gebhardt 2001, Richstone 2002 and Schödel et al. 2002 for the Galactic center) providing experimental support to this scenario.

Besides the central SMBH and the surrounding accretion disk, there are also massive gas clouds located at larger distances, which move quickly in the potential hole of the black hole. These clouds are colliding with the radiation coming from the accreting disk and produce the strong emission lines characteristic of the AGN spectrum, mainly through photo-ionization processes and excitation via collisions.

The clouds, located close by to the central source (within 0.001 - 1 pc) are denser (usually in the density range $n \approx 10^8 - 10^{12} \text{ cm}^{-3}$) and move faster. These clouds are responsible for the production of the wide emission

²The gravitational radius or Schwarzschild's radius is a characteristic radius associated to every mass and it is defined as: $R_G = 2GM/c^2$.

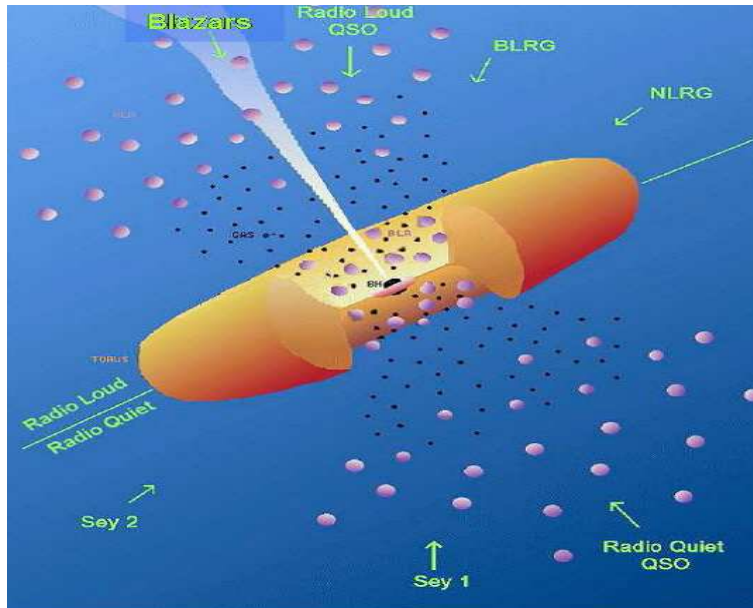


Figure 1.1: Modified figure, corresponding to the scheme of an AGN, as taken from Urry & Padovani 1995. The radio lobes are not shown in this picture.

lines (with typical widths of the order of several thousands km s^{-1}) in the spectrum in the UV/optical band, which are usually associated with allowed transitions. The most important lines are hydrogen lines of the Balmer and Lyman series and the transitions of carbon and magnesium ions. These clouds are commonly named as the broad-line region (BLR) with a typical FWHM larger of $1000 - 2000 \text{ km s}^{-1}$, and a maximum FWHM of about 10000 km s^{-1} .

The farthest gas clouds (located until some kpc; e.g. Schmitt & Kinney 1995; Bennert et al. 2002) are characterized by a lower velocity and density (n equal to $\approx 10^3 - 10^6 \text{ cm}^{-3}$). They originate the narrow emission lines (with widths of the order of several hundred km s^{-1}), and form the so-called narrow-line region (NLR). These lines have a typical FWHM lower to about $1000 - 2000 \text{ km s}^{-1}$. They are associated to both allowed and forbidden transitions. The stronger transitions among the forbidden ones, are those associated with ionized oxygen and neon.

Due to the evidence that wide emission lines are not observed in all AGNs, whereas the narrower ones are almost universally present, it is commonly hypothesized the presence of a dusty torus with inner radius of the order of $\sim 10^{17} \text{ cm}$. It is assumed that the dusty torus is located outside the accretion disk, surrounds the BLR and obscures it for some orientations of the line-of-sight. A strong empirical evidence of the existence of the dusty torus comes from the direct observations of polarized wide emission lines in the polarized light emitted by several AGNs (Antonucci & Miller 1985;

Cohen et al. 1999; Lumsden et al. 2001).

However, as we have mentioned in section 1.2, in some objects, defined as radio-loud sources, it is observed the additional presence of a relativistic jet, with a direction almost perpendicular to the accretion disk. This jet produces a strong anisotropy, polarization and amplification of the emission flux in the continuum ('relativistic beaming'). These jets are blobs of plasma (probably largely formed by electrons and protons) which are beamed and accelerated by a strong electromagnetic field. As a consequence, they irradiate energy via Synchrotron processes. The radio jets emit from regions near to the central black hole and fuel extended lobes until quite large distances (until several hundredths of kpc) from both sides with respect the central source. In fact, the radio jets can extend up to 0.1 – 1 Mpc, well outside the size of the optical galaxy.

The several components of the unification scheme for an AGN are shown in Figure 1.1 and an exhaustive review is provided, for example, by Urry and Padovani (1995).

1.4 Classification

At the first order, the classification of AGNs is made according to their intrinsic luminosity: the intrinsically brighter sources are called Quasars, while the fainter ones are named Seyfert.

In the optical the conventional dividing line between Seyfert and Quasars is defined as $M_B = -21.5 + 5 \cdot \log h_0$, where h_0 is the Hubble constant in unit of $100 \text{ km s}^{-1} \text{ Mpc}^{-1}$. In the case of the Seyfert objects, the total energy emitted by the compact central source is comparable with that of the stellar population in the parent galaxy, whereas for the Quasars the total energy produced in the optical band by the central source is at least 2 orders of magnitude larger than that associated to the stellar component in the host galaxy.

In order to properly understand the various physical mechanisms at work in an AGN, as well as their relative contribution, a preliminary step has been to provide a suitable classification of the AGNs on the basis of the observed properties of their optical and radio spectra.

The first basic classification is made according to the observed differences in the optical spectra, regardless of the observed radio spectrum. More in detail, AGN with a bright continuum and both broad and narrow emission lines are called *type 1 AGN* (or BLR Galaxies), those with a weak continuum and only narrow emission lines are called *type 2 AGN* (or NLR Galaxies).

It is currently believed that the quoted differences in the optical spectrum can be largely interpreted as due to orientation and obscuration effects. In fact, the dependence of the outcoming properties of an AGN on the viewing angle - see the previous discussion on the relative location of the dusty torus

	Type 2 (narrow lines)	Type 1 (broad lines)	Type 0 (a-typical)
RADIO QUIET	SEYFERT 2 LINER	SEYFERT 1 QSO	BAL QSO
RADIO LOUD	NLRG	BLRG FSRQ SSRQ	BL LAC

Figure 1.2: Classification scheme for the AGNs based on radio and optical properties.

with respect the regions producing the various types of lines (NLR and BLR) - is used for interpreting the existence of the two different classes of AGNs. More in detail:

- Type 1: At intermediate angles of the line of sight the emerging flux will be affected by absorption in the dusty torus and the radio jet, if present, will not be seen; both NLR and BLR plus optical continuum will be observed, but relativistic beaming effects will not be relevant. In this case the object will be classified as type 1, as BLRG, FSRQ or SSRQ. When the line of sight intercepts the radio jet which is then viewed along its axis, relativistic beaming strongly amplifies the luminosity and produces strong variability, polarization, superluminal motion characteristic of a class of AGN named *Blazar*.
- Type 2: If the viewing angle is large the observers line of sight will intercept the dusty torus and both the optical continuum from the central region and the BLR will be hidden. In this case the object will be classified as type 2 or NLRG;

The second basic classification is made according to the radio spectra. The scheme in Figure 1.2 gives the principal classification of AGN based on radio emission and optical spectral properties. It must be noticed that the X-ray properties of the objects are normally not taken into account for this classification scheme.

The first rough division is made according to the parameter called radio-loudness, defined as:

$$R_L = \log(f_{5GHz}/f_B) \quad (1.3)$$

where f_{5GHz} is the radio flux at 5 GHz and f_B is the optical flux in the B band, centered on the wavelength 4400\AA . These fluxes are in the rest-frame of the object. If an AGN has $R_L \geq 1$ it is conventionally said to be *radio-loud (RL)*, whereas if it has $R_L < 1$ it is said to be *radio-quiet (RQ)* (Kellermann et al. 1989).

The RL objects represent a small percentage ($\approx 10\%$) of all AGN. However, it must be pointed out that the sharp separation into these two classes has been questioned following the results of the FIRST survey (Brinkmann et al. 2000, White et al. 2000). The AGNs could instead follow a continuous distribution in radio-loudness, rather than being sharply divided into two populations. However, it has been argued recently that the lack of a bimodality in radio loudness as inferred from FIRST data could be due to an intrinsic insensitivity of the survey to the extended emission (Laor 2003).

It has been thought for some time that the physical basis for the radio-loud classification was that, whenever the host galaxy could be imaged, radio-quiet AGN were found to reside in spiral galaxies, whereas radio-loud AGN were usually housed by ellipticals. However, HST observations recently allowed the accurate measurement of the AGN host galaxies luminosity profiles (for $z \leq 0.5$), unambiguously revealing that both radio-loud and radio quiet quasars with nuclear $M_V < -23.5$ inhabit massive ellipticals with negligible disc components (Dunlop et al. 2003). The current picture thus appears to be that above a given optical nuclear luminosity threshold AGN can only reside in massive ellipticals regardless of their radio power. At lower optical nuclear luminosities spiral host galaxies become more common within the radio-quiet population, whereas radio-loud AGN are always hosted in ellipticals.

The RL AGNs are commonly divided in two further sub-classes on the basis of the shape of their radio spectrum (according to their radio spectral indices α_r at 5 GHz, see section 1.2): those objects with a flat energy distribution ($\alpha_r < 0.5$) are called *Flat Spectrum Radio Quasars (FSRQ)*, while those with a steep radio spectrum ($\alpha_r > 0.5$) are named *Steep Spectrum Radio Quasars (SSRQ)*.

Currently, FSRQ and BL Lac objects are considered to belong to the same class named *Blazar*. But the characteristic 'featureless' optical spectra of BL Lac, there are no particular differences between BL Lac and FSRQ. Essentially, the BL Lac are low-power Blazars (about $10^{46} - 10^{47} \text{ erg s}^{-1}$), while FSRQ are high-power Blazars (about $10^{47} \text{ erg s}^{-1}$). The evidence that the two kinds of objects are included in the same class is due to the fact that the observational properties of these objects (radio nuclei, flat radio spectra, strong polarization, super-luminary motion, high temperature of brilliance, strong and fast variability) can be explained as the emission of a relativistic plasma moving in the direction of the observer. The word 'Blazar', created by Ed Spiegel in 1978 combining the words BL(Lac) and (Qu)asar, is therefore used for all those AGNs with a jet of plasma emitting

at low angles with respect the line-of-sight.

Now, in the section 1.5, we will treat in more detail the emission properties in different wavebands, i.e. the spectral energy distribution of AGN, in the framework of the unified scheme.

1.5 Spectral Energy Distribution (SED)

AGN are powerful emitters in every energy band of the electromagnetic spectrum, from radio frequencies up to gamma-ray energies. A correct understanding of the AGN physics and a correct estimate of the total emitted power strongly depend on a detailed knowledge of the emission properties in every region of the spectrum. Therefore, it is clear that the availability of high quality, observational data in various spectral bands is of pivotal importance.

Some spectral bands, such as the radio, the optical and the X-rays, are better studied than others. Some wavebands are inaccessible by our instruments, like the extreme UV beyond the Lyman limit of 912 \AA , due to the high opacity of the interstellar medium in our Galaxy. It is obvious that a better knowledge of the multi-wavelength properties is achieved for the brightest AGN, i.e. Blazars.

In the following, we provide a general overview of the spectral properties of AGNs as they are known so far and discuss the physical emission mechanisms contributing in the various bands. Since the analysis of the spectral properties in the X-rays band of a selected sample of AGN is the main subject of present work, a detailed discussion on the features characterizing the SED in the X-rays band, as well as of the contributing physical emission processes will be presented in a specific subsequent section.

The commonly adopted approach for illustrating the multiwavelength energy output of AGN is through the so called Spectral Energy Distribution (SED). It corresponds to a broad band spectrum covering the whole range of frequencies, from radio to gamma-rays, generally represented in a $\log \nu - \log \nu f_\nu$ plot. The main advantage of this diagram is that it approximately shows the energy emitted per unit logarithmic frequency interval (or per decade of frequency), and so it provides the information on the spectral band in which the largest portion of the energy is released.

As far as it concerns the shape of the SED, we can note that there are some striking similarities in the SED of all AGN, but apart from these overall similarities, show some relevant differences. The existence of these differences among the SEDs has been interpreted as the consequence of the orientation and obscuration effects discussed in section 1.4. For the sake of clarity, in the following when discussing the main differences in the SEDs, we roughly distinguish among blazars AGN - whose SED is dominated by non-thermal emission processes in the jets -, and ‘non’ blazars AGN - whose SED

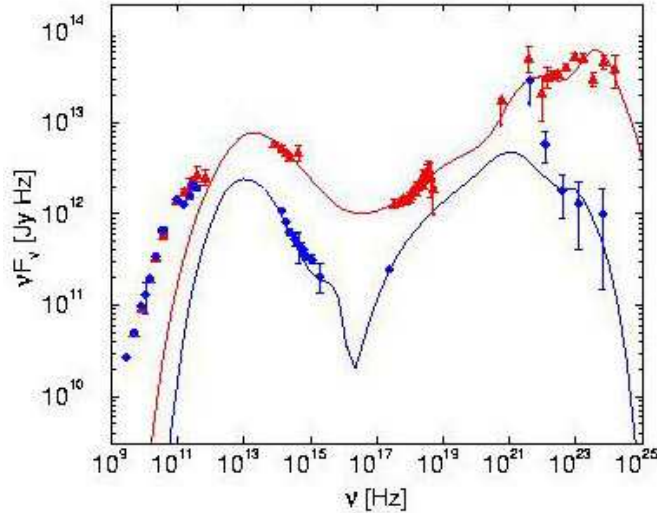


Figure 1.3: Spectral energy distribution (SED) of the Blazar 3C 279 in two different gamma-ray intensity states, from Hartmann et al. 2001.

is dominated by the thermal emission from the accretion disk. The AGN belonging to the first class are the most radio-loud AGNs and therefore they are considered jet-dominated objects; while the latter class includes radio-quiet quasars, Seyfert and radio galaxies and steep-spectrum radio quasars.

Concerning the similarities, the two main pieces of evidence are:

- All AGNs emit an almost constant power per decade of frequency in the range $\sim 100 \mu\text{m} - 100 \text{keV}$, whereas they show remarkably distinct behaviors at radio and gamma-ray energies: some of them are strong radio or gamma-ray emitters, whilst other are not;
- it appears that the spectral features across the largest portion of the SED do not depend on the AGN luminosities. In fact, they remain largely unchanged for AGN whose luminosity spans a wide range, even over about seven orders of magnitude.

As far as it concerns the differences in the SEDs, we start discussing the SED of Blazars.

The SED of the Blazar-type objects is usually modelled with two large humps (see Figure 1.3): the former peaks in the infra-red to soft X-ray energy band, the latter dominates the hard X-ray to gamma-ray regimes.

A further feature in the Blazar SED is a smooth transition from the radio emission to the infra-red one and this evidence is considered a possible suggestion that both emissions could have a common non-thermal origin.

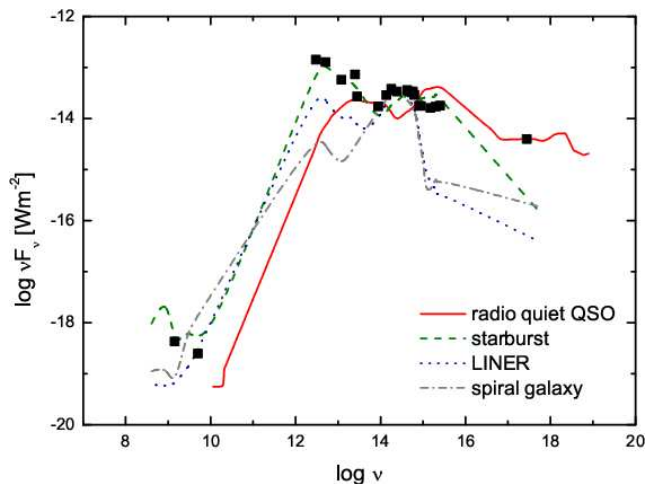


Figure 1.4: Spectral energy distribution (SED) of a radio-quiet object (in red, Elvis et al. 1994) and of the Seyfert Galaxy Mrk 609 (black points) constructed from literature values (Polletta et al. 1996; Rudy et al. 1988). The values are compared with average SEDs from normal galaxies, starbusts and LINERs.

A schematic plot of the SED for non-blazar objects is shown in Figure 1.4. The continuum can be quite well modelled via the convolution of a flat power law from the infrared band up to the X-rays one with some specific spectral features as for instance, the Fe $K\alpha$ emission line. Contrary to Blazar objects, in the SED of non-blazars the flux drops between the radio and IR band and this feature is at the basis of the distinction among radio-loud and radio-quiet AGN as discussed in section 1.4. It is worth noticing that although the radio emission from radio-quiet AGN is quite small in comparison to the total flux, it is still present and larger than that coming from normal galaxies. When looking to the SED of non-Blazar objects, it appears the presence of a peak that is known as the *infra-red bump*. A second prominent peak is located between the near-infrared and the UV. This feature is called the *Big Blue Bump*.

In the following we treat the most plausible emission mechanisms proposed for each waveband with the exception of the lower wavelength since a more detailed discussion about the SED properties in the X-ray spectral range will be presented in the following section.

Radio/IR: Radio/IR emission in powerful blazars (the FSRQ objects) is firmly believed to be Synchrotron emission from a population of relativistic electrons residing in jets. For the aim of completeness, we remind that the emitted power via Synchrotron emission by a relativistic electron is:

$$P_{syn} \propto \sigma_T \beta^2 \gamma^2 B^2 \quad (1.4)$$

where $\beta = v/c$, $\gamma = 1/(1 - (v/c)^2)^{1/2}$, and B is the magnetic field

intensity.

The radio spectral index is usually flat ($\Gamma_{radio} \leq 0.5$) in the core of a radio source and steep ($\Gamma_{radio} \geq 0.5$) in the outer lobes. The power law form of the spectrum results naturally if the energy distribution of the emitting particles is also a power law, that is, if the number of particles per energy interval is given by:

$$N(E) \sim E^{-p} \quad (1.5)$$

The particle distribution index p is related to the spectral index Γ_{radio} through $\Gamma_{radio} = (p - 1)/2$ (Rybicki & Lightman 1979).

The evidence for a steeper slope of the lobes is believed to be the result of the aging of the plasma. In fact, due to the fact that the plasma forming the lobes is older than that present in the neighborhood of the core, and that higher energies electrons cool faster - since the emitted Synchrotron power depends on the electron energy -, the number of high energy electron is lower in this region. Then it occurs that $p_{core} < p_{lobes}$. Due to the relation between p and Γ_{radio} , this condition fully explains the steepening of the spectrum. In blazars, observed at small angles, the Synchrotron radio emission from the jet is highly beamed. Radio-quiet AGN rarely show a jet+lobes radio structure similar to classical radio sources and at a considerable lower luminosity level. Frequently, the radio emission has a complex diffuse morphology. In these cases the commonly adopted interpretation is that the radio emission originates from a mixture of thermal and non-thermal processes associated with starbursts.

In the case of radio-quiet AGNs, non-blazar radio-loud AGNs and low-power blazars (the BL Lac objects), since the extrapolation of the radio emission into the IR band lies far below the observed IR flux and since the IR emission shows no rapid variability, the IR bump is generally attributed to thermal emission by dust, heated by the optical/UV radiation from the central energy source.

The range of temperatures required is wide, from ~ 50 to ~ 1000 K. In this scenario the drop in flux around $1\mu m$ is easily explained by the maximum temperature of ~ 2000 K that dust can reach before sublimation takes place and both the dust opacity to UV/radiation and its radiative efficiency decline.

As already quoted before, in powerful blazars the non-thermal radio emission smoothly merges with the infra-red emission, which is therefore naturally interpreted as the high energy continuation of the Synchrotron emission. The IR emission in non-blazar radio-loud AGN is likely a combination of both the thermal and non-thermal components discussed above.

Optical/UV: The currently most favored interpretation for the Big Blue Bump in radio-quiet, non-blazar radio-loud AGN and powerful blazars is thermal radiation produced by the gas in the accretion disk. The small bump

at $\sim 3000\text{\AA}$ is the sum of the contributions from the Balmer continuum, the blending of higher order Balmer lines and the blending of the Fe II lines. The low-power blazars (the BL Lac objects) lack the Big Blue Bump and their optical/UV radiation is just the steepening side of the Synchrotron bump, whose peak can also lie close in the X-ray band.

1.6 The X-ray spectrum: features and physical interpretation

A very large fraction of the bolometric luminosity of an AGN (larger than 20%, see Figures 1.3 and 1.4) is emitted in the X-rays band and soft-Gamma one. In addition, the rapid temporal variability of the emission observed in this band (occurring also on a time-scale of the order of hours), suggests that the radiation comes from the more interior regions: from some gravitational radius toward some hundredths of parsecs far from a super-massive black hole ($10^6 - 10^9 M_\odot$) accreting matter through an accretion disk (Standard Model).

Therefore, the availability of observational data in a wide spectral range ($0.1 \div 200$ keV) is very important since it allows us to analyze simultaneously the spectral characteristics originating in the more interior regions (within a few parsec far from the core) and, in turn, to study the radiative mechanisms that produce the observed emission, as well as, the geometry and structure of the object.

The spectral components of a RQ AGN observed in the X-rays and soft-Gamma bands are:

- the primary radiation (or intrinsic continuum) that is produced by the thermal comptonization (inverse compton) of electrons belonging to a hot and optically thin medium (named corona, whose temperatures are of the order of $100 \div 600$ keV, and whose geometry is still not well understood) with optical-UV photons coming from a cold, optically thick medium, probably the accretion disk (e.g., Haardt & Maraschi 1993, Haardt, Maraschi & Ghisellini 1994).

This component is well reproduced by a power law and an exponential cut-off: $F_E \propto E^{-\Gamma} \exp -E/E_{cut}$, where F_E is the photon energy differential flux, Γ ($\sim 1.7 \div 1.9$) represents the photon spectral index, and E_{cut} ($\sim 100 \div 600$ keV) is the value of the cut-off energy and it is related to the electron temperature inside the corona ($E_{cut} \sim kT_e$).

The observation of such component (i.e., of the Γ index and of the E_{cut} energy) allows to derive fundamental information on the temperature of the electrons in the corona and on both electron temperature and optical depth of the accretion disk;

- the two components of the Compton reflection of the primary radiation: the ‘Compton Reflection’ continuum and the emission of the fluorescence line of iron at 6.4 keV.

A relevant characteristic of the Standard Model is, indeed, the coupling between the accretion disk and the corona of hot electrons. In fact, a fraction of the X photons, produced in the corona, is re-emitted toward the disk. When this happens, the more energetic X photons (~ 100 keV \div 1 MeV) are reflected by the low energy electrons in the disk via Compton effect. This process produces a reflected continuum (the *Reflection*), that appears in the spectrum as a hump, named ‘Compton hump’ with a maximum located at about 20 \div 30 keV.

On the other hand, the less energetic X photons, due to the dependence on energy of the cross section of the photoelectric absorption process ($\sigma_{ph} \propto E^{-3.5}$), are at first photo-absorbed by the disk, and then re-emitted as UV photons via thermal emission.

Furthermore the photoelectric absorption of the electrons in the K shell of the elements present in the cold matter, produces the K emission lines via fluorescence effect. The strongest emission line is that produced by iron - that is indeed the most abundant element - at 6.4 keV if matter is mainly neutral, at 6.68 keV for the Fe *XXV* and at 6.97 keV for Fe *XXVI*.

The reprocessing structures, as described above, depend on the optical depth of the medium that reprocesses the primary radiation and on its geometry. In particular, if this medium is an accretion disk around a black hole, we expect that the Fe line is broad and with a characteristic distorted profile as a consequence of General Relativity effects. Therefore, its observation can provide important clues not only on the size of the internal radius of the disk and its inclination, but also on the central black hole;

- the low energy component (below 0.5 keV), called *Soft Excess*. It is probably a thermal emission from the disk, and provide indications about the temperature of the electrons inside the medium responsible for its production;
- the photoelectric absorption produced by ionized matter, named *Warm Absorber*, whose spectral fingerprint (around 1 keV) is represented by the absorption lines of highly ionized ions, mainly oxygen. It is commonly assumed that the Warm Absorber is gas located at a distance of few parsec far from the central region.

The general discussion on these components and their interactions, is furtherly complicated when a jet is present as in the case of blazars. As

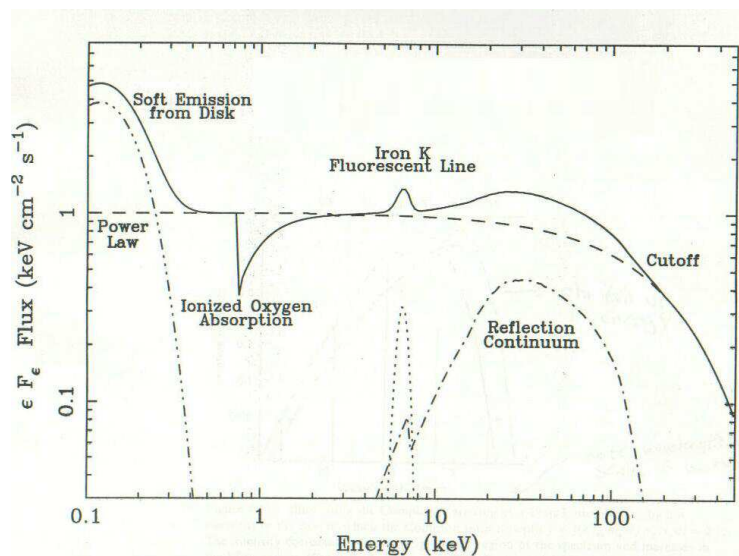


Figure 1.5: Broad-band X-ray spectrum of a Seyfert active galaxy.

already discussed, Blazars have very peculiar overall spectra compared to other AGNs.

The X-ray spectral difference of a RQ-type source and a RL-type source are clearly shown in the Figures 1.5 and 1.6, respectively.

The understanding of the physical scenario producing these peculiarities has not been fully achieved. For instance, and we will have way of seeing more in detail in the chapter 2 (section 2.3), it is commonly assumed that the high energy hump of the spectrum arises through the inverse Compton scattering of soft photons by highly relativistic electrons in the jet plasma. Sources of these soft photons could either be the local Synchrotron radiation within the jet or the nuclear optical/UV emission from the accretion disk eventually reprocessed by the emission lines region (BLR) and/or the dusty torus (Dermer & Schlickeiser 1993; Sikora, Begelman & Rees 1994), namely *Synchrotron Self-Compton* (SSC) and *External Compton* (EC) components, respectively.

However, in many objects, the interpretation of the physical scenario is not clear, because the observed spectrum can not be accounted for as due only to the combination of SSC and EC. This occurrence strongly suggests that the understanding of the empirical scenario is quite more complicated, as it will be discussed in the next Chapter.

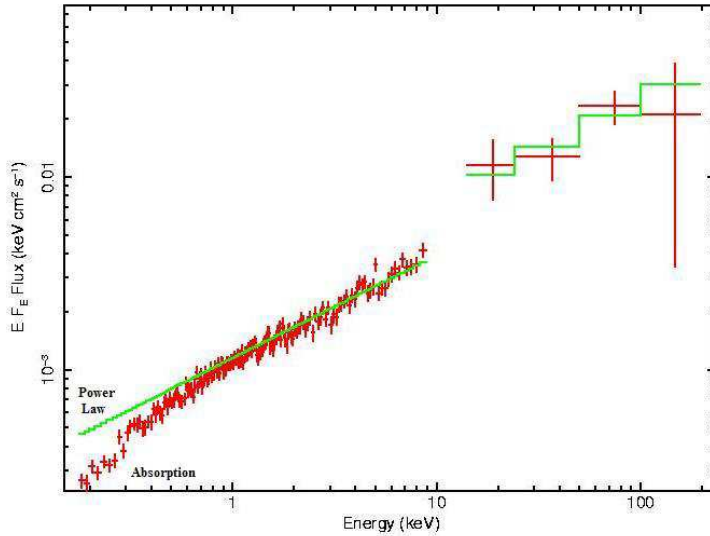


Figure 1.6: Broad-band X-ray spectrum of a radio-loud active galaxy.

1.7 Why is the study in the X-ray energy range important?

The study of AGNs in the X-ray energy range is of pivotal relevance for, at least, three reasons:

- the X-rays Luminosity (hereinafter L_X) represents a large fraction of the bolometric luminosity ($L_{Bol} \sim 10^{47} \text{ ergs}^{-1}$) of an AGN: $L_X \geq 20\% L_{Bol}$ (Elvis et al. 1994);
- it provides a relevant information that is complementary to those derived from the analysis of other spectral bands accessible with the other available instruments (such as the HST that works mainly in the optical bands, Spitzer with its infrared bands, etc.), and essential in order to identify the typical features of AGN spectra, and to evaluate the relative contribution of the various physical processes that determine the SED of an AGN;
- it is well known from the analysis of both the spectral and timing properties (e.g. Mushotzky, Done & Pounds. 1993, Yuan et al. 1998)(mainly of RQ objects) that the X-ray radiation is emitted from a region very near to the central engine. But the X-ray energy range, this region is not observable in any other spectral window with present generation of instrumental facilities;

- in the case of Blazar-objects a correlation between the X-ray variability and the optical one is expected as due to the jet/disk connection (see Sambruna et al. 2006).

The opportunity of investigating the central regions of the AGN is clearly very important. In this context, it is worthwhile to explain why the spectral variability and features in the X-ray band allow us this opportunity: the reason is that the typical timescale of the spectral variability is of the order of hours. This property allows to make quick important predictions about the physical region emitting the X-ray photons: it has to be very compact and centrally located. In fact, the requirement that the luminosity of the source could vary significantly, it is mandatory that the ‘information’ carried out by the photons, could transmit through the whole source. Since the information is transmitted with the light speed (c), a signal coming from a source with size equal to D will change on a timescale not less than $\Delta t \sim D/c$. Therefore, since $\Delta t \sim 1hr$, this implies that $D \leq 10^{-3}pc$ ($D \sim 10 - 100 R_{Sw}$).

The understanding of the physical reasons for the existence of this spectral variability has not been fully achieved. A possible scenario is that this variability is produced as a consequence of changes in both the density and ionization level of the dust and gas surrounding the central engine, that can absorb the X-ray emission.

As it has been stated above, the possibility to use the spectral variability in the X-ray band to constrain the properties of the central engine is limited to RQ AGNs. In fact, in the case of RL AGNs, the spectral variability is dominated by the variability of the jet and not by the one of the central source. The contribution to the whole spectrum of RQ objects, provided by the central region (accretion disk plus torus) is largely overwhelmed by the one produced by the jet.

Chapter 2

Blazars

2.1 Introduction

The Blazars are one of the most intriguing class of objects among the AGNs and are among the most enigmatic objects in astrophysics.

As we have seen in the section about the classification, this class include not only BL Lac objects, that are low-redshift RL sources but also FSRQ, that are high-redshift RL QSOs.

The possibility to study AGN at different redshifts, i.e. at different ages, is of crucial importance in order to assess the existence of systematic differences in the AGN properties as a function of the redshift. If this is the case, we could try to analyze how and why the AGN properties evolve with time and so to trace the evolutionary path of AGNs.

In addition, being very luminous objects, the investigation of Blazar-type AGN is a powerful and unique tool for understanding the cosmological evolution of the physical properties in their interiors and in their surroundings.

In this context, for instance, a key problem concerns the evolution of the galaxies: does each galaxy experience an evolutionary stage of intense activity or only a small fraction of the galaxies becomes active along the time as a consequence for instance of environmental effects?

Moreover, to investigate the properties of these sources, we can allow to understand if there is an evolution of the X-rays spectrum with the intrinsic luminosity of the object or with the redshift. If this would be the case, an important implication would be the fact that the properties of the central engine, powering the blazar, would evolve along the time. In addition, if the photon spectral index Γ and the amount of absorption intrinsic to the object, would also change, this empirical finding would mean that also the properties of the environment are changing with the time.

As we have seen in the Chapter 1, their large bolometric luminosity (10^{47} erg s⁻¹) is generally interpreted as due to the friction of dust and gas which

fall in a SMBH by forming an accretion disk. A mechanism that is able to transform about the half of the total mass of an object in energy, when the thermonuclear processes are able to transform a small fraction of the mass in energy. However, in the particular case of this class of AGN, a further effect has to be taken into account that is an effect of amplification of the emission from the continuum due to the additional presence of a relativistic jet aligned in the direction of the line-of-sight (see section 1.3).

The general scenario described above is also very useful for explaining why the QSOs were more numerous in the early Universe: the energy production ends when the SMBH has wasted all the gas, dust and stars present around it. This means that it is possible that the major fraction of all galaxies in the Universe, included the Milky Way, has experienced an evolutionary stage as a QSO and are now experiencing a quiescent stage due to the lack of fuel (matter) for the central Black Hole. This scenario has also the interesting implication that a QSO could ‘switch on’ if fresh matter is pushed inside the galactic center. This event could occur in many interacting galaxies, and indeed the fraction of QSO in these galaxies is larger than that of normal, non-interacting, galaxies.

2.2 The Blazar peculiarities

As discussed in the previous Chapter, the peculiar characteristics of a Blazar object is probably the one related to the presence of relativistic jets - strongly collimated and accelerated by a quite strong magnetic field - that pollute/dilute the AGN component and the reprocessing features and amplify the emission by means of a relativistic ‘beaming’.

It is the existence of these peculiar properties that makes the Blazar sources, fundamental objects for investigating more accurately the interaction between the jet and the environment. This is a pivotal step for studying the not-yet well understood physical mechanisms, responsible for the ‘extraction’ of non-thermal energy from the central black hole, and for the collimation and acceleration of the relativistic jets.

More in detail, as firstly suggested by Rees (1966), the plasma inside the jet of radio-loud AGN moves at relativistic velocity, and then it is able to efficiently transport energy from the SMBH neighborhoods to the distant lobes. However, this occurrence has strong implication for the observer looking at the jet at relatively small angles, as it is considered to be the case of BL Lac and FSRQ, that represent the class of Blazars.

In the case of a source emitting isotropically in its rest frame K' , in the observer frame K , where the source is moving with relativistic velocity ($\beta = v/c \sim 1$), three effects occur (adapted from Rybicki & Lightman 1979):

1) The light aberration: the angular distribution of the radiation is strongly peaked in front.

In particular, since for a particle in a magnetic field the speed and the acceleration vectors are orthogonal (in K'), the emitted photons observed in K form an angle given by $\sin\phi = 1/\gamma$, where $\gamma = 1/(1 - \beta^2)^{1/2}$ is the Lorentz factor of the accelerated particle. This means that in K , half of the photons are concentrated in a cone with semi-opening equal to about $1/\gamma$ and are not irradiated over the whole available solid angle equal to 2π .

2) Arrival time of the photons: the intervals of the photons emission and the photons arrival time, (Δt_e and Δt_a , respectively) are different. In the observer-frame K , we obtain $\Delta t_a = \Delta t_e / (1 - \beta \cos\phi)$ (there is the Doppler effect). Measuring $\Delta t'_e$ in K' , $\Delta t_e = \gamma \Delta t'_e$ and $\Delta t_a = \gamma(1 - \beta \cos\phi) \Delta t'_e = \Delta t'_e / \delta$, where δ is the Doppler factor.

3) Blue-shift frequency: since the frequency is the inverse of the time, we obtain $\nu = \delta \nu'$.

Due to the first effect, one observes that the jet intensity is strongly increased if its velocity vector is aligned near the line-of-sight. This effect is named with term "beaming" or "Doppler boosting". In particular, since I_ν/ν^3 is a relativistic invariant, one obtains for the observed specific intensity $I_\nu(\nu) = \delta^3 I'_{\nu'}(\nu')$ and the integration on the frequency from $I = \delta^4 I'$. In the same manner, by assuming that the spectrum of the synchrotron emission could be approximated by a power-law of the type $F'_{\nu'}$ proportional to $\nu'^{-\alpha}$, it is possible to find for the received flux: $F_\nu = \delta^{(p+\alpha)} F'_{\nu'}(\nu)$ with $p = 3$ and 2 , in the cases of a source with an isotropic motion and a continuum jet, respectively. More complicated cases are possible (Lind & Blandford 1985). The effect of the beaming is maximized for angles of view $\phi = 0^\circ$, in which case $\delta \sim 2\gamma$.

The second effect predicts the observation of an apparent super-luminal motion for objects oriented with very small angles as firstly indicated by the work of Rees (1966).

2.3 The Blazars spectral features and radiative processes

The Blazars are powerful emitters in every energy band of the electromagnetic spectrum with a very strong radio emission ($\geq 10^{41}$ erg s $^{-1}$) and with a bolometric luminosity between 10^{46} - 10^{48} erg s $^{-1}$.

A very large fraction of this luminosity ($\sim 20\%$) is emitted in the X-ray energy band, and we are just interested to investigate it.

As we have seen, the commonly adopted approach for illustrating the multiwavelength energy output of a Blazar is through the SED, that corresponds to a broad band spectrum covering the whole range of frequencies, from radio to gamma-rays, generally represented in a $\log \nu F_\nu - \log \nu$ plot. The SED of these sources can be well described by a double-hump profile: Synchrotron and Inverse Compton (IC) (see Figure 2.1). In these objects

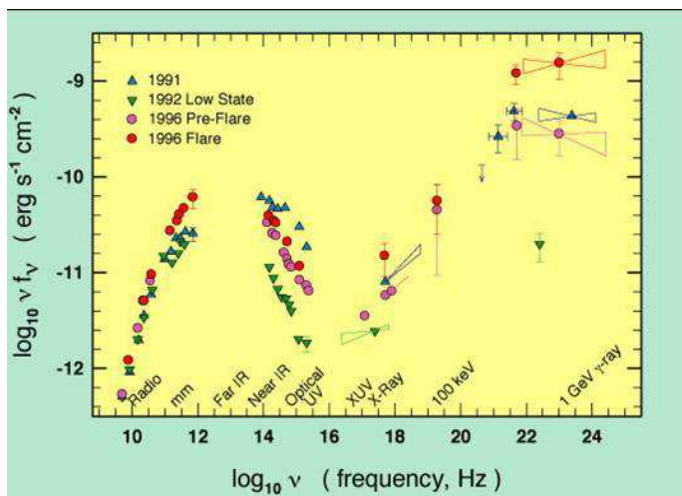


Figure 2.1: An example of the SED for blazar (the objects 3C 279, see <http://heasarc.nasa.gov/docs/cgro/epo/posters/>). The results shown in this plot summarize several multi-wavelength campaigns covering the frequency regions from the radio through the gamma-ray range observed by EGRET.

there is a mix of disk and jet emission, with the jet dominating the radio/IR and hard X-rays (via Synchrotron and IC) and the disk dominating the optical/UV through soft X-rays. The component dominating the SED of these objects is the non-thermal one, associated to the jet.

We will now briefly discuss the radiative process that is at the basis of the thermal emission component, whereas we will discuss more in detail the radiative processes that cause the non-thermal emission of these objects. In fact, these are the processes that produce the features in the energy spectral range we are working with.

The spectral feature with thermal origin that appears in the optical/UV and soft-X energy range can be well described with a black-body emission originating from the optically thick disk. It is the spectrum of a multi-temperature black-body: at any radius of the disk there is a slightly different temperature and the resulting spectral profile is given by the convolution of each black-body spectrum at a fixed temperature.

The non-thermal components are produced by blobs of relativistic plasma (probably composed mostly by electrons and positrons or electrons and protons) that are collimated and accelerated by a strong electromagnetic field and forming the so-called 'jet' of Blazars.

The simplest scenario to account for the non-thermal emissions and their relative spectral features from radio up to gamma-rays, assumes a spherical homogeneous source filled by a single relativistic electrons population N and by a tangled magnetic field B (see Maraschi & Tavecchio 2003 for a full description). This spherical region moves with bulk Lorentz factor Γ_{bulk} at

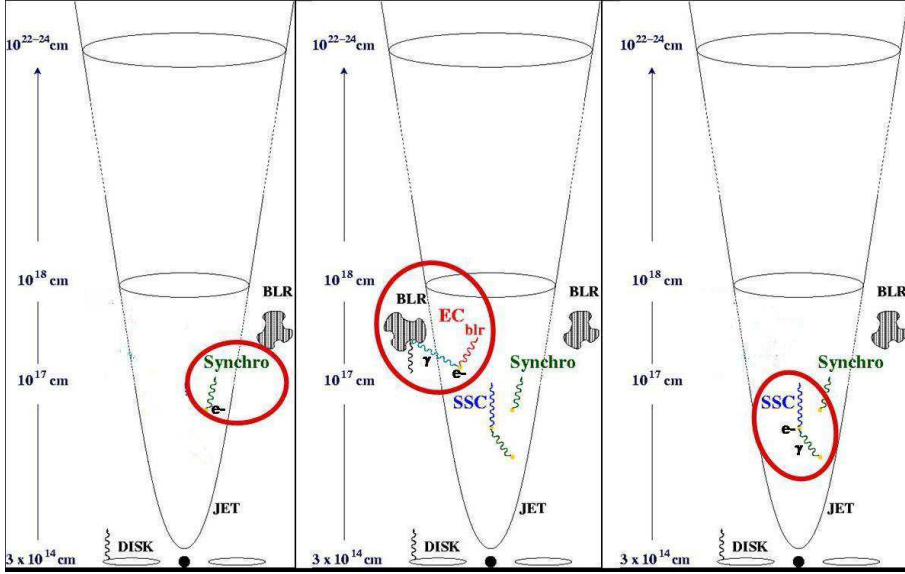


Figure 2.2: Representation of the physical interactions that give the non-thermal spectral features observed in the SED of the Blazar-type sources.

an angle of view $\theta \sim 1/\Gamma_{bulk}$ with respect to the line of sight (under these conditions the relativistic Doppler factor is $\delta = \Gamma_{bulk}$). In the Blazar environment a field of external soft radiation with energy density U_{ext} interacts with the blob of relativistic plasma.

Within the scenario described above, the first non-thermal component, the hump at low-energy, is produced by relativistic electrons which irradiate via Synchrotron processes (see section SED) in a magnetic field in a range between 10^{-4} and 10^4 Gauss (see sketch on the left in Figure 2.2).

If one assumes the distribution given by a power law for the relativistic particles then the resulting total spectrum is still a spectrum F_ν that can be described by a power law with spectral index in the radio correlated with the p index of the particle distribution through the formula $\Gamma_{radio} = (p - 1)/2$ (Rybicki & Lightman 1979). The frequency at the peak of this component is given by:

$$\nu_{Syn} \propto \gamma^2 \nu_L \delta \quad (2.1)$$

where γ is the Lorentz factor of the charged particles, ν_L is the characteristic frequency of Larmor ($2.8 \cdot 10^6 B$ Hz) and δ is the Doppler factor. The relevant data that can be obtained by studying this component present in the radio are: the distribution function of the radiating particles and the magnetic field in which they are embedded.

The second non-thermal component is in general the sum of the SSC and External Compton (EC) emission.

The SSC component (see sketch on the right in Figure 2.2) is believed to be produced through IC scattering of soft photons by the same electrons which have produced them (SSC model, e.g. Maraschi, Ghisellini & Celotti 1992), although other scenarios have been considered (e.g. hadronic models, see Mannheim & Biermann 1992).

Also in this case as in the previous one if the distribution of the high-energy electrons is described by a power law, the resulting spectrum will be still described by a power law with a peak frequency that will depend by the Γ of the relativistic particles and by the Synchrotron frequency according to the formula

$$\nu_{SSC} \propto \gamma^2 \nu_{Syn}. \quad (2.2)$$

From this formula, we can note that, with an average γ of 10^4 , the boost energy of the photons emitted via Synchrotron causes the transformation of the radio/IR photons into X-ray photons. Also in this case, as in the previous one, the study of this component provides information about the distribution function of the relativistic electrons and the strength of the magnetic field.

About the EC component, it seems to be produced by the scattering between high-energy electrons and soft photons external to the jet. The latter ones may be produced by the accretion disk itself and be scattered/reprocessed in the BLR (EC model, Dermer & Schlickeiser 1993; Sikora, Begelman & Rees 1994).

This process is schematically represented in Figure 2.2 (sketch at the center). Again, as in the two previous cases, if the electron population has a power law distribution, the resulting spectrum is described by a power law. The peak frequency of this component now depends not only on the γ of the relativistic electrons and the frequency of the photons field, but also on the Γ of the blob according to the following relation:

$$\nu_{EC} \propto \gamma^2 \Gamma_{blob} \nu_{BLR} \delta. \quad (2.3)$$

The additional information that is obtained from the study of this second high energy component is the energy density U of the external photons field. In the case in which the ambient photons are dominated by the emission from the BLR clouds it is customary to model the external photon spectrum with a black body shape peaking around $\nu_{BB} \sim 10^{15}$ Hz (e.g., Ghisellini et al. 1998). In this case, the energy density U_{ext} is the energy density of the BLR radiation, given by $U_{BLR}^{obs} = L_{BLR}/(4\pi c R_{BLR}^2)$. Here R_{BLR} is the BLR extension that is measured either through reverberation mapping where a $R_{BLR}-\lambda L_{\lambda}(5100\text{\AA})$ relation is assumed (Kaspi et al. 2005) or through the relation $R_{BLR} \sim 10^{17} (L_{disk}/10^{45})^{1/2}$ cm (Maraschi et al. 2008).

From the basic equations for the processes above described (see Rybicki & Lightman 1979), it is possible to retrieve the dependence of the fluxes on

the three non-thermal components from principal parameters such as:

$$\begin{aligned} F_{Syn} &\sim \delta^4 N B^2 \\ F_{SSC} &\sim \delta^4 N^2 B^2 \\ F_{EC} &\sim \delta^4 N U_{ext} \end{aligned}$$

and one can note that, with increasing electron density or strength of the magnetic field, the SSC flux increases, while the increase of the disk luminosity or of the global Lorentz factor Γ bulk (and in turn, of δ), cause an increase mainly of the EC flux.

It is widely accepted that the SEDs of Blazars sources follow a sequence (see Figure 2.3) with the luminosity (Fossati et al. 1998, Donato et al. 2001): the powerful sources, that is the FSRQs, are characterized by SEDs whose Synchrotron and IC peaks are in the radio/IR and X-ray or even MeV band, respectively, while the low-power blazars, that is the BL Lacs, show the maxima of their components in the optical/UV or even soft X-ray band and in the hard X-ray or GeV-TeV region. Ghisellini et al. (1998) proposed that the sequence could be related to the balance between acceleration and cooling acting on the electrons emitting most of the power: electrons in the jet of FSRQs are characterized by strong radiative losses, and thus cannot reach large energies. On the contrary in BL Lacs the small cooling allows the electrons to be accelerated to very high energy and determines high frequencies for the Synchrotron and IC emission components (see Ghisellini & Tavecchio 2008, 2009 for a refined view).

However, despite of this general view, the nature of soft photons involved in the IC processes is still debated. It is widely believed that the IC emission from powerful blazars (FSRQ) is dominated by the EC component with photons coming into the jet from the external environment as the dominant population. For BL Lac objects the energy density of target photons is probably dominated by those produced by Synchrotron. We stress here that in the simplest case of a single EC component, the X-ray spectrum of FSRQs represents the low-energy side of the IC peak and therefore is due to low-energy electrons scattering the externally produced photons. This spectral band could give then information on a part of the electron spectrum that, because of self-absorption, is not accessible in the low-frequency Synchrotron component. This same energy band in the case of BL Lac objects gives indeed information about the position of the Synchrotron peak.

2.4 Open questions

As we have seen in Chapter 1 (sections 1.2 and 1.6), the spectrum of an AGN in the X-rays band is usually well described by a power-law with a specific flux (i.e. per unit energy interval) of the form $N(E) \propto E^{-\Gamma}$, where E is the energy, $N(E)$ is the number of photons in units of $s^{-1} \text{ cm}^{-2} \text{ keV}^{-1}$ and Γ is the photon index.

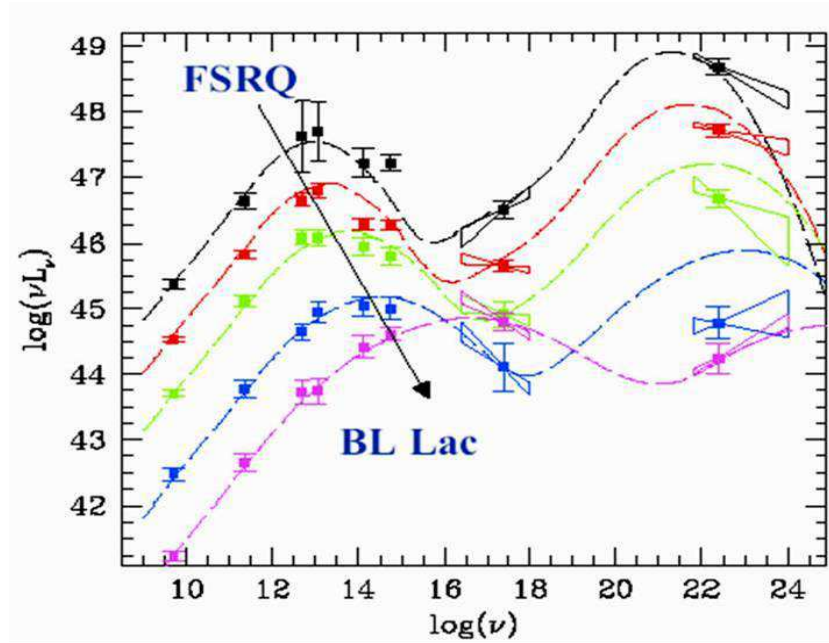


Figure 2.3: A phenomenological sequence discovered by Fossati and collaborators (1998) that shows that the values of the peak frequency are fixed by the radio luminosity: higher radio luminosity objects peak at lower frequencies.

However, despite of this general view, in the X-ray spectra of the Blazars there are some deviations from the simple power-law. These spectral signatures appear in the soft X-ray band with a curvature - a flattening or a steepening of the spectrum - and towards high energies with a "hardening" of the spectrum.

To date, these features have not still a clear physical interpretation and pose the following questions:

- How to explain the flattening of the primary intrinsic continuum with respect to a simple power-law observed at low energies in many RL objects? (Page et al. 2005, Galbiati et al. 2005, Yuan et al. 2006)
- Which is the origin of the steepening of the primary intrinsic continuum with respect to a simple power-law - usually named soft excess emission component - observed in some RL sources? (Sambruna et al. 2006, Kataoka et al. 2008)
- Is the "hardening" of the observed spectrum of some RL objects interpretable as a component of Compton reflection of the power-law continuum from a cold reprocessor? (George & Fabian 1991)

So far, there exist two physical interpretations of the flattening feature above mentioned: absorption in excess to the Galactic one (e.g. Cappi et al.

1997) and a break in the intrinsic continuum (e.g. Sikora, Begelman & Rees 1994, Tavecchio et al. 2007). In the case of the absorption, a dependence between the hydrogen column density of the absorber and the redshift has been also proposed. In fact, in a former work of Yuan et al. (2006) based on XMM observations of a sample of 32 RL sources a N_H -redshift correlation has been found.

Also in the case of steepening, there exist alternative physical interpretations as: the presence of a continuum break or a bulk Compton emission (Celotti, Ghisellini & Fabian 2007). This latter is between the most recent interpretations suggested for the soft X-ray band emission and it is associated to the existence a ‘cold’ electrons population in the jet. The detection of a component of a bulk comptonization is quite important since this is the unique opportunity we have for tracing this population of electrons. In fact, these particles would make Synchrotron in the regime of absorption and, so not observable.

Concerning the hardening of the spectrum, contrary to RQ sources the presence of the reflection features - most notably the Fe K-alpha line and the associated Compton reflection “hump” peaked at about 20 – 30 keV - from the cores of the RL AGN is not well established. In particular, in RQ AGNs the reprocessed features are generally intense and always detected (Matt 2001), whereas in RL AGNs the iron line and the reflection component can be absent or weak. The simplest interpretation is that the reflection features are diluted by the beamed emission of the jet (Sambruna et al. 2006). X-ray observations of RL AGN by ASCA, RXTE and Beppo SAX (e.g., Sambruna, Eracleous & Mushotzky 1999; Eracleous, Sambruna & Mushotzky 2000; Grandi et al. 2001; Ballantyne, Ross & Fabian 2002; Grandi & Palumbo 2004) have shown that some of these objects (defined as Broad Line Radio Galaxies and therefore their jets are not oriented along the line-of-view) seem to have weak hard X-ray reflection features. These results have important implications for understanding the physical distinction between RQ and RL objects, that is why strong radio sources (lobes, jets, etc.) arise somehow only in a small fraction of AGNs. In particular the detection of an iron line could provide an important tool for mapping the inner region of AGN and for determining the BH central mass (Fabian et al. 1989; George & Fabian 1991).

2.5 Aim of this work: a broad-band study of Blazars

Most of our knowledge on the AGNs is based on the analysis of RQ AGN since they contribute to about 90% of the whole AGN population. Nevertheless, in general for a given optical luminosity, the X-ray band emission provided by a RL AGN, is about a factor of 3 larger than that of a RQ AGN (Zamorani et al. 1981; Worrall et al. 1987) and this occurrence allows us to

study RL AGN at the larger redshifts.

It is clear that to investigate the Blazar sources, as RL AGN, is quite important in order to shed light on the properties of this ‘minor’, but significant, sub-class of objects.

In particular, most of the investigations on the Blazar objects performed so far have been limited to small spectral windows of the X-ray energy range. This represents a big limitation. In fact, to the aim of understanding more carefully the physical properties of these objects and the physical processes responsible for their - non thermal - emission, it is fundamental to perform measurements of the shape of the primary continuum, of the energy cut-off, of the two components of the Compton reflection, and of the emission-absorption/flattening in the low-energy tail of the X-ray band.

It is worth noting here that although the two features of absorption and emission appear in soft-X ray band, the availability of broad-band observations (0.2 – 100 keV) is relevant to well reproduce the global shape of the spectrum. Infact, if the continuum is not well reproduced, the interpretation of these features is ambiguous; in this case the availability of a broad band analysis is mandatory in order to disentangle the contribution of the various physical processes. Therefore hard X-ray observations play a key role not only for the study of reflection features (the Fe K-alpha emission line between 6 and 7 keV and the Compton reflection hump at energies above 10 keV) but also for the flattening or/and steepening in the spectrum shape at low energies.

From the requirement mentioned above, it derives the importance of a broad-band spectral analysis, i.e. in the energy range 0.2 – 100 keV. This broad-band analysis can be performed only by combining together measurements obtained by instruments working in the high energy range (above 20 keV) such as INTEGRAL, with those provided by satellites operating in the low-energy interval (0.2 – 10 keV) such as XMM-Newton and Swift/XRT.

Our aim is therefore to investigate the open questions mentioned in previous section about the emission processes of these objects, the nature of their environment and its interaction with the jet.

To this purpose, we will present a broadband (0.2-100keV) X-ray study of a sample of blazars observed with INTEGRAL, Swift and XMM-Newton satellites. The wide energy range covered by the instruments at low energies and the INTEGRAL satellite is well suited to the study of the three open questions discussed above. In particular, INTEGRAL could give a fundamental contribution to the topics mentioned above by means of significantly increase of its data set coming soon publicly available (Bird et al. 2009).

Chapter 3

INTEGRAL: INTERnational Gamma Ray Astrophysical Laboratory

3.1 Introduction

The data used in this thesis are mainly based on observations with the IBIS instruments on board INTEGRAL.

The ESA gamma-ray observatory INTEGRAL, launched on 17 October 2002, continues to produce a wealth of discoveries and new results on compact high energy Galactic objects, nuclear gamma-ray line emission, diffuse line and continuum emission, cosmic background radiation, AGNs, high energy transients and sky surveys. The mission's technical status is healthy and INTEGRAL is continuing its scientific operations well beyond its 5-year technical design lifetime. In fact, the INTEGRAL mission, together with the ESA *XMM-Newton* one, has been recently extended to be operative up to December 2012, because of the excellent scientific results.

3.2 The INTEGRAL mission: an overview

The ESA observatory INTEGRAL (Winkler et al. 2003) is dedicated to the fine spectroscopy and fine imaging of celestial gamma-ray sources in the energy range 15 keV to 10 MeV with concurrent source monitoring in the X-ray (3-35 keV) and optical (V-band, 550 nm) bands. INTEGRAL, with a total launch mass of about 4 tons was launched by a four-stage PROTON from Baikonur/Kazakhstan on 17 October 2002. The orbit is characterized by a high perigee in order to provide long periods of uninterrupted observations with nearly constant background and away from trapped radiation (electron and proton radiation belts). The orbital parameters at the beginning of the mission were: 72-hour orbit with an inclination of 52.2 degrees,

a height of perigee of 9,050 km and a height of apogee of 153,657 km.

Owing to background radiation effects in the high-energy detectors, scientific observations are carried out while the satellite is above a nominal altitude of typically 40,000 to 60,000 km. This means that most of the time spent in the orbit provided by the PROTON can be used for scientific observations, about 210 ksec per revolution orbit.

INTEGRAL carries two main gamma-ray instruments, the spectrometer SPI (Vedrenne et al. 2003), optimized for the high-resolution (2.5 keV FWHM at 1 MeV) gamma-ray line spectroscopy (20 keV - 8 MeV), and the imager IBIS (Ubertini et al. 2003), optimized for high-angular resolution (12 arcmin FWHM) imaging (15 keV - 10 MeV). Two monitors, JEM-X (Lund et al. 2003) in the (3-35) keV X-ray band, and OMC (Mas-Hesse et al. 2003) in the optical Johnson V-band complement the payload. All instruments are coaligned with overlapping fully coded field-of-views ranging from 4.8° diameter (JEM-X), $5^\circ \times 5^\circ$ (OMC), to $9^\circ \times 9^\circ$ (IBIS) and 16° corner-to-corner (SPI), and they are operated simultaneously, providing the observer with data from all 4 instruments.

3.3 The INTEGRAL Observatory

Most of the observing time, from 65% of the total time in the first year to 75% for subsequent years, is devoted to the scientific community. Typical observations last from 100 ks up to about one or few Ms, depending on the target or sky region. Proposals for observations are selected on their scientific merit only by a Time Allocation Committee. These selected observations form the basis of the "General Programme".

The remaining fraction of the total observing time was the "Core Programme", reserved for scientific institutes which have developed and delivered instruments (the INTEGRAL Science Working Team, ISWT) and for the scientific Data Centre (guaranteed PI time). During the nominal period of the mission, the Core Programme consisted of three parts with a dedicated exposure time per year:

- Frequent scans of the galactic plane (Galactic Plane Survey, GPS): these scans provide a periodic monitor of the gamma-ray sky to search for transient sources and monitoring the persistent ones. The scans are performed weekly with a "slew and stare" manoeuvre of the spacecraft along the seasonally visible part of the galactic plane within a galactic latitude of $\pm 10^\circ$.
- Deep Exposure of the galactic central radian (Galactic Central Deep Exposure, GCDE): has the aim of mapping line emission and diffuse emission of the central galactic region and to perform deep imaging

and spectroscopic studies of the galactic bulge and of the single point sources around the galactic centre zone.

- Target of opportunity (ToO), pointed observations of selected sources.

One of the key outcome of the INTEGRAL Core Program is mapping the soft gamma-ray sky with particular interest in the galactic plane regions of the galaxy from 20 keV up to 1 MeV.

Within the new "Key Program" (KP) strategy, started after the mission extension to cover the period 2008-2012, only specific interesting zones of the sky plane, not covered enough, are the target of observations (with a significant amount of annual observing time – one to few Ms –).

The first operational years were dominated by observations of the Galactic bulge and plane regions, largely also thanks to the high priority Core Programme observations. During the recent years, the sky exposure has started to open up for higher galactic latitudes. This, for example, has led to a significant increase in the number of detected extragalactic sources as listed in the 4th IBIS/ISGRI survey (Bird et al. 2009) compared to earlier IBIS survey catalogues. As of October 2009, INTEGRAL has spent about 168 Ms on science observations including dozens of Target of Opportunity observations (totaling about 2 Ms per year), which provide highly important serendipitous science.

3.3.1 Observing modes

In order to minimize systematic effects taking place in the the two main instruments, SPI and IBIS (see Section 3.4) due to spatial and temporal background variations, a controlled and systematic spacecraft dithering manoeuvre was required.

This manoeuvre consists of several off-axis pointings of the spacecraft pointing axis from the target in steps of 2 degrees. The integration time for each pointing could vary in the range 0.5–1 hour and time is adjusted in a way so that always multiples of a complete dither pattern are executed for each observation. Two main, different pointing patterns are currently used:

- Hexagonal dither pattern: this consists of a hexagonal pattern around the nominal target location (1 source on-axis pointing, 6 off-source pointings, each 2 degrees apart).
- Rectangular, or 5×5 , dither pattern: this consists of a square pattern around the nominal target location (1 source on-axis pointing, 24 off-source pointings, each 2 degrees apart). This is the nominal pattern for the best use of both SPI and IBIS.

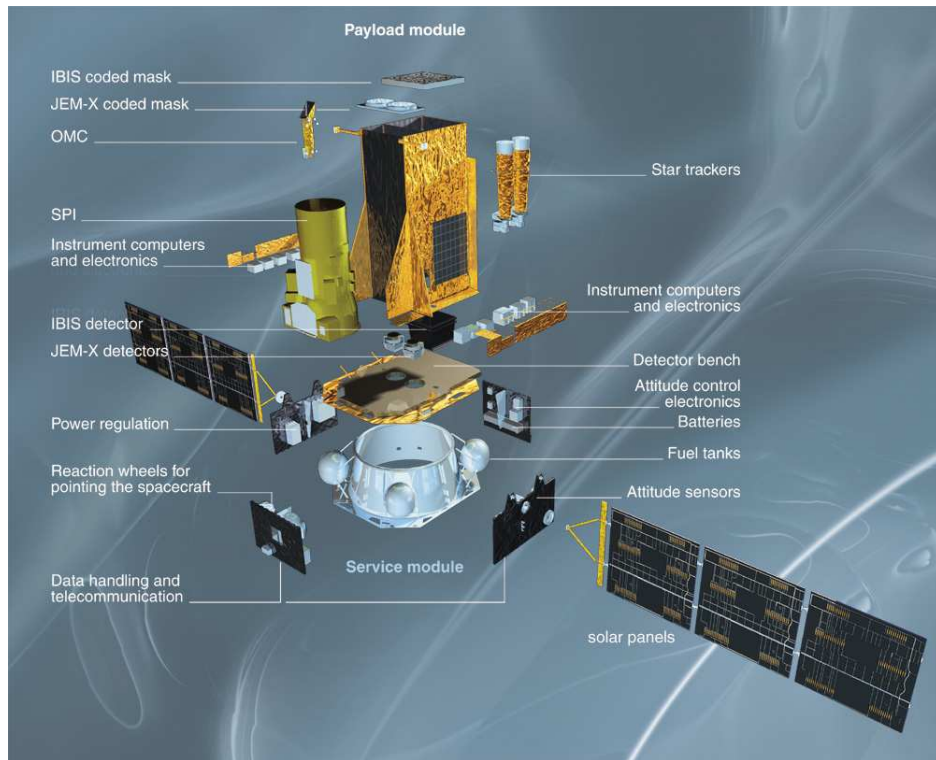


Figure 3.1: An INTEGRAL payload modules view.

3.4 The instruments on-board INTEGRAL

The two main gamma-ray instruments, integrated in the INTEGRAL payload (Fig. 3.1), have both spectral and angular resolution, but they are differently optimized in order to complement each other and to achieve overall excellent performance. The Spectrometer, the Imager as well as the X-ray monitor have a common principle of operation: they are all coded aperture mask telescopes.

3.4.1 Coded mask telescopes

An X- and γ -ray telescope works outside the earth atmosphere and is designed to collect as much information as possible on the incident radiation emitted from a source. It should have the capability to provide information on the position of the sources, on its flux variation, timing properties and on its energy distribution.

The techniques used for the source imaging depends on the energy range considered.

The X-rays can be reflected from surfaces, but at very small incidence angles. The critical grazing angle (the maximum incidence angle at which

reflection can occur), is inversely proportional to the photon energy, so that reflecting high-energy X-rays requires very small incidence angles. This makes designing practical mirrors very difficult. Up to soft X-rays (< 20 keV) methods, using multiple reflections, are available to increase the typical reflection angles and permit to focus the X-rays on the detector, as for example, a combination of a paraboloid mirror and an hyperboloid mirror. This solution was used in satellites like *HEAO-2* and now *Chandra*.

It is not easy to focus a γ -ray photon because it passes through most of materials and thus cannot be simply reflected by a mirror like optical photons. For gamma-ray observations one of the commonly techniques use the coded aperture masks system.

This imaging techniques employs straight-line ray optics that offer the opportunity to image at higher photon energies and over larger FOVs. The characteristic of this techniques is that the direction of the incoming rays is, before detection, encoded, so the image of the sky has to be reconstructed by decoding the observation afterward.

This method of producing sky images is a two-step, indirect procedure in contrast to the direct, one-step, imaging procedure of focusing techniques. These alternative techniques are referred to as multiplexing techniques, for which, for equal collecting areas, the sensitivity of a focusing instrument is always better. Multiplexing techniques can be divided into two classes: those based on temporal and those on spatial multiplexing.

In a spatial sensitive coded-mask telescope such as IBIS, the imager on board INTEGRAL satellite, the imaging system and concept is shown in Fig. 3.2. A coded mask is made of opaque plates and holes optimally distributed and it is placed above the detector. The detector plane records the shadow of the mask projected by the gamma-ray sources located within the field of view.

For any particular telescope geometry, the field of view consists of two different zones: The Fully Coded Field of view (FCFOV) in which the detected flux is completely modulated by the mask, and the Partially Coded Field of View (PCFOV) in which the detected photons are coded only by a fraction of the mask.

The angular resolution, $d\theta$, of a coded mask telescope depends on the ratio between the mask element size, C , and the mask-detector distance, H . Each peak in the deconvolved image has angular extent (FWHM) of approximately the size of C/H . For point sources and no source confusion, the parameter actually driving the imaging performance is the Point Source Location Accuracy (PSLA). The theoretical PSLA is limited by the spatial resolution of the detector array.

$$PSLA = \arctan(d/H)/n \quad (3.1)$$

with d the detector inter-pixel separation and n the Signal to Noise ratio

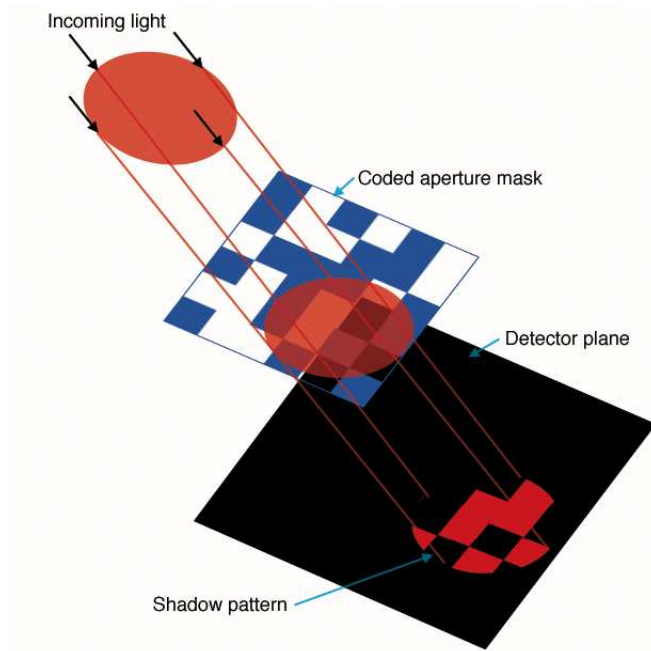


Figure 3.2: Schematic diagram illustrating the working principle of a coded aperture camera: the recorded count rate in each pixel of the detection plane is the summation of contributions from each source flux modulated by the mask.

(S/N).

3.4.2 The gamma-ray imager IBIS

IBIS, Imager on Board the INTEGRAL Satellite (Ubertini et al. 2003), provides diagnostic capabilities of fine imaging (12 arcmin Full Width Half Maximum). The source location accuracy is of 30 arcsec for strong sources, the FOV is $19^\circ \times 19^\circ$ (Full Width to Half Response) with a FCFOV of $9^\circ \times 9^\circ$. The detection unit is composed of two gamma-ray cameras separated by 10 cm:

- ISGRI (INTEGRAL Soft Gamma-Ray Imager), covering the range from 15 keV to 1 MeV, has a detection plane made of 16384 physically independent cadmium telluride semiconductor crystals organized in eight modules (Lebrun et al. 2003).
- PICsIT (Pixilated CsI Telescope) covering the range from 170 keV to 10 MeV, made of 4096 cesium iodide crystal scintillators.

Photons are detected by IBIS in three modes: detection on ISGRI, detection on PICsIT, and detection on the two layers (Compton mode). Table

3.1 shows the principal IBIS scientific capabilities.

Two anti-coincidence shields protect the detector from external radiation:

- a passive shield composed by an “hopper ” unit (truncated pyramid on the top of the ISGRI detector) and a “tube ” made of four walls closing the aperture down to the hopper level. The passive shielding is designed to reduce the celestial diffuse background component; it becomes transparent above 200 keV;
- an active anti-coincidence shield, the VETO anti-coincidence system that is composed of 16 independent modules, each made with two large BGO crystals. This ensures a substantial reduction of the background due to the induced photons and hadronic component, enhancing the detector sensitivity. Measured over the whole energy range, the VETO system provides a background suppression effect of $\sim 50\%$ for ISGRI and $\sim 40\%$ for PICsIT.

Table 3.1: An overview of the IBIS scientific capabilities.

Energy Range	15 keV–10 MeV
Continuum sensitivity, at 3σ and 10^6 s integration ($\text{ph cm}^{-2} \text{s}^{-1} \text{keV}^{-1}$)	2.3×10^{-6} @ 100 keV 1.6×10^{-6} @ 1 MeV
Line sensitivity, at 3σ and 10^6 s integration ($\text{ph cm}^{-2} \text{s}^{-1}$)	1.8×10^{-5} @ 100 keV 3.8×10^{-4} @ 1 MeV
Energy Resolution (FWHM %)	8% at 100 keV ISGRI 10% at 1 MeV PCSIT
Angular resolution (FWHM)	$\sim 12'$
Point Source Location Accuracy (90 % error radius)	30" @ 100 keV (50σ source) 3' @ 100 keV (5σ source) 5'-10' @ 1 MeV (5σ source)
Timing accuracy	61 μs - 1 hr
Field of View	$9^\circ \times 9^\circ$ (fully coded) $29^\circ \times 29^\circ$ (zero response)

The basic design of the IBIS mask (Figure 3.3) is a Modified Uniformly Redundant Array (MURA)¹ of 53×53 elements. This pattern, reiterated four times and cut on the borders, provides the IBIS mask of 95×95 individual square cells. Half of them are in tungsten (16 mm thickness) offering a 70% opacity at 1.5 MeV; the other half are opened and covered by a carbon fibre with an off-axis transparency of 60% at 20 keV.

¹For design and properties of MURA pattern, see Gottesman & Fenimore (1989)

The FCFOV size, for which sensitivity is the nominal one, is $9^\circ \times 9^\circ$; it becomes then 50% at 19° , and response decreases to zero at 29° . The angular resolution is $d\theta = \arctan(C/H) = 12'$ with $C = 11.2$ and $H = 3133$ mm.



Figure 3.3: IBIS coded mask patterns

Since the work of this thesis is based on data from ISGRI/IBIS, here we give some details on this just layer detector.

Each pixel of the ISGRI camera is a spectrometer chain with its own characteristics. The spectral performance of the camera depends therefore critically on the alignment of the pixel gains and offset. The alignment is performed in two steps: the electronics allow for a rough alignment and then a fine software correction must be applied.

In principle, the amplitude of the pulse yields the energy of the incident photon. However, above 60 keV the energy is a function of both pulse height and rise time, because of the charge trapping inside the CdTe material. The longer the rise time, the more important are the charge losses. In order to determine the energy for each photon, raw data are corrected on-ground using Look Up Tables (LUTs) carried out by calibrations. In addition, the resulting line profile is no longer a Gaussian, but more similar to a Lorentzian. ISGRI energy resolution (Tab. 3.1) depends on the operating temperature, and also on the bias voltage.

3.4.3 The spectrometer SPI

The spectrometer SPI (SPectrometer on INTEGRAL) provides spectral analysis of gamma-ray point sources as well as extended sources over an energy range between 20 keV and 8 MeV.

Table 3.2: An overview of the SPI scientific capabilities.

Energy Range	20 keV – 8 MeV
Continuum sensitivity, at 3σ and 10^6 s integration (ph cm ⁻² s ⁻¹ MeV ⁻¹)	1.5×10^{-4} @ 1MeV
Line sensitivity, at 3σ and 10^6 s integration (ph cm ⁻² s ⁻¹)	5.1×10^{-6} @ 1MeV 2.8×10^{-5} @ 511 keV
Energy Resolution (FWHM %)	2.33 keV @ 1.33 MeV
Angular resolution (FWHM)	$\sim 2.0^\circ$
Timing accuracy (3σ)	0.129 ms
Field of View	16° (corner to corner) (fully coded)

The field of view is 16 degrees with an angular resolution of 2 degrees. The SPI detector is composed of an array of 19 hexagonal high purity germanium detectors. Table 3.2 summarizes the principal SPI scientific capabilities. Emission lines from radioactive nuclei, such as ²⁶Al, are the main observational subjects of the spectrometer SPI.

The SPI Mask, placed 1.7 m above the 19 germanium detectors, is a Hexagonal Uniformly Redundant Array (HURA) made up of 127 hexagonal cells of which 63 are opaque to the radiation (95 % opaque @ 1 MeV) and 64 are transparent to gamma-radiation (60 % transparent @ 20 keV & 80 % transparent @ 60 keV). The pattern has a 120° symmetry and the cells are of size 60 mm side-to-side (i.e. short axis) by 67.55 (i.e. long axis) forming a hexagonal-shaped coded area of overall dimensions 692.72 mm (i.e. short axis) by 770 mm (i.e. long axis). The opaque elements are made of 3 cm thick tungsten.

3.4.4 The X-ray monitor JEM-X

The JEM-X monitor works simultaneously with the other instruments in the energy range between 3 and 35 keV with an angular resolution of one arcmin and a FCFOV of 4.8 °. The coded mask is placed 3.4 m above the detector. The detector consists of two identical chambers filled with Xenon at a pressure of 1.5 bar (see Table 3.3).

3.4.5 The optical monitor OMC

The Optical Monitoring Camera (OMC) is a CCD detector of 1024×1024 pixels located in the focal plane of a 50 mm lens with a Visible (V) filter. The size of each pixel is $13 \times 13 \mu\text{m}$ covering a field of 17.6×17.6 arcsec. The total field of view of the OMC camera is of 5×5 degrees. The camera

Table 3.3: An overview of the JEM-X scientific capabilities.

Energy Range	3 keV–35 keV
Continuum sensitivity, at 3σ and 10^6 s integration ($\text{ph cm}^{-2} \text{s}^{-1} \text{keV}^{-1}$)	1.3×10^{-5} @ 6 keV
Line sensitivity, at 3σ and 10^6 s integration	1.7×10^{-5} ($\text{ph cm}^{-2} \text{s}^{-1}$) @ 6keV
Spectral Resolution	1.2 keV @ 10 keV
Angular resolution (FWHM)	~ 3 arcmin
Point Source Location Accuracy	$< 30''$ (10 σ source)
Timing accuracy (3σ)	122 μs
Field of View	4.8° (fully coded)

is placed on top of the satellite and is sensitive to stars of magnitude up to about 18.

3.5 A comparison with some X-ray detectors

In present work, the data supplied by INTEGRAL have been implemented with observational data provided by other X-ray instruments: XMM-Newton, Swift/XRT, Swift/BAT. The XMM-Newton and Swift/XRT telescopes work in the 0.2-10 keV energy range. The use of data provided by these instruments is mandatory for our aim of performing a broad-band analysis of our targets. It is well known that the XMM-Newton instrument is a quite more efficient detector with respect to Swift/XRT instrument. So we always adopted the XMM-Newton data when available.

The Swift/BAT instrument is sensitive in the spectral energy range 15–200 keV, and its data have been adopted for those objects (see Chapter 4) not yet included in the Third INTEGRAL catalog that was the release available at the time we started this work.

It is worthy briefly summarizing the characteristics and the general scientific objectives of these instruments. A basic comparison of the properties of the low energy instruments XMM-Newton and Swift/XRT is given in Table 3.4. Table 3.5 lists the main characteristics of the Swift/BAT instrument and for comparison also the INTEGRAL ones.

XMM-Newton was designed specifically to investigate in detail the X-ray emission characteristics, i.e. the emission distributions, the spectra and the temporal variability, of cosmic sources down to a limiting flux of order 10^{-15} $\text{erg}/(\text{s cm}^2)$. With its high throughput and moderate angular resolution, XMM is extremely sensitive to low surface brightness X-ray emission.

The XMM-Newton spacecraft carries a set of three X-ray CCD cameras,

comprising the European Photon Imaging Camera (EPIC). Two of the cameras are MOS (Metal Oxide Semi-conductor) CCD arrays (referred to as the MOS cameras). They are installed behind the X-ray telescopes that are equipped with the gratings of the Reflection Grating Spectrometers (RGS). The gratings divert about half of the telescope incident flux towards the RGS detectors such that (taking structural obscuration into account) about 44% of the original incoming flux reaches the MOS cameras. The third X-ray telescope has an unobstructed beam; the EPIC instrument at the focus of this telescope uses pn CCDs and is referred to as the pn camera (for details see <http://xmm.esac.esa.int>).

Some astronomical sources are prominent X-ray emitters, but faint or even invisible in other parts of the electromagnetic spectrum. Therefore, high-quality X-ray observations of these objects are very important and cannot be replaced by data obtained through other observing techniques. Instead, X-ray observations supplement data from other wavebands, leading to a more complete picture of the universe. Other objects are bright not only in the X-ray, but also in other parts of the spectrum, e.g. the optical or UV. Due to internal reprocessing, some sources emit both X-rays and other photons, but the optical or UV emission sometimes lags the X-ray light. Therefore, to further broaden the scope of the investigations, the Optical Monitor (OM) on board XMM offers the possibility to simultaneously study the optical/UV properties of the observed X-ray sources.

In the past, many X-ray observations suffered from weaknesses in spectral resolution, limited width of energy bandpass, lack of simultaneous optical/UV data, insufficient timing resolution or combinations of these. On the contrary, XMM-Newton allows for spectroscopy of X-ray sources with a spectral resolution of about 3.5 eV at 1 keV energy. This, in conjunction with XMM's large effective area and its well-sampled Line Spread Function (LSF), enables users to obtain high signal-to-noise spectra in the energy range from 0.35 to 2.5 keV (together with moderate resolution imaging spectroscopy over the 0.1 to 15 keV band) for detailed investigations of the diagnostic lines in the spectra of AGNs. The fact that the XMM bandpass reaches to an energy of 15 keV is important, because one can penetrate very deep into the central area of an AGN at high energies due to the low absorption cross section of high-energy X-rays in interstellar matter.

Swift is a multi-wavelength space-based observatory dedicated to the study of Gamma-Ray Burst (GRB) science. Its three instruments (BAT, XRT, UVOT) work together to observe GRBs and their afterglows in the gamma-ray, X-ray, ultraviolet, and optical wavebands. Based on continuous scans of the area of the sky which one of the instruments monitors (BAT), Swift uses momentum wheels to autonomously slew into the direction of possible GRBs.

The XRT telescope on board Swift can take images and perform spectral

analyses of the GRB afterglow. This provides more precise location of the GRB, with an error circle of approximately 3.5 arcseconds radius. The XRT is also used to perform long term monitoring of GRB afterglow light-curves for days to weeks, depending on the brightness of the afterglow. The XRT is primarily composed of the X-ray mirrors from the JET-X mission, with the detector upgraded to a single MOS CCD similar to those used by the XMM-Newton EPIC MOS cameras. The energy range of this instrument is: 0.2 – 10 keV.

One of the most important instruments on board of the Swift satellite is the Burst Alert Telescope (BAT), it detects GRBs events and computes its coordinates in the sky. It covers a large fraction of the sky (over one steradian fully coded, three steradians partially coded by comparison, the full sky solid angle is 4π or about 12.6 steradians) and locates the position of each event with an accuracy of 1 to 4 arc-minutes within 15 seconds. This crude position is immediately relayed to the ground and some wide-field, rapid-slew ground telescopes can catch the GRB with this information. BAT uses a coded-aperture mask of 52,000 randomly placed 5 mm lead tiles, 1 metre above a detector plane of 32,768 four mm CdZnTe hard X-ray detector tiles. As already noted, the energy range of this instrument is between 15 and 200 keV.

We note that due to its multi-wavelength capacity, Swift has become also an important observatory for studies of AGNs (non-GRB science). Swift covers the critical optical/UV to X-ray range where most of the accretion power in an AGN is released. In fact, key areas of Swift non-GRB science are BAT sky survey and AGN studies. Since the publication of the 9-months BAT survey (Tueller et al. 2008) the number of energy channels has been increased and the number of sources with accurate average spectra has been substantially increased. In its first 22 months, the BAT survey has reached a sensitivity of 0.8 mCrab over 80% of the sky. It has detected ~ 583 sources across the sky including 235 AGN (Tueller et al. 2009).

XMM-Newton has enormously improved capabilities compared to Swift/XRT. It is important to note that for the X-ray imaging, Swift/XRT was equipped only with a telescope, whereas XMM-Newton has three telescopes: MOS1, MOS2 and PN EPIC cameras.

Some special strengths of XMM-Newton are e.g.:

- extreme sensitivity to extended emission;
- the capability of performing high-resolution spectroscopy (with the RGS instrument) with simultaneous medium-resolution spectroscopy and imaging (EPIC) and optical/UV observations (the OM detector);
- the high sensitivity of XMM-Newton EPIC camera at high energies;
- excellent low energy response down to 0.15 keV;

- the high time resolution of XMM-Newton with the EPIC camera.

As far as it concerns the Swift/BAT instrument, due to an average positional uncertainty of $1.7'$ and a sensitivity limit of a few times $10^{-11} \text{ erg cm}^{-2} \text{ s}^{-1}$ in the 14 – 195 keV band, the BAT data are about 10 times more sensitive than the previous all-sky hard X-ray survey and the positions are accurate enough to allow unique identifications of nearly all of the sources. Some particular advantages of Swift/BAT are:

- it can detect sources to $\sim 8^\circ$ from the Sun;
- it can detect sources anywhere in the anti-Sun hemisphere;
- it covers $\sim 60\%$ of the sky each day;
- it can automatically provide hard X-ray light curves with minimal gaps.

When comparing the Swift/BAT and INTEGRAL performances in the AGN Surveys, the following similarities and differences can be found:

- Similar in design and performance;
- INTEGRAL/IBIS spectral coverage is extended up to 300 – 500 keV and spectral resolution is much better allowing for better spectra.
- INTEGRAL exposures of a few 10^7 s should be about 6 times more sensitive than SWIFT/BAT;
- Swift/BAT has more sky coverage;
- the Swift/BAT AGN discovery rate is about 4 times larger than that of INTEGRAL;
- Swift/BAT sensitivity improves as $t_{obs}^{1/2}$;
- Swift/XRT allows associations to be made with counterparts in the hard X-ray energy band.

Therefore, it is evident that INTEGRAL and Swift/BAT telescopes are complementary and AGN observations can take advantage of the strengths of each mission.

Table 3.4: XMM-Newton and Swift/XRT parameters.

	MOS	PN	XRT
Energy Range	0.2 – 12 keV	0.2 – 12 keV	0.2 keV – 10 keV
Effective area	360 (at 0.4 keV) cm ²	771 (at 0.4 keV) cm ²	110 cm ² (at 1.5 keV)
Field of view	30'	30'	23.6×23.6'
Angular resolution	~ 6"	~ 6"	18" (at 1.5 keV)
Energy resolution	45 eV (at 0.4 keV)	45 eV (at 0.4 keV)	145 eV (at 5.9 keV)
Sensitivity (in 10 ⁴ s)	2 10 ⁻¹⁴ erg cm ⁻² s ⁻¹ (in 2 – 10 keV)	10 ⁻¹⁴ erg cm ⁻² s ⁻¹ (in 2 – 10 keV)	2 10 ⁻¹⁴ erg cm ⁻² s ⁻¹

Table 3.5: An overview of the Swift/BAT and INTEGRAL Surveys.

	Swift/BAT	INTEGRAL
Energy Range	14 – 195 keV	15 keV – 10 MeV
Area	5200 cm ²	2600 cm ²
Field of view	2 Steradian Partially Coded	0.24 Steradian Partially Coded
Equivalent Fully Coded Exposure	~ 1 – 2 Ms/yr (all sky)	> 10Ms/yr (selected fields)
Background	~ 7000 count/s	~ 700 count/s
Sensitivity	few 10 ⁻¹¹ erg cm ⁻² s ⁻¹ at 9 months	few 10 ⁻¹² erg cm ⁻² s ⁻¹
Observing strategy	Random pointings	Selected pointings

Chapter 4

Broad-band study of the Blazars observed with INTEGRAL

4.1 Introduction

Among the various instruments on board of INTEGRAL observatory (Winkler et al. 2003), the IBIS telescope (Ubertini et al. 2003), owing to its mCrab sensitivity on long exposures, large field of view ($\sim 28^\circ \times 28^\circ$), and good ($\sim 10'$) angular resolution (see Chapter 3 for more details) allows to collect data for a large sample of both bright (> 1 mCrab for Ms exposure) and weak hard X-ray sources and then to build up a large observational database.

In present work we have adopted the INTEGRAL/IBIS data, supplementing these data with the observations in the soft X-ray band 0.2 – 10 keV, in order to perform a broad-band analysis of Blazar objects. This approach is very useful to study the Reflection hump peaked at about 20 – 30 keV (and therefore also the reflecting medium properties) and the high energy cut-off characteristic of the primary continuum.

4.2 The INTEGRAL/IBIS selected sample

The INTEGRAL/IBIS total sample of sources is derived from the third IBIS/ISGRI survey catalog that includes 421 sources for a total exposure time of 40 Ms; 131 sources out of 421 have been identified as AGN. The survey input data set consists of all pointings data available at the time we started this project, from revolutions 12-429 inclusive, covering a time period of about three years. The details about this survey are presented in the work of Bird and collaborators (2007).

Among these objects we selected a small sample according to the following selection criteria:

- they are sources classified as blazars, as resulted from optical identification (e.g. Masetti et al. 2004, 2008)
- for each of them, soft X-ray data (in 0.2 – 10 keV energy band) are available.

Our sample, that is representative of INTEGRAL detected blazars, consists of 11 sources: 9 FSRQ objects with $0.15 < z < 3.67$ and 2 BL Lac objects with $z = 0.069$ and 0.086 , although seven out of nine FSRQ are from the third INTEGRAL catalog at the date when this work started (2007). For the other 2 objects, that are now included in the fourth INTEGRAL catalog (Bird et al. 2009) hard X-rays BAT data were adopted. The relevant information for our whole sample are given in Table 4.1 where we list the name of the source, the type, the optical coordinates, the redshift, the Galactic absorption along the line of sight according to Dickey & Lockman (1990). In the last column of Table 4.1 we also list the IBIS 20-100 keV flux derived by Bird et al. (2007) and the BAT 14-195 keV flux as reported by AGN Catalog of the first 9 months¹ of all sky survey data collected by the BAT coded mask hard X-ray instrument². We remark that the source with the IGR designation has been discovered in hard X-rays with INTEGRAL and so it is defined a hard X-rays INTEGRAL-detected source, this is the farthest object so far detected by INTEGRAL and its nature was determined a posteriori through optical spectroscopy (Bassani et al. 2007).

¹The data available at the time we started this project; in these last times, also the data corresponding to the first 22 months of the BAT survey became available

²The BAT data have been taken from the on-line archive at: [http : //swift.gsfc.nasa.gov/docs/swift/results/bs9mon](http://swift.gsfc.nasa.gov/docs/swift/results/bs9mon).

Table 4.1: Most relevant information for the sample of blazars observed with INTEGRAL, Swift and XMM-Newton.

<i>Source</i>	<i>Type</i>	R.A.	Dec	<i>redshift</i>	N_H^{Gal} [$10^{22} cm^{-2}$]	$F_{20-100keV}^{IBIS}$ ($F_{14-195keV}^{BAT}$) [$10^{-11} erg \cdot cm^{-2} \cdot s^{-1}$]
QSO B0836+710	FSRQ	08 41 24.37	+70 53 42.2	2.172	0.030	6
1ES 0033+595	BL Lac	00 35 52.63	+59 50 04.6	0.086	0.427	2
PKS 0537-286	FSRQ	05 39 54.28	-28 39 55.9	3.104	0.020	(3)
PKS 2149-307	FSRQ	21 51 55.52	-30 27 53.7	2.345	0.020	(5)
Swift J1656.3-3302	FSRQ	16 56 16.56	-33 02 09.3	2.4	0.220	2
IGR J22517+2218	FSRQ	22 51 53.50	+22 17 37.3	3.668	0.050	4
Bl Lac	BL Lac	22 02 42.72	+42 17 16.8	0.069	0.022	3
PKS 1830-211	FSRQ	18 33 39.89	-21 03 39.8	2.507	0.260	5
4C 04.42	FSRQ	12 22 22.55	+04 13 15.8	0.965	0.017	3
3C 273	FSRQ	12 29 06.70	+02 03 08.6	0.158	0.018	20
3C 279	FSRQ	12 56 11.17	+05 47 21.5	0.536	0.020	2

4.3 The hard X-ray data reduction

4.3.1 The INTEGRAL/IBIS and Swift/BAT data

The INTEGRAL data presented here are based on pointings with the IBIS instrument (Ubertini et al. 2003), collected over the period from end of 2002 up to April 2006 (revolution 12 up to 429). Images from the ISGRI detector (Lebrun et al. 2003) for each pointing have been generated in different energy bands using off-line scientific Analysis Software (Goldwurm et al. 2003) OSA version 5.1. Count rates at the source position have been extracted from individual images to provide light curves in different energy bands. We note that for building the third INTEGRAL catalog, the light curves have been used to derive the average spectra in 5 energy bands that have been chosen in order to be suitable for retrieving the properties of weak (~ 5 mCrab) objects. From light curves the average fluxes have been derived and combined to produce an average source spectrum (for details see Bird et al. 2007). These spectra collected in the framework of the Survey refer to 20 – 100 keV band.

The BAT data have been taken from the on-line archive (<http://swift.gsfc.nasa.gov/docs/swift/results/bs9mon>)

for the first 9 months of the BAT Survey and their reduction was described in Sambruna et al. 2006.

4.4 The soft X-ray data reduction

4.4.1 The XMM-Newton and Swift/XRT data

The seven blazars (3C 273, 1ES 0033+595, 4C 04.42, PKS 1830-211, QSO B0836-710, PKS 0537-286 and PKS 2149-306) are a combination of proprietary data and public observations obtained from the XMM-Newton Science Archive³. The raw EPIC Observation Data Files (ODFs) were obtained from the XMM Science Archive and reduced using the standard Science Analysis System (SAS) software package (v.7.1.0) and the most recent calibration files available at the time of the data reduction (2007). We used the EMCHAIN and EPCHAIN task for the pipeline processing of the ODFs to generate the corresponding event files. The spectra were created using X-ray events of pattern 0-12 for MOS and 0-4 for PN. The source counts were extracted from a circular region centred on the source with a radius of 20-40 arcsec and the background was derived from two nearby source-free circular regions of the same size. Spectra were re-binned using GRPPHA to have a minimum of 20 counts in each bin⁴, so that the CHI2 statistic could reliably

³<http://xmm.esac.esa.int/xsa/index.shtml>.

⁴10 counts are the minimum number of counts required to use the CHI2 minimization technique.

be used. Details of the XMM-Newton observations and the source observed count rates are summarized in Table 4.2.

Table 4.2: Information about the XMM-Newton observations and source observed count rates.

<i>Source</i>	Obs.ID	Date of obs.	Exp. time MOS1 (s)	Exp. time MOS2 (s)	Exp. time PN (s)	Counts/s MOS1 (0.2 – 10keV) (s ⁻¹)	Counts/s MOS2 (0.2 – 10keV) (s ⁻¹)	Counts/s PN (0.2 – 10keV) (s ⁻¹)
1ES 0033+595	0094381301	2003-02-01	1204	1535	4209	1.40 ± 0.04	1.41 ± 0.04	4.02 ± 0.04
4C 04.42	0401790601	2006-07-12	11515	11527	8842	0.24 ± 0.01	0.24 ± 0.01	0.89 ± 0.01
PKS 1830-211	0204580201	2004-03-10	30445	30444	20906	0.58 ± 0.01	0.56 ± 0.01	1.52 ± 0.01
QSO B0836-710	0112620101	2001-04-12	35614	35620	29035	3.88 ± 0.01	3.85 ± 0.01	11.97 ± 0.02
PKS 0537-286	0206350101	2005-03-20	80610	80765	64661	0.213 ± 0.002	0.222 ± 0.002	0.583 ± 0.003
PKS 2149-306	0103060401	2001-05-01	23959	23960	20287	0.63 ± 0.01	0.62 ± 0.01	1.67 ± 0.01
3C 273	0126700801	2000-06-17	56508	56526	42513	11.70 ± 0.02	11.23 ± 0.02	47.03 ± 0.03

Table 4.3: Information about the Swift/XRT observations and source observed count rates.

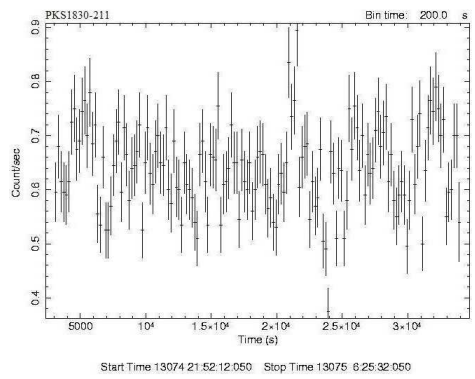
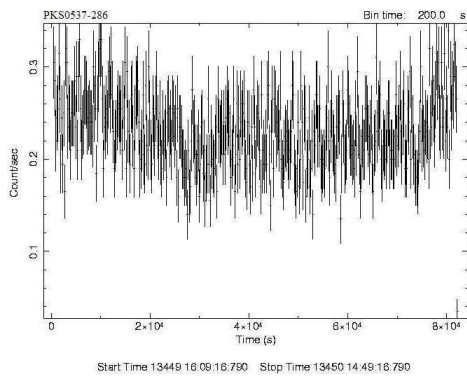
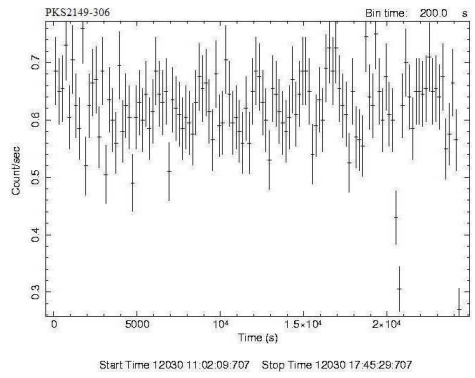
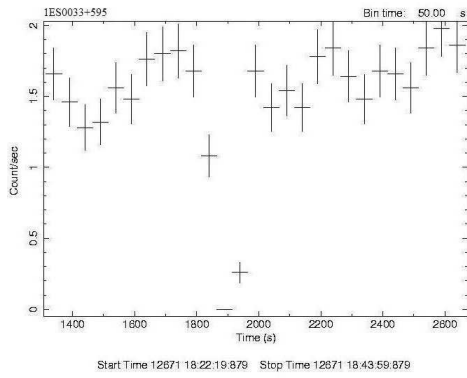
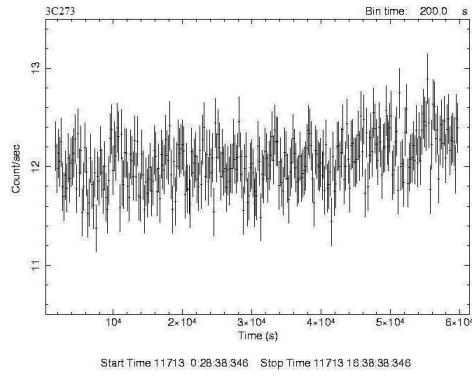
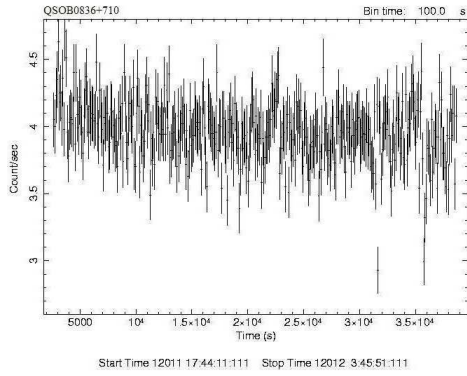
<i>Source</i>	Obs.ID	Date of obs.	Exp. time XRT (s)	Counts/s XRT (s^{-1})
BL Lac	00090042010	2008-08-29	5806	0.20 ± 0.01
IGR J22517+2218	00036660001	2007-05-26	8300	0.054 ± 0.003
Swift J1656.3-3302	00035272002	2006-06-13	4785	0.075 ± 0.004
3C 279	00035019009	2008-11-26	22580	0.198 ± 0.003

Swift/XRT data reduction of four blazars (IGR J22517+2218, 3C 279, BL Lac and Swift J1656.3-3302) was performed using the tool XSELECT v. 2.4. Events for spectral analysis were extracted within a circular region of radius 20 arcsec centred on the source position. The background was extracted from a circular region with the same radius and located far from the source. In all cases, the spectra were binned using GRPPHA. We used Ancillary Response Files (ARFs) and Response Matrix Files (RMFs) available for download from the HEASARC Calibration Database (caldb) at: http://heasarc.gsfc.nasa.gov/docs/heasarc/caldb/caldb_intro.html. Table 4.3 lists the observation ID, the observation start time, the integration time and the observed count rate.

4.5 The XMM and XRT timing analysis

Before extracting the spectra of the sources, the soft X-ray light-curves were produced to investigate their variability (see plots in Figures 4.1 and 4.2). By analyzing the trend of the light curves, most of the observations showed intermittent background flaring, so these time slots were subsequently ignored for the spectral analysis.

In all cases, but one (see plot of 3C279 in Figure 4.2), we have not observed any change in the rate (counts/s) with respect to average value larger than about 30%. In view of the fact that we are investigating the average properties of the Blazars, we have decided to consider the whole time interval not only for the sources that do not show significant variation with the time, but also for the Blazar 3C 279.



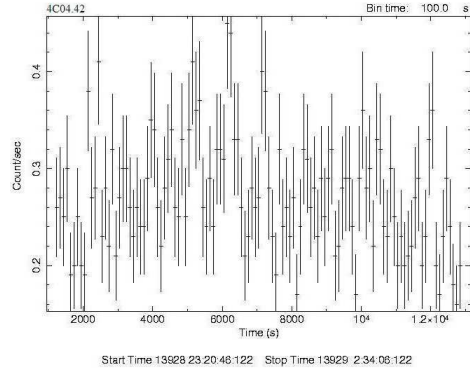


Figure 4.1: The light curves (0.2 – 10 keV) of the sources observed with XMM-Newton MOS1 camera.

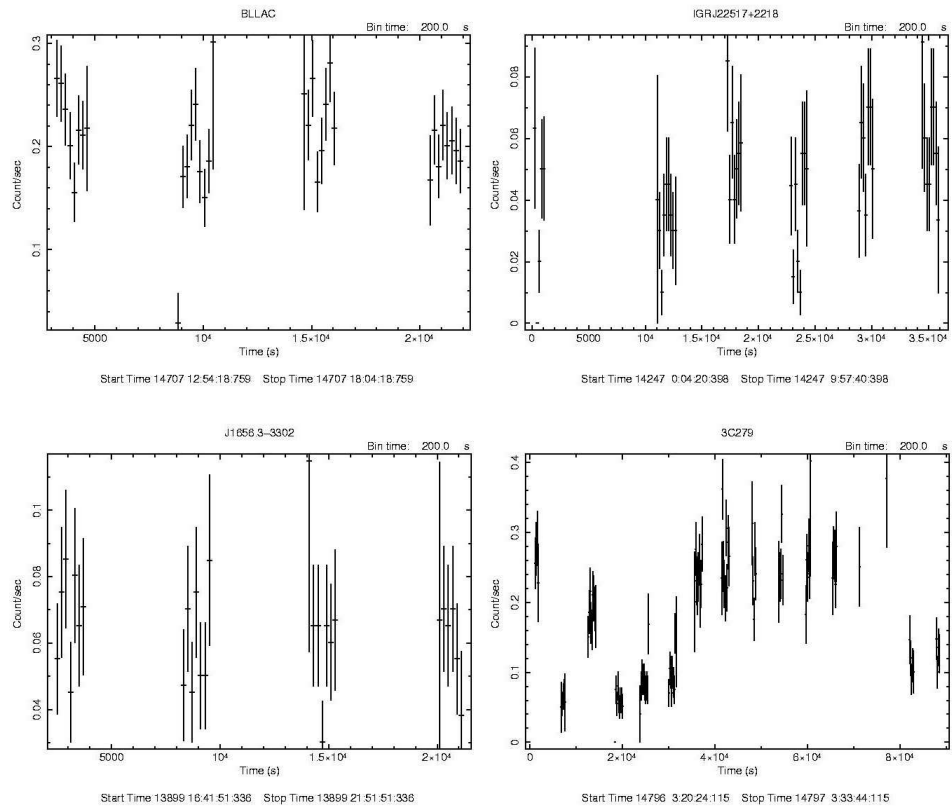


Figure 4.2: The light curves (0.2–10 keV) of the sources observed with Swift/XRT instruments.

4.6 Broad-band spectral analysis: 0.2 – 100 keV

The result of the data reduction process described in the previous section provides different spectra, one for each of the different instruments. The X-ray spectral analysis was performed by combining the different data from each instrument using the X-ray SPECTral fitting software XSPEC v. 11.3.2 (Arnaud 1996). The errors are quoted at 90% confidence level for one interesting parameter. Throughout this work, a WMAP (Wilkinson Microwave Anisotropy Probe) Cosmology of $H_0 = 70 \text{ km s}^{-1} \text{ Mpc}^{-1}$, $\Omega_\lambda = 0.73$ and $\Omega_m = 1 - \Omega_\lambda$ is assumed. We have combined XMM spectrum with the INTEGRAL one for the blazars 3C 273, 1ES 0033+595, 4C 04.42, PKS 1830-211, QSO B0836-710, XRT spectrum with the INTEGRAL one for the blazars 3C 279, BL Lac, IGR J22517+2218, Swift J1656.3-3302 and XMM spectrum with the BAT one for the blazars PKS 0537-286, PKS 2149-306. A multiplicative constant factor (C) has been introduced to account for possible cross-calibration mismatches between instruments as well as to take into account flux variations between the observing periods. In general, the calibration between the various satellites is performed analyzing the Crab spectrum. In fact, since the Crab spectrum is simple and not variable, from the late 1970s on, the Crab was used as a standard X-ray calibration source for all missions. In particular, various studies of the Crab spectrum (e.g. Kirsch et al. 2004 and 2005) have shown that the inter-calibration XMM/INTEGRAL and Swift/INTEGRAL is close to 1 (within a few percent). We remark that, since the XMM, Swift and INTEGRAL observations were not simultaneous, flux variations are plausible given the blazar-nature of the analyzed objects. Given that the inter-calibration constant C between the two instruments is ~ 1 , we suggest that, a different value for this constant is likely to be due to the flux variability just mentioned. In our analysis, this constant C between two instruments at low and high energies has been allowed to vary freely in the fits. In particular, we have considered the MOS1 and XRT instruments as reference detectors in the case of XMM-INTEGRAL or BAT data and XRT-INTEGRAL data, respectively. Therefore, the inter-calibration constants in our fitting procedure are MOS2/MOS1, PN/MOS1, INTEGRAL/MOS1, BAT/MOS1 and INTEGRAL/XRT. However MOS2/MOS1 and PN/MOS1 are always close to 1 within few percent.

In order to reproduce the shape of the intrinsic continuum of our sources we fitted the combined spectra (0.2 – 100 keV) of each source with several models.

At first, we have tried to fit the spectra of our sources in the 3 – 100 keV energy band with the model *A*, that corresponds to a simple power-law absorbed by gas of the Milky Way. The results of the fit are summarized in Table 4.4. This model provides a good fit for all sources. When extrapolating

the model A to the low energy range, we obtained a very poor fit in all cases but one (PKS 2149-307). In fact the data to model ratio (see Figure 4.3), constructed by fitting a simple power-law over the observed frame 3 – 100 keV and extrapolating⁵ over 0.2–100 keV, shows a clear systematic residuals on the lower energy side (below ~ 3 keV in the observer frame). From the data/(model A) ratios shown in Figure 4.3, we can see that the spectra of the majority of the sources (but 4C 04.42 and 3C 273) clearly show a deficit of soft X-ray counts with respect to the simple power-law model, indicating the possible presence of excess absorption and/or of an energy break in the intrinsic continuum.

⁵This procedure is used to show the possible presence of a deficit or an excess in counts with respect a continuum well fitted by a power-law.

Table 4.4: Best fit parameters of a simple power-law model in 3 – 100 keV energy range (model A).

Model A						
Name	${}^1F_{ob(2-10keV)}$	${}^1F_{ob(20-100keV)}$	${}^3\Gamma$	4c	${}^5\chi_r^2/\text{dof}$	${}^6P_{null}$
QSO B0836+710	4.1	5.2	1.34 ± 0.02	0.28 ± 0.03	0.91/1521	0.996
1ES 0033+595	1.1	1.5	$2.52_{-0.17}^{+0.18}$	$4.2_{-1.6}^{+2.5}$	0.79/53	0.865
PKS 0537-286	0.5	2.3	1.19 ± 0.06	0.6 ± 0.2	1.05/329	0.253
PKS 2149-307	0.6	4.9	1.41 ± 0.06	1.9 ± 0.5	0.91/225	0.835
PKS 1830-211	1.4	4.4	1.22 ± 0.04	0.5 ± 0.1	1.03/442	0.315
Swift J1656.3-3302	0.5	2.1	$1.60_{-0.32}^{+0.33}$	$1.6_{-0.9}^{+2.0}$	1.02/18	0.434
IGR J22517+2218	0.3	3.8	$1.43_{-0.56}^{+0.59}$	$4.1_{-3.1}^{+11.4}$	0.66/14	0.817
Bl Lac	0.6	2.3	$2.01_{-0.41}^{+0.43}$	$4.3_{-2.6}^{+6.5}$	0.589/11	0.840
4C 04.42	0.3	1.7	$1.26_{-0.10}^{+0.20}$	1.2 ± 0.2	1.02/110	0.429
3C 273	7.9	17.2	1.61 ± 0.01	0.88 ± 0.03	1.06/1267	0.066
3C 279	0.5	2.1	$2.00_{-0.23}^{+0.24}$	$4.3_{-1.8}^{+3.1}$	1.06/19	0.382

¹ Observed flux in the 2 – 10 keV (and 20 – 100 keV) energy range in units of $10^{-11}\text{erg cm}^{-2} \text{ s}^{-1}$. ³ Photon index, related to the spectral index α (where $F \propto \nu^{-\alpha}$) by $\alpha = \Gamma - 1$. ⁴ IBIS/MOS, BAT/MOS or IBIS/XRT cross-calibration constant. ⁵ Reduced chi-squared to degrees of freedom. ⁶ Null hypothesis probability.

In order to properly reproduce such a feature we have tested the impact of different models.

In the model *B* we added an extra absorption (in the rest-frames of the sources) to fit the broad-band data of objects showing the deficit of low energy events (phabs * zphabs * zpo model in XSPEC). The results of model *B* are presented in Table 4.5.

All sources that show a deficit of soft X-ray counts with respect to the simple power-law model, with the exception of PKS 2149-307 and PKS 1830-211, were well fitted with the model *B*. For PKS 2149-307 we have obtained an upper limit value on the intrinsic absorbing column density and for PKS 1830-211 the model *B* produces a poor quality fit to the data. We will discuss the case of this source in more detail later on.

The X-ray spectra and the best-fit models with a redshifted absorption component at the quasar redshift are shown in Figure 4.4.

Successively, we also tested a broken power-law in the model *C* (phabs * bknpo model in XSPEC) for the whole sample. The results of this model are shown in Table 4.6. The model *C* did not improve the fit further in the majority of the cases and, also in those cases for which a slightly better χ^2 is obtained, the null hypothesis probability increases only a few per cent with respect to the model *B*. Although this result suggests that strong statistical evidence does not exist for a broken power-law respect to the absorbed one, however the presence of an intrinsic spectral break cannot be excluded.

The X-ray spectra and the best-fit models with a broken power-law are shown in Figure 4.5.

For PKS 1830-211, both models *B* and *C* fail to reproduce source data. PKS 1830-211 is a gravitationally lensed galaxy and the excess absorption can be attributed to the intervening galaxy at redshift $z = 0.89$. The best-fit of the observed spectrum requires both an absorber and a broken power-law (model *D*), confirming the results reported by Zhang and collaborators (2008) with the three XMM-Newton observations (Obs.ID 0204580201, 0204580301 and 0204580401) and at the time available INTEGRAL observation (up to April 29, 2006). In fact, in addition to the excess cold absorption, PKS 1830-211 also exhibits an energy break at about 4 keV in the observer frame. Table gives the results of this best-fit model.

The X-ray spectrum and the best-fit model with a broken power-law and a redshifted absorption component produced by the lens galaxy at redshift $z = 0.89$ is shown in Figure 4.6.

Finally, we also checked a Compton Reflection component with a power-law reflected from neutral matter (pexrav model in XSPEC, Magdziarz & Zdziarski, 1995): this model produces a worst fit for all sources. In addition, no evidence for an iron line emission is detected. In fact, to the best fitting model, we also tried the addition of an extra narrow Gaussian line (centered around 6.4 keV and redshifted in the quasar frame corresponding to neutral iron line $K\alpha$) to account for the AGNs iron line emission: however this

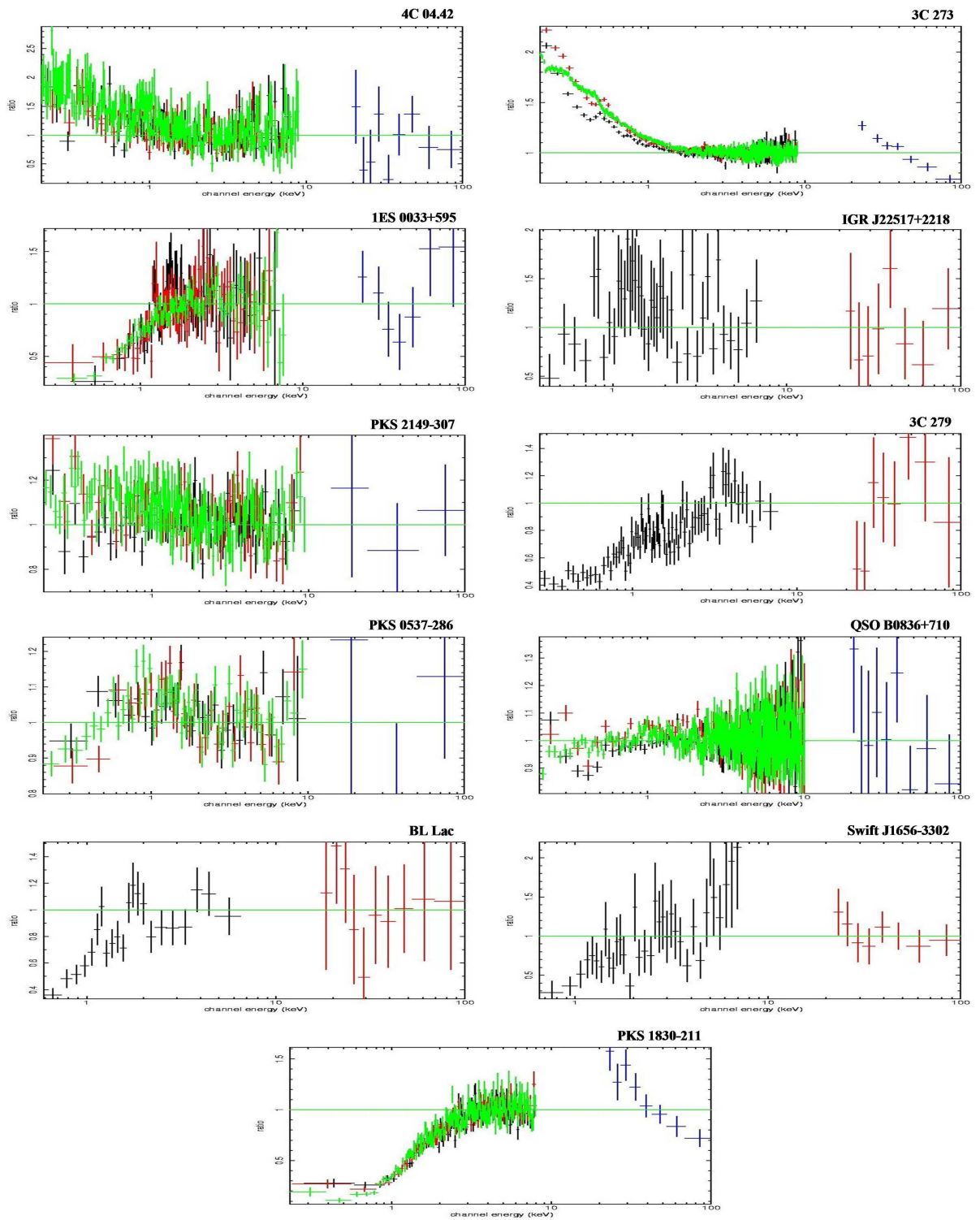


Figure 4.3: The data to model *A* as obtained by fitting a simple power-law over the observed frame 3 – 100 keV and extrapolating over the 0.2 – 100 keV range.

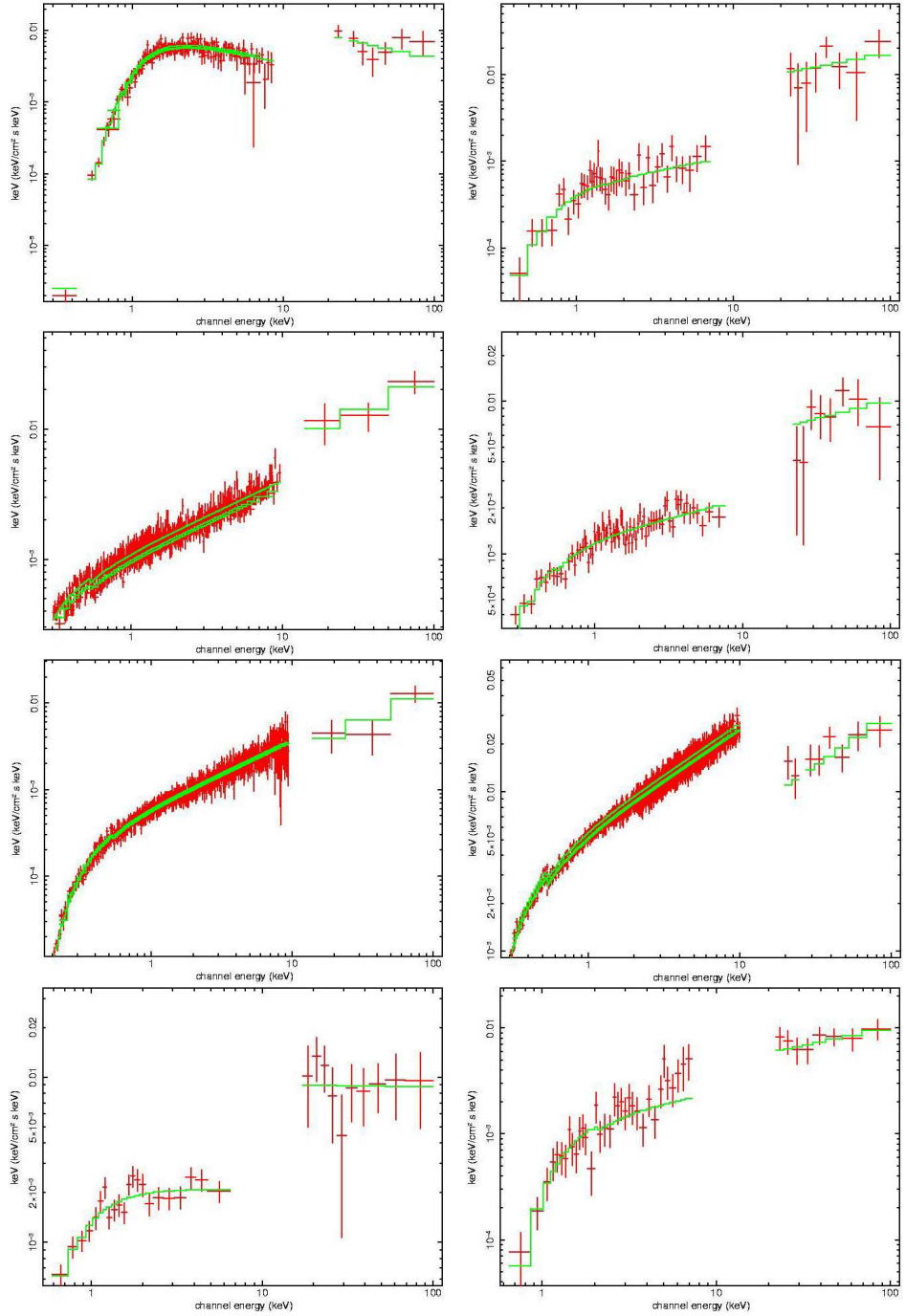


Figure 4.4: The νF_ν plot (in $\text{keV cm}^{-2} \text{s}^{-1}$) of the sources obtained by fitting the spectrum with a power-law and an intrinsic cold absorption in excess to the Galactic one. Left column, from top to bottom: 1ES0033+595, PKS2149-307, PKS0537-286 and BL Lac; right column, from top to bottom: IGRJ22517+2218, 3C279, QSOB0836+710 and SwiftJ1656-3302.

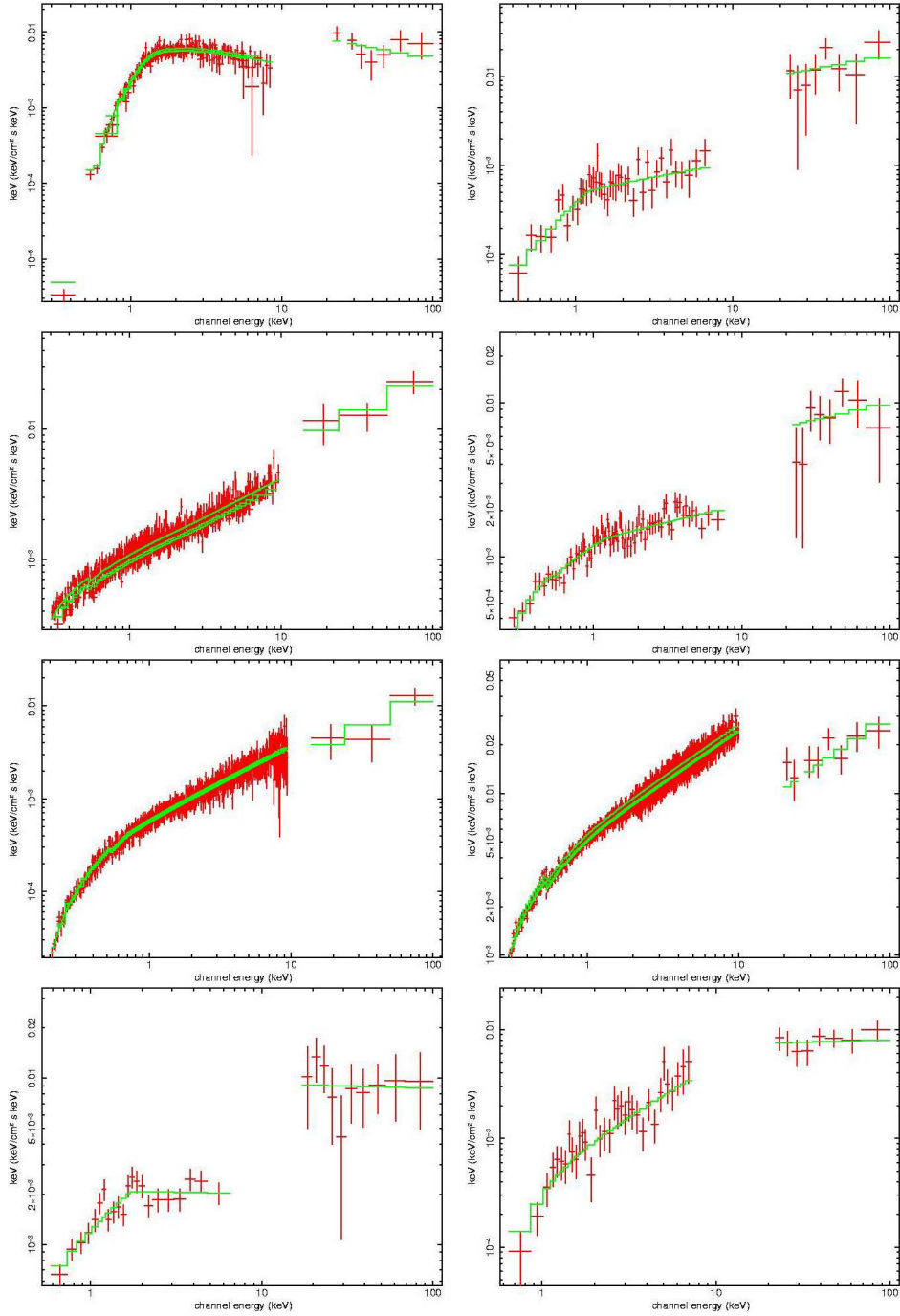


Figure 4.5: The νF_ν plot (in $\text{keV cm}^{-2} \text{s}^{-1}$) of the sources obtained by fitting the spectrum with a broken power-law. Left column, from top to bottom: 1ES0033+595, PKS2149-307, PKS0537-286 and BL Lac; right column, from top to bottom: IGRJ22517+2218, 3C279, QSOB0836+710 and SwiftJ1656-3302.

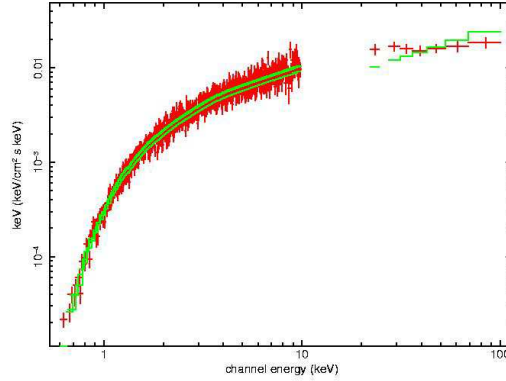


Figure 4.6: The νF_ν plot of PKS 1830-211 obtained by fitting the spectrum with a broken power-law and an absorption associated to the lens galaxy ($z \sim 0.89$).

feature is not required by the data. The upper limit on the Equivalent Width (EW)⁶ of the nuclear iron line varies between 4 and 571 eV for the whole selected sample. In particular, for the sources QSO B0836+710, PKS 0537-286, PKS 2149-307, PKS 1830-211 and Swift J1656.3-3302 the upper limit on the EW is of the order a few eV and for the blazars 3C 279, 1ES 0033+595, IGR J22517+2218 and BL Lac it is about a few hundred of eV. Therefore, we can exclude the presence of the Reflection features in these absorbed RL objects.

⁶The EW is defined as the width of a rectangle centered around the spectral line having the same area of the line and it is directly proportional to the line photon flux.

Table 4.5: Best fit parameters of an absorbed power-law model (model *B*).

Model <i>B</i>							
Name	${}^1F_{ob(2-10keV)}$	${}^1F_{ob(20-100keV)}$	2N_H	${}^3\Gamma$	4c	${}^5\chi_r^2/\text{dof}$	${}^6P_{null}$
QSO B0836+710	4.0	4.9	0.07 ± 0.02	1.353 ± 0.005	0.28 ± 0.03	1.02/2421	0.206
1ES 0033+595	1.2	1.5	0.20 ± 0.02	2.47 ± 0.05	3.5 ± 0.8	0.81/229	0.985
PKS 0537-286	0.5	2.3	0.30 ± 0.05	1.22 ± 0.01	0.7 ± 0.2	1.03/972	0.235
PKS 2149-307	0.6	4.8	< 0.05	1.45 ± 0.01	2.1 ± 0.5	0.99/849	0.543
Swift J1656.3-3302	0.5	2.0	$7.9^{+5.1}_{-3.8}$	$1.66^{+0.22}_{-0.20}$	$1.9^{+1.7}_{-0.9}$	1.03/42	0.422
IGR J22517+2218	0.2	3.5	$3.6^{+3.3}_{-2.2}$	$1.66^{+0.21}_{-0.19}$	$7.1^{+6.7}_{-3.4}$	0.85/49	0.770
Bl Lac	0.5	2.3	0.20 ± 0.07	$2.01^{+0.17}_{-0.16}$	$4.3^{+2.8}_{-1.7}$	0.81/31	0.762
3C 279	0.5	2.2	0.04 ± 0.02	1.75 ± 0.06	$2.5^{+0.7}_{-0.6}$	1.07/79	0.311

¹ Observed flux in the 2 – 10 keV (and 20 – 100 keV) energy range in units of $10^{-11} \text{erg cm}^{-2} \text{s}^{-1}$. ² Intrinsic column density of hydrogen in units of 10^{22}cm^{-2} . ³ Photon index, related to the spectral index α (where $F \propto \nu^{-\alpha}$) by $\alpha = \Gamma - 1$. ⁴ IBIS/MOS, BAT/MOS or IBIS/XRT cross-calibration constant. ⁵ Reduced chi-squared to degrees of freedom. ⁶ Null hypothesis probability.

Table 4.6: Best fit parameters of a broken power-law model (model *C*).

Model <i>C</i>							
Name	¹ $F_{ob(2-10keV)}$	¹ $F_{ob(20-100keV)}$	⁷ Γ_1, Γ_2	⁸ E_b	⁴ c	⁵ χ_r^2/dof	⁶ P_{null}
QSO B0836+710	4.0	4.9	$1.26^{+0.01}_{-0.02}$ 1.354 ± 0.005	0.98 ± 0.08	0.28 ± 0.03	1.02/2420	0.274
1ES 0033+595	1.2	1.6	$1.38^{+0.16}_{-0.13}$ $2.37^{+0.06}_{-0.05}$	$1.39^{+0.12}_{-0.10}$	$2.8^{+0.7}_{-0.6}$	0.85/228	0.947
PKS 0537-286	0.5	2.3	$0.83^{+0.09}_{-0.12}$ 1.21 ± 0.01	0.72 ± 0.09	0.7 ± 0.2	1.03/971	0.282
PKS 2149-307	0.6	4.8	$1.47^{+0.01}_{-0.02}$ $1.41^{+0.04}_{-0.34}$	$2.7^{+4.5}_{-1.1}$	1.9 ± 0.5	0.99/848	0.579
Swift J1656.3-3302	0.6	2.0	$1.03^{+0.17}_{-0.47}$ $1.96^{+0.30}_{-0.27}$	$8.3^{+45.5}_{-3.4}$	$1.8^{+2.2}_{-1.4}$	0.87/41	0.708
IGR J22517+2218	0.2	3.5	$0.58^{+0.49}_{-0.69}$ $1.69^{+0.23}_{-0.19}$	$1.19^{+0.27}_{-0.26}$	$7.8^{+8.4}_{-3.7}$	0.82/48	0.803
Bl Lac	0.5	2.2	$1.06^{+0.57}_{-0.73}$ $2.02^{+0.34}_{-0.12}$	$1.71^{+0.75}_{-0.15}$	$4.6^{+1.7}_{-1.0}$	0.89/30	0.633
3C 279	0.5	2.2	$1.46^{+0.10}_{-0.11}$ 1.78 ± 0.06	$1.16^{+0.27}_{-0.20}$	$2.7^{+0.8}_{-0.7}$	1.01/78	0.446

¹ Observed flux in the 2 – 10 keV (and 20 – 100 keV) energy range in units of $10^{-11} \text{erg cm}^{-2} \text{s}^{-1}$. ⁴ IBIS/MOS, BAT/MOS or IBIS/XRT cross-calibration constant. ⁵ Reduced chi-squared to degrees of freedom. ⁶ Null hypothesis probability. ⁷ Spectral index below the break (Γ_1) and above the break (Γ_2). ⁸ Observed break energy in units of keV.

Table 4.7: Best fit parameters of a broken power-law model with an absorption in excess for PKS 1830-211 (model *D*).

Model <i>D</i>								
Name	¹ $F_{ob(2-10keV)}$	¹ $F_{ob(20-100keV)}$	² N_H	⁷ Γ_1, Γ_2	⁸ E_b	⁴ c	⁵ χ_r^2/dof	⁶ P_{null}
PKS 1830-211	1.4	4.3	$1.5^{+0.2}_{-0.1}$	0.95 ± 0.05	$4.01^{+0.42}_{-0.54}$	$0.8^{+0.3}_{-0.2}$	1.06/856	0.101
				$1.32^{+0.10}_{-0.07}$				

¹ Observed flux in the 2 – 10 keV (and 20 – 100 keV) energy range in units of $10^{-11}\text{erg cm}^{-2} \text{ s}^{-1}$. ² Intrinsic column density of hydrogen in units of 10^{22}cm^{-2} at redshift of the lens galaxy ($z = 0.89$). ³ Photon index, related to the spectral index α (where $F \propto \nu^{-\alpha}$) by $\alpha = \Gamma - 1$. ⁴ IBIS/MOS, BAT/MOS or IBIS/XRT cross-calibration constant. ⁵ Reduced chi-squared to degrees of freedom. ⁶ Null hypothesis probability. ⁷ Spectral index below the break (Γ_1) and above the break (Γ_2). ⁸ Observed break energy in units of keV. ⁹ Black-body temperature in the source rest-frame in units of keV. ¹⁰ Temperature at inner disk radius in the observer-frame in units of keV.

Two intriguing cases are represented by the FSRQs 4C 04.42 and 3C 273 because they are the only sources of our sample that show a significant evidence for the presence of possible soft excess component.

4C04.42 is equally well fitted by an unabsorbed power-law with a multi-temperature disk emission (model *F*, `ph * zpo * diskbb` in XSPEC, with multiple black-body components working from the temperature at the inner disc radius) that provides a $kT \sim 0.26$ keV in the observer frame or with a simple black-body thermal emission (model *E*, `ph * zpo * zbb` in XSPEC) providing a $kT \sim 0.19$ keV in the quasar rest-frame. Also in this particular case, the alternative model of broken power-law (with the following best-fit parameters $\Gamma_1 = 1.57^{+0.04}_{-0.05}$, $\Gamma_2 = 1.16^{+0.08}_{-0.12}$ and $E_b = 2.19^{+0.62}_{-0.37}$ keV in the observer frame) did not significantly improve the result.

Finally, no evidence for an iron line emission is detected when we add Gaussian line component to both models of multi-temperature disk emission and thermal emission of black-body (the upper limit on the EW is of the order a few eV). The results of these fits are shown in Table 4.8. The X-ray spectra and the best-fit models are shown in Figure 4.7.

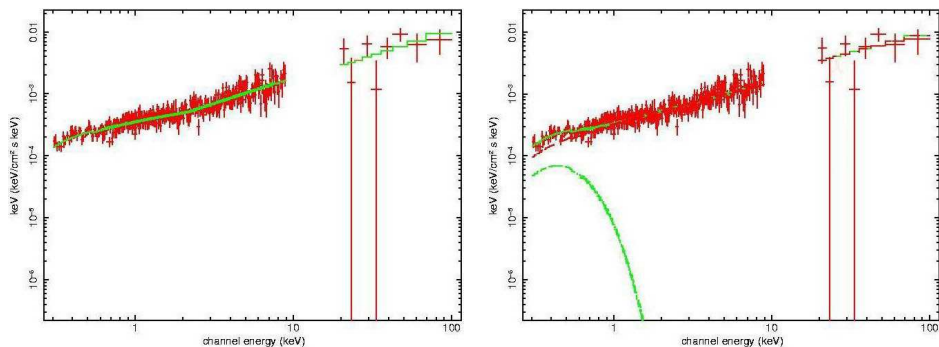


Figure 4.7: The νF_ν plot of 4C 04.42 obtained by fitting the spectrum with two different best-fit models: a broken power-law model (on the left) and a power-law model with a simple thermal emission of black-body (on the right).

The broad-band spectrum of 3C 273 has been fitted with different models: a broken power-law (see model *C* in Table 4.9), a multi-temperature disk emission (see model *F* in Table 4.9), a broken power-law model with a multi-temperature disk emission (see model *G* in Table 4.9) and finally, with an unabsorbed power-law with two multi-temperature disk emissions (see model *H* in Table 4.9). Comparing the results shown in the previous tables, the soft excess of this source seems to be well modelled by a broken power-law with a single black-body component, with $kT \sim 0.13$ keV in the observer-frame. Figure 4.8 shows the plot νF_ν when the spectrum is fitted by the model *G*.

Table 4.8: Best fit parameters of the models for 4C 04.42.

Model	${}^1F_{ob(2-10keV)}$	${}^1F_{ob(20-100keV)}$	${}^7\Gamma_1, \Gamma_2$	8E_b	4c	${}^5\chi_r^2/\text{dof}$	${}^6P_{null}$
<i>C</i>	0.2	1.5	$1.57_{-0.05}^{+0.04}$ $1.16_{-0.12}^{+0.08}$	$2.19_{-0.37}^{+0.62}$	0.9 ± 0.3	1.02/368	0.404
Model	${}^1F_{ob(2-10keV)}$	${}^1F_{ob(20-100keV)}$	${}^3\Gamma$	${}^9kT_{bb}$	4c	${}^5\chi_r^2/\text{dof}$	${}^6P_{null}$
<i>E</i>	0.2	1.5	1.34 ± 0.03	0.19 ± 0.05	1.4 ± 0.3	1.08/368	0.126
Model	${}^1F_{ob(2-10keV)}$	${}^1F_{ob(20-100keV)}$	${}^3\Gamma$	${}^{10}kT_{inn}$	4c	${}^5\chi_r^2/\text{dof}$	${}^6P_{null}$
<i>F</i>	0.2	1.5	1.22 ± 0.08	0.26 ± 0.05	$1.0_{-0.3}^{+0.4}$	1.05/368	0.268

¹ Observed flux in the 2 – 10 keV (and 20 – 100 keV) energy range in units of $10^{-11} \text{erg cm}^{-2} \text{s}^{-1}$. ³ Photon index, related to the spectral index α (where $F \propto \nu^{-\alpha}$) by $\alpha = \Gamma - 1$. ⁴ IBIS/MOS, BAT/MOS or IBIS/XRT cross-calibration constant. ⁵ Reduced chi-squared to degrees of freedom. ⁶ Null hypothesis probability. ⁷ Spectral index below the break (Γ_1) and above the break (Γ_2). ⁸ Observed break energy in units of keV. ⁹ Black-body temperature in the source rest-frame in units of keV. ¹⁰ Temperature at inner disk radius in the observer-frame in units of keV.

Table 4.9: Best fit parameters of the models for 3C 273.

Model	${}^1F_{ob(2-10keV)}$	${}^1F_{ob(20-100keV)}$	${}^7\Gamma_1, \Gamma_2$	8E_b	4c	${}^5\chi_r^2/\text{dof}$	${}^6P_{null}$	
<i>C</i>	7.0	17.0	1.95 ± 0.01 $1.639^{+0.005}_{-0.004}$	1.31 ± 0.03	$0.98^{+0.03}_{-0.02}$	1.24/2104	5e-13	
Model	${}^1F_{ob(2-10keV)}$	${}^1F_{ob(20-100keV)}$	${}^3\Gamma$	${}^{10}kT_{inn}$	4c	${}^5\chi_r^2/\text{dof}$	${}^6P_{null}$	
<i>F</i>	7.6	17.2	1.636 ± 0.004	$0.161^{+0.003}_{-0.004}$	$0.98^{+0.03}_{-0.02}$	1.16/2104	3e-07	
Model	${}^1F_{ob(2-10keV)}$	${}^1F_{ob(20-100keV)}$	${}^{10}kT_{inn}$	${}^7\Gamma_1, \Gamma_2$	8E_b	4c	${}^5\chi_r^2/\text{dof}$	${}^6P_{null}$
<i>G</i>	7.6	17.2	0.13 ± 0.01	$1.75^{+0.02}_{-0.01}$ 1.62 ± 0.01	$1.78^{+0.06}_{-0.03}$	0.95 ± 0.02	1.12/2102	0.0001
Model	${}^1F_{ob(2-10keV)}$	${}^1F_{ob(20-100keV)}$	${}^3\Gamma$	${}^{10}kT_{inn}$	4c	${}^5\chi_r^2/\text{dof}$	${}^6P_{null}$	
<i>H</i>	7.6	17.2	$1.616^{+0.004}_{-0.007}$	$0.27^{+0.04}_{-0.01}$ 0.13 ± 0.01	$0.93^{+0.03}_{-0.02}$	1.13/2102	3e-05	

¹ Observed flux in the 2 – 10 keV (and 20 – 100 keV) energy range in units of $10^{-11}\text{erg cm}^{-2} \text{ s}^{-1}$. ³ Photon index, related to the spectral index α (where $F \propto \nu^{-\alpha}$) by $\alpha = \Gamma - 1$. ⁴ IBIS/MOS, BAT/MOS or IBIS/XRT cross-calibration constant. ⁵ Reduced chi-squared to degrees of freedom. ⁶ Null hypothesis probability. ⁷ Spectral index below the break (Γ_1) and above the break (Γ_2). ⁸ Observed break energy in units of keV. ⁹ Black-body temperature in the source rest-frame in units of keV. ¹⁰ Temperature at inner disk radius in the observer-frame in units of keV.

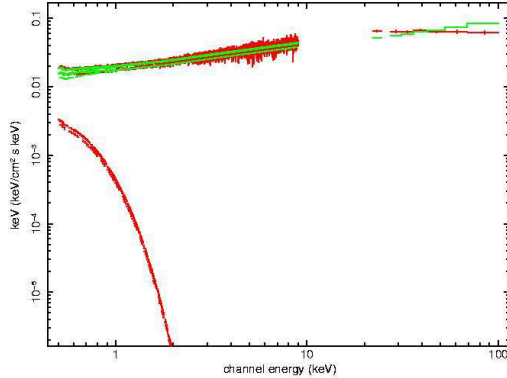


Figure 4.8: The νF_ν plot of 3C 273 obtained by fitting the spectrum with a broken power-law model and a multi-temperature disk emission.

4.7 Parameter distributions and correlations

Although the number of sources of our selected sample is not so large, we have also performed an analysis of the distribution of the spectral parameters (absorbing column density, spectral index, redshift) and their possible correlations. We note that this type of analysis has been performed so far only at energies between 0.2 – 10 keV. This study is still preliminary and has been performed by a comparison among the results of our own spectral analysis and those already available in literature performed only at the soft X-ray energies.

The majority of the sources in our sample show a deficit of soft photons in the X-ray spectrum. We emphasize that on basis of our spectral analysis an intrinsic spectral break cannot be ruled out (see the values of the reduced χ^2 and of the null hypothesis probability listed in the Tables 4.5 and 4.6). In this context, the existence of a break in the intrinsic continuum is related to the electron distribution, but important constraints on the electron distribution can be retrieved only analyzing both Synchrotron and EC components in the SED that is out of the aim of present work. Therefore we will focus the following discussion on the absorption scenario.

In the framework of a possible N_H -redshift relation as proposed in a work by Yuan et al. (2006) and based on XMM-Newton observations of a sample of RL objects, we have combined our results for the column density (depending on the redshift) with a larger sample (about thirty) of RL objects (Galbiati et al. 2005; Page et al. 2005; Yuan et al. 2006). In fact, it is interesting to check whether the 9 blazars selected in the sample and analyzed in a more wide energy band follow the trend of N_H with redshift as previously reported by Yuan et al. (2006). If this would be the case, we would have

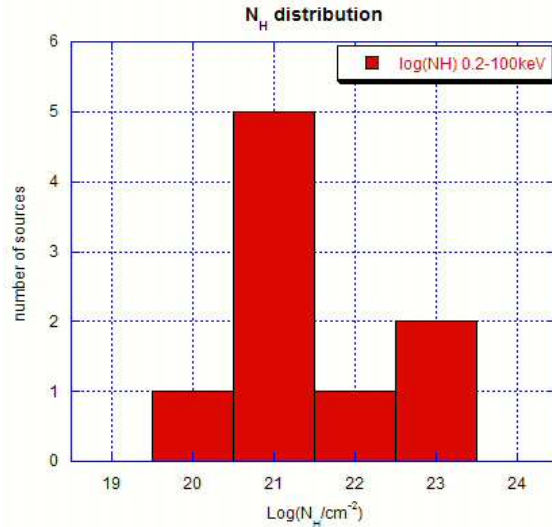


Figure 4.9: Distribution of the X-ray absorption column density (N_H) for our sample objects over the 0.2 – 100 keV energy range.

further evidence that the absorbing column density in these sources is linked to the distance and thus we would confirm a cosmic evolution effect.

4.7.1 Absorption column density distribution

We have made a detailed analysis of the rest-frame hydrogen column density (N_H) for the blazars in our sample in conjunction with the intervening absorption in excess to the galactic one.

The N_H distribution shown in Figure 4.9 appears to be asymmetric, with a peak located at about $\log(N_H) = 21$ and tails seem to extend towards low and high values until $\log(N_H) = 20$ and $\log(N_H) = 23$, respectively. However, the statistical significance of this result is strongly affected by the small number of objects in our sample. Therefore we choose to analyze N_H distribution of our sources by comparing our sample with a larger sample of 16 RL objects observed in the 0.2 – 10 keV energy range from XMM-Newton. We underline that the sample of 16 sources includes only one object belonging to our sample (the blazar QSO B0836+710). The N_H distribution of the larger sample is shown in Figure 4.10 with a peak located at $\log(N_H) = 22$ and a tail extending towards low values until $\log(N_H) = 20$. Looking at the distribution in Figure 4.10 and at the distribution in Figure 4.9, we note that sources with absorbing column density $\log(N_H) = 23$ are "missing". This evidence is expected in view of the fact that in the soft X-ray energy range 0.2 – 10 keV these sources are almost completely obscured.

On the other hand, by comparing the same N_H distributions we note that a tail towards the high values of column density ($N_H = 10^{23} \text{ cm}^{-2}$)

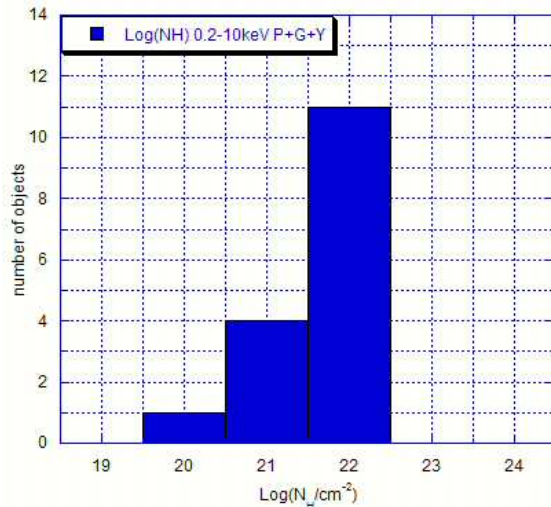


Figure 4.10: The N_H distributions of a sample of 16 RL objects observed in the 0.2 – 10 keV energy range from XMM-Newton.

is apparent. This occurrence strongly suggests that data above 10 keV represent a pivotal tool to make an unbiased selection of heavily absorbed objects.

It is clear that the statistical significance of this result is not high: it is strongly affected by the small number of objects in our sample and thus the excess of absorption is only qualitative.

With regards to the N_H -redshift trend, the N_H distribution of the sources in our sample is shown in Figure 4.11.

The comparison of the N_H distribution of our sample with those analyzed previously in the work of Yuan et al. (2006) at various redshifts based on soft X-ray observations of a sample of 32 RL sources, seems to reveal that the property of the X-ray absorption in excess to the Galactic value evolves with cosmic time. This trend is shown in Figure 4.12. In fact, at first glance, it seems that a correlation exists between N_H and redshift and, compared to low redshifts ($z < 2$), a shift toward higher values of N_H of the absorber in excess seems to be indicated at high redshifts.

We remark that the sample of 32 sources includes 3 objects belonging to our sample (QSO B0836+710, PKS 0537-286 and PKS 2149-307 with the observations Obs.ID 0112620101, 0114090101 and 0103060401, respectively) and the N_H values for these 3 sources as obtained through our spectral analysis are in agreement with those presented in the work of Yuan and collaborators (2006).

The existence of a correlation is confirmed by the statistical analysis: we obtain a correlation coefficient (R) around 0.7 (Figure 4.12) when the results corresponding to our sample are added to the sources investigated

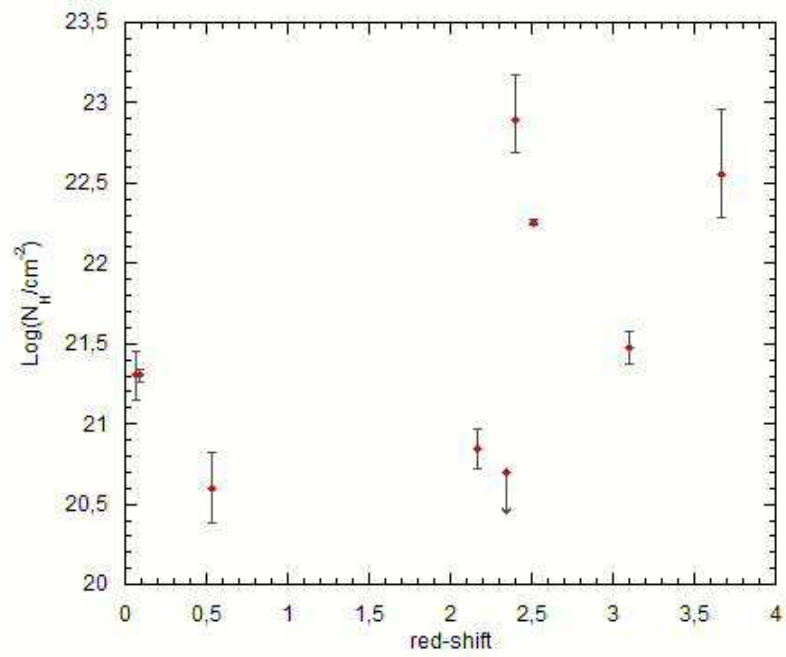


Figure 4.11: The X-ray absorption column density N_H as a function of the redshift for our sample.

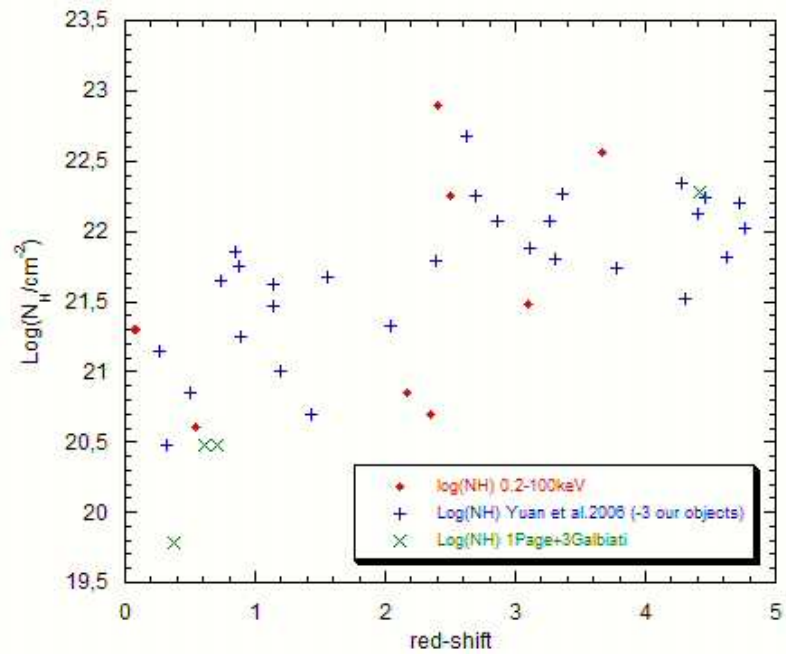


Figure 4.12: The X-ray absorption column density N_H as a function of the redshift, combining the results of our sources (empty red rhombs) and ones of a larger sample (blue plus and green cross signs) analyzed in the soft X-ray energy range.

in the works by Page et al. (2005), Galbiati et al. (2005) and Yuan et al. (2006).

This result seems to support the hypothesis of an intrinsic absorber. It should be noted that the investigation of the possible correlations between the various parameters - such as N_H versus redshift - is mandatory in order to find an explanation of the nature of this absorption. We mention two hints supporting the intrinsic nature of the hydrogen column density in the following:

- the X-ray absorption is associated with RL but not with RQ objects (Yuan & Brinkmann, 1999). This evidence supports the hypothesis that the absorber are physically associated with the RL quasars;
- the change of the N_H distribution that seems to occur at $z \sim 2$ and the decrease of the slope in the N_H - z relation at $z > 2$ could indicate an effect of cosmic evolution. This effect could be due e.g. to the rate of stellar formation. In fact, an increase of the stellar formation at $z \leq 2$ could reduce the amount of gas in the host galaxy.

4.7.2 Photon-index distribution

The distribution of the photon index (Γ) for our sample as obtained by taking into account both the excess of X-ray absorption and the excess of emission, when present, is shown in Figure 4.13. The mean value obtained from our analysis in 0.2 – 100 keV energy band is $\Gamma = 1.39 \pm 0.01$.

This value is flatter than the value found by Page et al. (2005) derived from an analysis of a sample of 16 radio-loud objects in the soft 0.3 – 10 keV energy band and having redshifts in the range $2.0 < z < 4.7$ ($\Gamma = 1.55 \pm 0.04$).

For comparison, in Figure 4.14 we also show the distribution of the photon index derived from the analysis performed in the works of Page et al. (2005), Galbiati et al. (2005) and Yuan et al. (2006) and including 35 sources. The Γ distribution of our sample of sources shows a peak at $\Gamma \sim 1.4$, whereas the Γ distribution of the RL objects as obtained by including the results published by Page et al. (2005), Galbiati et al. (2005) and Yuan et al. (2006), shows a peak corresponding to a steeper value of Γ (~ 2). However, we note here that our sample is mainly composed by FSRQ, while the larger sample contains different types of RL objects - not all identified as Blazars. Therefore, in order to perform a more meaningful comparison, we have studied the photon index distribution only for the sources – in the larger sample – identified as Blazars (19 objects). The location of the peak of the Γ distribution (see Figure 4.15) is again around 2.

In order to account for the fact that the majority of the sources in our sample are FSRQ-type objects and that FSRQ objects show a lower value of Γ with respect to BL Lac objects, we studied the Γ distribution by including

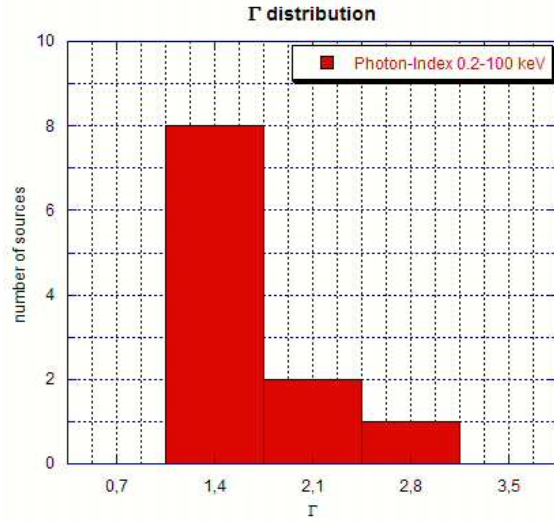


Figure 4.13: Distribution of the power-law photon-index for our sample in the 0.2 – 100 keV energy range.

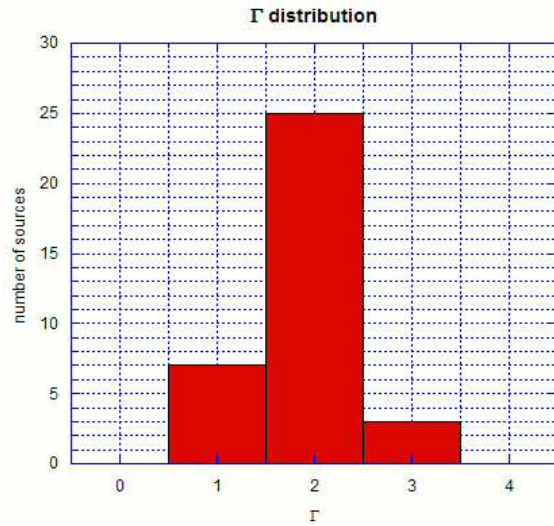


Figure 4.14: Distribution of the photon-index resulting by the analysis performed in the works of Page et al. (2005), Galbiati et al. (2005) and Yuan et al. (2006).

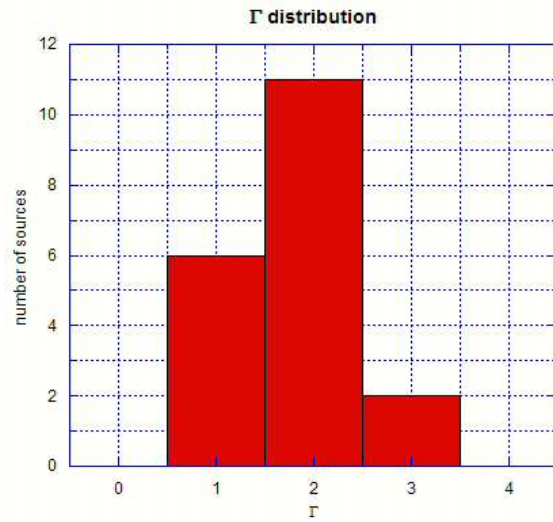


Figure 4.15: Photon-index distribution for the sources of the larger sample identified as Blazar.

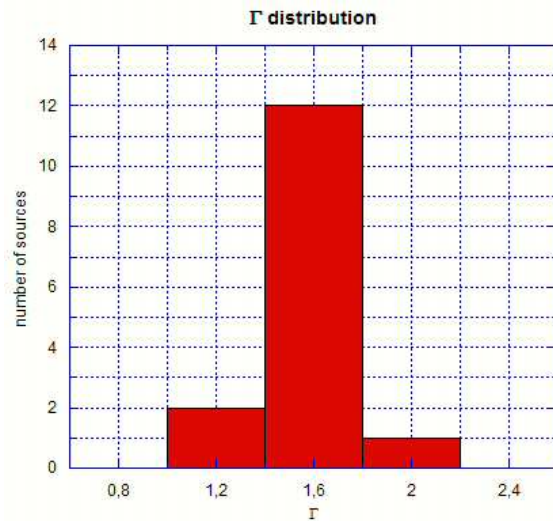


Figure 4.16: Photon-index distribution for the sources of the larger sample identified as FSRQ.

only the FSRQ sources in the larger sample (15 objects). In this case, the Γ distribution in Figure 4.16 shows a peak at $\Gamma \sim 1.6$. This value of the photon index is again steeper than that for our Blazar sample.

The differences between the values of Γ of our sample and those of the larger sample could be due to the hard X-ray selection of our INTEGRAL sample, which is clearly biased towards the flatter values of the photon index.

Chapter 5

Discussion

5.1 Introduction

We have studied the broad-band behavior of the whole sample of blazars detected by INTEGRAL satellite, by investigating the spectral characteristic: the continuum shape, the Compton reflection components, the absorption and emission features. This analysis has allowed us to highlight several still-open questions.

At first we will focus our discussion on the flattening/steepening of the spectrum of our sample in the soft X-ray energy range and on their possible physical interpretations. In the following sections we will discuss the presence of the Reflection features and the possible evidence of a variability in the spectra of our sources. In the final section the discussion will be mainly focused on the absorption and on the broad-band continuum shape of our INTEGRAL Blazars sample.

5.2 Absorption properties

The broad-band spectral analysis has shown that a deficit of photons in the soft X-ray energy domain is a common feature of 9/11 objects of our sample. This phenomenon has been previously observed in several samples of RL objects (e.g. Page et al. 2005, Galbiati et al. 2005, Yuan et al. 2006) and its origin is not yet well understood. This observed soft X-ray flattening can be produced by either an intrinsically curved continuum or an extra absorption component (this is the gas present in our Galaxy $-N_H^{Gal}-$ does not contribute to the global absorption).

The broken continuum hypothesis is linked to the blazar-type source. In fact, in the hypothesis of an intrinsically curved blazar continuum, it can be assumed that the relativistic electrons in the jet follow a broken power-law energy distribution with a low energy cut-off, producing a flattening in the observed spectrum. This is a purely phenomenological form and it has

been assumed to reproduce the observed shape of the blazar SEDs, without any specific assumption on the acceleration/cooling mechanism acting on the particles (e.g. Tavecchio et al. 2007). Alternatively, within the same hypothesis, it can be also assumed that there is an inefficient radiative cooling of lower energy electrons of the jet producing few Synchrotron photons. These photons, which are scattered at higher energies via SSC mechanism, poorly contribute to filling of the "gap" between the Synchrotron and External Compton components, primarily in the UV-soft X-ray band and produce the observed spectral break (e.g. Sikora, Begelman & Rees 1994).

As discussed in the previous Chapter, the presence of a break in the intrinsic continuum can not be exploited on the basis of present analysis, then in the following we will discuss in detail the scenario related to the presence of an absorber.

The explanation with an absorption takes into account an absorber in excess of the Galactic one.

In general, in an AGN, the absorption observed in the X-ray band is due to the presence of gas that absorbs via photoelectric effect, and it appears as a suppression of the emission in the soft-X band with an energy cut-off. This energy cut-off increases with increasing column density of Hydrogen (N_H) of the absorber. It is worthwhile to note that to investigate how the absorption affects the spectrum of the object, can provide relevant data on the geometry and distribution of the absorber.

In some cases, the absorbing medium can be cold (not ionized) and located between the observer and the source along the line of sight at a different redshift with respect to the blazar (e.g. Cappi et al. 1997; Fiore et al. 1998; Fabian et al. 2001; Masetti et al. 2004). In other cases, the cold absorbing medium can be located at the same redshift of the source (Page et al. 2005; Yuan et al. 2006) in the circum-nuclear region, as suggested by the observed variability in Risaliti et al. 2005, 2007 – see following discussion on this issue – and it is namely an intrinsic cold absorber.

In the case of an absorber located between the observer and the source at several redshifts, the damped Ly-alpha systems are the more plausible cause (e.g. Elvis et al. 1994) and the line of sight would have to pass through two or more very high column density damped Ly-alpha systems (e.g. Fall & Pei 1995). However this is a rare occurrence (e.g. O’Flaherty & Jakobsen 1997; Zwaan, Verheijen & Briggs 1999) and favors the hypothesis that, if the origin of the soft X-ray flattening is a cold absorber, it is intrinsic to the source with column densities of the order $10^{22} - 10^{23} \text{ cm}^{-2}$. The suggestion of an intrinsic origin is also confirmed by the circumstance that the soft X-ray spectral flattening has so far been detected only in objects that are radio loud (Bechtold et al. 1994; Reimers et al. 1995; Siebert et al. 1996).

In this case, it is possible to obtain further information by comparing optical/UV data and X-ray data. In fact, we know that the obscuration due to the presence of dust (Polletta et al. 2007) is usually observed at

optical and IR wave-lengths where the continuum and the emission lines are reddened and, sometimes, completely suppressed.

It can be the case that the AGN, absorbed in the X-ray band, are not obscured in the optical-IR band, and viceversa. So, if the AGN absorbed in the X-ray band, does not show significantly reddened/obscured optical spectra, this means that the absorbing medium is located within the central engine. In fact, the dust sublimation is possible only if it is near to the black hole.

If it is present absorption in the optical/IR band, but not in the X-ray band, this occurrence is considered an evidence that the gas is fully ionized and so completely transparent to the X photons (Fabian et al. 2001).

It is also possible to assume that the absorbing intrinsic matter is warm. In this case, the absorbing medium, at the same redshift of the AGN (probably, the inner part of the dense interstellar medium of the young host galaxy), is ionized possibly due to the proximity from the jet (Fabian et al. 2001; Yuan et al. 2006).

In the case of our selected sample, the fitting procedure supports the presence of an intrinsic (local to the AGN) cold absorber for all sources showing deficit of low-energies photons. The possibility of a warm absorber (absori in XSPEC) can be excluded since the model with an ionized-gas produces a worse fit and an inconsistent value for the ionization parameter ($\xi \sim 0 \text{ erg cm s}^{-1}$ and $\xi > 500 \text{ erg cm s}^{-1}$; these values of the ionization parameter indicate a neutral absorber and a completely ionized absorber, respectively).

In the case of an intrinsic absorber, the information on the absorption is of pivotal importance to understand the blazar environment and its interaction with the jet.

The absorption originating from the material present in the AGN environment – possibly in the form of clouds near the central source (Cappi et al. 1997) – seems to be the more plausible explanation for many sources belonging to the class of RL AGN (Page et al. 2005; Yuan et al. 2006, and references therein). There is some evidence not only of absorption but also of a correlation between absorption and redshift, with the more distant sources being more absorbed and the increase in N_H with z occurring starting at $z \sim 2$ (Yuan et al. 2006). We note that more than one half of sources in our sample appears in agreement with this scenario, because this fraction of objects has a redshift larger than 2. Moreover, if the mentioned N_H - z trend is real, the observational band above 10 keV of INTEGRAL/IBIS instrument is of pivotal importance, because it allows the detection of more strongly absorbed objects. Therefore more highly absorbed high- z objects will be detected by this instrument in the near future.

However, so far, the physical interpretation of absorption has not been confirmed. The issues about the absorption in RL objects presented in this work, in combination with the results of previous analysis (Page et al.

2005) can be put in a more general context: the origin of the observed X-ray spectral differences between RL and RQ AGNs. The excess of intrinsic absorption in the rest-frame of the RL objects compared with the lack of any absorption above the Galactic value of their RQ counterparts (Canizares & White 1989; Lawson & Turner 1997; Yuan et al. 1998; Page et al. 2003, 2005; Vignali et al. 2003, 2005; Grupe et al. 2006), suggests that an intrinsic difference could exist in the local environments of the two classes of objects. Since the X-ray spectra of RL AGNs appear to be dominated by the emission of the jet component, it is likely that the absorbing material is linked to the presence of this component. This working scenario is supported by a theory discussed, e.g., in the work of Ferrari (1998), in which the confinement of the radio jet needs the presence of a cold medium (local to the AGN) able to contrast the jet expansion.

5.3 Emission properties

The spectral behavior of 4C 04.42 and 3C 273 deviates from that of the other sources in the sample since they show a soft X-ray emission component (see Figure 4.3). Several competing models to fit this component are available: a broken power-law continuum, a multi-temperature black-body or a disk reflection.

The observed steepening can be due to an intrinsic energy break of the electron population, belonging probably to the jet, that up-scatters the photons coming from the disk through Inverse Compton, so producing an intrinsically curved continuum in the photon distribution (e.g. Ghisellini et al. 1998, Maraschi et al. 2008). The quoted break in the energy distribution of the electrons can be produced by their radiative losses: increasing the energy of the electron, the probability that this electron loses energy via different mechanisms – mainly via synchrotron process – increases. As a consequence, the number of electrons at low energy is quite larger with respect the number of high energy electrons, and so the number of target photons scattered at high energy decreases with respect to those scattered at low energy. This occurrence will produce a break in the resulting photon distribution. An alternative interpretation of this soft X-ray component within the same scenario – the intrinsic break energy in the electrons population – is based on mechanisms (e.g. shocks due to the collision of plasma shells propagating with different Lorentz factors within the jets or magnetic reconnections) that energize/accelerate the relativistic electrons at the low energies (that is with $\gamma < 10$), involved in production of the X-ray emission within the EC model (e.g. Kataoka et al. 2008).

Alternatively, the observational feature can be associated to the existence of a population of cold electrons (Begelman & Sikora 1987), that is with a Lorentz factor $\gamma \approx 1$, present in the jet. Also these electrons, like the

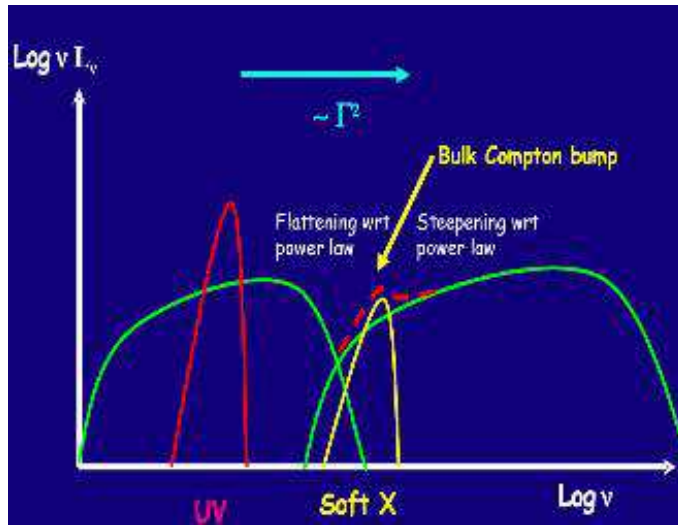


Figure 5.1: Bulk Compton feature (Celotti, Ghisellini & Fabian 2007)

relativistic ones, interact via IC process with the photons coming from the accretion disk and reprocessed by the BLR. Since the γ factor is very small, the energy acquired by the photons is small so they ‘shift’ from the typical energies of the UV – where is located the disk bump – to the soft X-ray band energies, producing the observed feature in the soft X-ray energy range of the spectrum (see Figure 5.1).

The quoted process is named Bulk Compton (BC) and it is one of the most recent interpretations suggested for the soft X-ray band emission (Kataoka et al. 2008, Celotti, Ghisellini & Fabian 2007). The ratio between the luminosity associated to the Bulk Compton process and that associated to the IC, clearly depends on the population ratio between the cold electrons and the relativistic ones. The possibility to retrieve this information on the presence, if any, of the cold electron population is quite important since this is the unique opportunity we have for tracing this population of electrons. In fact, these electrons would make synchrotron in the regime of absorption and so not observable. In addition, they would also provide a remarkably negligible contribution to the EC. The study of the Bulk Compton is also relevant for obtaining important estimates of the bulk Lorentz factor and the kinetic energy associated to the cold electron of the jet (Celotti, Ghisellini & Fabian 2007). The evaluation of this minimum energy is very important to evaluate the total power transported by the jets and, to provide strong constraints on the physical mechanisms contributing to accelerate the relativistic electrons. It is worth noting that to observe the Bulk Compton component is quite difficult, mainly for three reasons:

- in general it can be a transient feature if the plasma (e^- , e^+ e p) of

injection and dissipation in the jet is not continuous; this occurrence is also supported by the evidence of a strong variability in the whole electromagnetic spectrum observed in the blazars;

- the radiation has to be strongly beamed. In other words, the jet has to be highly relativistic and the angle with the line of sight has to be small;
- the other emission processes could obscure this component; in fact the Bulk Compton is often embedded in the SSC component.

Finally, another possibility is that the soft X-rays emission results from reprocessing of the hard X-ray power-law, for instance through reflection and scattering of X-rays off the optically thick disc (e.g. George & Fabian 1991). The presence of a disk emission including the Reflection Component has been suggested by Sambruna and collaborators 2006 for the blazars 1136-135, 1150-497, 0723-679.

Alternative interpretations of this spectral feature have been provided so far and it will be briefly addressed in the following: the possible contribution of the SSC in the soft X-ray band, the presence of a soft-excess as that observed in the RQ AGN, the fact that the synchrotron emission is peaked in the X-ray band and not in the IR (the so-called Blue Quasars) and, quite recently, Tavecchio & Ghisellini (2008) have suggested that the observed emission could be properly interpreted by adopting a realistic emission spectrum for the BLR to derive the EC component.

5.3.1 The case of 4C 04.42

4C 04.42 is a FSRQ at $z = 0.965$ that shows a soft X-rays excess component, with the low-energy spectrum steeper ($\Gamma \sim 1.6$) than the high-energy power-law ($\Gamma \sim 1.2$) and a break in energy at around 2 keV in the observer frame. We note that although the multi temperature disk emission model seems to fit well the observed spectrum with kT of the inner disk around 0.5 keV in the quasar frame (see Table 4.8), it appears not realistic. In fact, a so high temperature strongly suggest that the emission can not be due to result directly from the quasar accretion disk; as on the contrary it occurs in the RQ quasars, for which lower disk temperatures¹ are obtained.

A temperature around 0.2 keV is certainly more consistent with emission from the disk for such objects. The origin of this soft X-rays excess emission component observed in 4C 04.42 has been already investigated by De Rosa et al. 2008. It is likely due to bulk Compton of a ‘cold’ relativistic shell of plasma moving in the jet of the blazar and interacting with the external photon field originated from the accretion disk and reprocessed in the Broad

¹The temperature of the disk component varies as $T_{BB} \sim M_{BH}^{-1/4}$ and hence is expected to be cooler for the more luminous objects with larger black hole masses.

Line Region (BLR). In fact, it is plausible that the bulk Comptonization by these cold electrons could up-scatter cooler extreme ultraviolet (EUV) photons from the disk to soft X-ray energies and account for the observed emission (Celotti, Ghisellini & Fabian 2007). We note that a similar feature at the energy of the soft X-rays (energies lower than 3 keV in the observer-frame) has been detected so far in the SED of few additional sources: the RL quasars 1136-135, 1150+497 observed with CHANDRA, 0723+679 observed with XMM-Newton (Sambruna et al. 2006) e PKS 1510-089 (Kataoka et al. 2008) observed with Suzaku. However, besides to the models that include a thermal emission of black-body, also a broken power-law well models the observed spectrum with an energy break of $E_b = 2.2^{+0.6}_{-0.4} \text{ keV}$.

5.3.2 The case of 3C 273

The second source of the sample that shows a spectral steepening at low energies is the FSRQ 3C 273. We note that in this case, contrary to the 4C 04.42, a simple broken power-law model does not provide a good fit (see the value of P_{null} in Table 4.9). We obtain a improvement in the fit with the models that include a thermal emission from multiple black-bodies (models *F*, *G* and *H*). But among these, the modelling of the soft excess with two emissions from black-body is not quite physical and although it produces an acceptable fit (Table 4.9) we exclude it. More realistic models for the emission are likely the *F* and *G* ones. Between these, the broken power-law model with a single thermal emission from black-body (model *G*) seems to fit lightly better (compare the values of χ_r^2 and P_{null}). It gives a temperature at inner disk radius $kT \sim 0.13 \text{ keV}$ in the observer-frame, that is a temperature of around 0.15 keV in the source rest-frame. This value is consistent with a thermal emission resulting directly from the quasar accretion disk. The observed break energy around 1.8 keV could be attributed to one out of two physical interpretations discussed above about the intrinsically curved continuum.

Our broad-band results are consistent with the ones obtained by analysis of XMM-Newton observations by Page et al. 2003 on the same revolution of 17 June 2000 (number 96). More in detail, in their analysis, the soft X-ray emission component is well fitted with multiple black-body components with $kT \sim 0.1$ and 0.2 keV in the observer frame. For this source a broad-band analysis with XMM-Newton and INTEGRAL data has been already published by Chernyakova and collaborators, 2007. The low energy data have been obtained by observations in the years 2003, 2004 and 2005. The results of their study show that the $0.2 - 100 \text{ keV}$ spectrum of 3C 273 is well fitted by a combination of a soft cut-off power-law ($\Gamma \sim 2.3$) and a hard power-law ($\Gamma \sim 1.7$) with a energy break around to 1 keV .

5.4 Compton Reflection features and the analysis of the variability

In our sample we have not found neither an evidence of an iron emission line nor evidence of a Compton reflection "hump". The lack of these spectral features – interpreted as the result of reprocessing of the primary continuum by cold matter around the X-ray source, presumably the accretion disk (Lightman & White 1988; Guilbert & Rees 1988; George & Fabian 1991; Sambruna & Eracleous 1999; Sambruna, Eracleous & Mushotzky 1999) – can be explained either with the out-and-out absence of these reprocessing features in Blazar-type objects or with the hypothesis that these features in strong radio sources are difficult to detect being likely dilute by the jet (Sambruna et al. 2006).

In view of the fact that we analyze non-simultaneous broad-band data of highly variable sources, it is important to understand the effects of the variability on the detection of the Compton Reflection hump. In fact, this hump above 10 keV can be reproduced by a cross-correlation constant greater than unity. This can be the case for QSO B0836+710, 1ES 0033+595, PKS 2149-307, IGR J22517+2218, BL Lac, and 3C 279 (see Tables 4.5 and 4.6). However we stress that the spectral shape (Γ) does not change between 0.2 – 10 keV and 20 – 100 keV energy ranges, supporting the idea that, above 10 keV, no additional component to the power-law (e.g. Reflection hump) is present in the spectrum.

Therefore, we can attribute the changes in the intensity between high energies instruments and low energies ones to the strong time variability of these Blazar-type objects. In particular, we found that the source IGR J22517+2218 did undergo severe changes in the intensity between the INTEGRAL and the Swift observations with a value of the XRT/IBIS intercalibration factor of about 7 (see Table 4.5). In addition, we wish to remark that the data of the Third INTEGRAL survey correspond to an average performed on observations spanning a temporal interval of about 3 years, while the data for the low-energy range correspond to observations with a time baseline of few hours.

5.5 Conclusions

In this work we have presented a systematic broad-band X-rays spectral study of a sample of 11 blazars (with a redshift range of $0.06 < z < 3.67$) observed with INTEGRAL, XMM-Newton and Swift. We remark once more that the selected objects are representative of INTEGRAL blazars. The main results of the present analysis can be summarized as follows:

- The broad-band spectra of all selected sources - but two, the FSRQs 4C 04.42 and 3C 273 - are well reproduced with a power-law model

absorbed by an amount of gas in excess to the Galactic one ($N_H \sim 10^{20} - 10^{23} \text{ cm}^{-2}$; we note that for the source FSRQ PKS 2149-306 only an upper limit of $N_H \sim 2 \cdot 10^{20} \text{ cm}^{-2}$ has been derived).

- The previously quoted result provides plain evidence to the fact that by using the INTEGRAL high-energies data the highly absorbed sources can be more easily detected.
- The absorption seems to be a signature of a cold intrinsic absorber, confirming and extending previous results quoted in the literature (Cappi et al 1997, Page et al. 2005, Yuan et al 2006).
- Present work provides a further confirmation of the existence of a N_H -redshift trend.
- The broad-band analysis of our sample of blazars revealed a harder spectrum with a photon-index of the order of $\Gamma \sim 1.4$, with respect to the mean value of the spectral index obtained by Page et al. (2005) with XMM data of a statistically sizeable sample of RL objects. Such a difference could be due to the hard X-ray selection of our INTEGRAL sample that is clearly biased towards flatter values of the photon index as shown by previous results.
- Previous result clearly shows that the INTEGRAL high energies data allow to observe the sources with a flat spectrum.
- In our analysis we have find two case of soft-excess, 4C 04.42 and 3C 273. The case of 4C 04.42 has been interpreted as Bulk Compton emission produced by cold plasma accelerating in the blazar jet (De Rosa et al. 2008).
- We have not found any evidence of reflection components (Reflection "hump" and iron emission line) as expected in RL-type objects.
- We note that, due to the small size of the sample, our results could be affected by statistically effects.

In conclusion, the analysis presented here has shown that our INTEGRAL-sample selection favours objects heavily absorbed and with a flatter value of spectral index. On the other hand, the present broad-band analysis of INTEGRAL, XMM-Newton and Swift observations of RL QSOs confirms that the observed flattening, interpretable as absorption in excess to the Galactic one, is common in these objects and is clearly detected in 8 out of 11 quasars of our sample. The assumption, confirmed by fitting procedure, of an intrinsic origin and a cold nature for the absorber is in agreement with previous results up to 10 keV obtained by Page et al. (2005) and Yuan et al. (2006) with XMM-Newton data only. However, a broken power-law

model, as alternative explanation for the deficit of soft photons observed in the majority of our sources, cannot be ruled out by the data. We stress that, despite the poor statistical quality due to the small sample, our results have been obtained by a broad-band study and thus by a more complete analysis with respect to the analysis obtained only with observations at low energies.

5.6 Future developments

The future work that we plan to perform can be summarized as follows:

- We point out that in order to verify the intrinsic nature of the absorber, we will need to support the following issues:
 - the optical extinction observed in these sources should be not consistent with the high density of N_H required in order to reproduce the observed soft X-ray flattening;
 - no correlation should exist between the absorption and the occurrence of any damped Ly-alpha system along the line of sight, suggesting that the absorbers are associated with the QSO or its host galaxy.
- It will be important to observe many more blazar objects with INTEGRAL to determine how common the spectral flattening observed in our sample is and whether the phenomenon can be correlated with any other properties of the objects (redshift, etc). This will help to determine whether the spectral flattening is indeed an intrinsic property of the source (and if so provide clues as to its origin). To this aim we expect to achieve key results with significantly increase of the data set making use of the public data now available from INTEGRAL observations (included in the Fourth INTEGRAL/IBIS catalog).
- We will work on building the SED of the Blazars of our sample by collecting data from radio up to gamma-rays (through public Fermi/LAT data).
- By comparing our SEDs with theoretical ones already published we want to check if these models properly reproduced the hard X-ray data. This is fundamental in order to estimate the physical parameters of the emitting region (bulk Lorentz factor, n_e , γ_m , γ_M , etc.) and so to investigate more in detail the emission processes of type-Blazar objects.
- The possibility of doubling the number of sources of our sample by using the new public INTEGRAL data (Bird et al. 2009) will allow us to achieve more sound results about the physical processes governing the blazar SED, and to perform a more significant statistical analysis.

Bibliography

- Abdo A.A., Ackermann M., Ajello M. et al., 2009, *ApJ*, 700, 597
- Antonucci R.R.J. & Miller J.S., 1985, *ApJ*, 297, 621
- Antonucci R., 1993, *ARA&A*, 31, 473
- Arnaud K., 1996, in *ASP Conf. Ser. 101, Astronomical Data Analysis Software and Systems V*, ed. G. Jacoby & J. Barnes (San Francisco: ASP), 17
- Baade W. & Minkowski R., 1954, *ApJ*, 119, 215
- Ballantyne D.R., Ross R.R. & Fabian A.C., 2002, *MNRAS*, 332, L45
- Bassani L., Landi R., Malizia A. et al., 2007, *ApJ*, 669, L1
- Bechtold J., Elvis M., Fiore F. et al., 1994, *AJ*, 108, 759
- Bennert N., Falcke H., Schulz H. et al., 2002, *ApJ*, 574, 105
- Bird A.J., Malizia A., Bazzano A. et al., 2007, *ApJ*, 170, 175
- Bird A.J., Bazzano A., Bassani L., Capitanio F. et al., 2009, *arXiv* : 0910.1704
- Brinkmann W., Laurent-Muehleisen S.A., Voges W. et al., 2000, *A&A*, 356, 445
- Canizares C.R. & White J.L., 1989, *ApJ*, 339, 27
- Cappi M., Matsuoka M., Comastri A. et al., 1997, *ApJ*, 478, 492
- Celotti A., Ghisellini G. & Fabian A.C., 2007, *MNRAS*, 375, 417
- Chernyakova M., Neronov A., Courvoisier T.J.-L. et al., 2007, *A&A*, 465, 147
- Cohen M.H., Ogle P.M., Tran H.D. et al., 1999, *AJ*, 118, 1963
- De Rosa A., Piro L., Tramacere A. et al., 2005, *A&A*, 438, 121
- De Rosa A., Bassani L., Ubertini P. et al., 2008, *MNRAS*, 388, 54
- Dermer C.D. & Schlickeiser R., 1993, *ApJ*, 416, 458
- Donato D., Ghisellini G., Tagliaferri G. et al., 2001, *A&A*, 375, 739
- Dunlop J.S., McLure R.J., Kukula M.J. et al., 2003, *MNRAS*, 340, 1095

Elvis M., Fiore F., Mathur S. & Wilkes B., 1994, *ApJ*, 425, 103

Eracleous M., Sambruna R. & Mushotzky R.F., 2000, *ApJ*, 537, 654

Fabian A.C., 1979, *RSPSA*, 366, 449

Fabian A.C., Rees M.J., Stella L. & White N.E., 1989, *MNRAS*, 238, 729

Fabian A.C., Celotti A., Iwasawa K. & Ghisellini G., 2001, *MNRAS*, 324, 628

Fall S.M. & Pei Y.C., 1995, *Proceedings of the ESO Workshop Held at Garching, Germany, 21-24 November 1994*, edited by G. Meylan. Springer-Verlag Berlin Heidelberg New York. Also *ESO Astrophysics Symposia*, p.23

Ferrari A., 1998, *A&A*, 36, 539

Fiore F., Giommi P., La Franca F. et al., 1998, *arXiv:astro-ph/9911149*

Fossati G., Maraschi L., Celotti A. et al., 1998, *MNRAS*, 299, 433

Galbiati E., Caccianiga A., Maccacaro T. et al., 2005, *A&A*, 430, 927

George I.M. & Fabian A.C., 1991, *MNRAS*, 249, 352

Ghisellini G., Celotti A., Fossati G. et al., 1998, *MNRAS*, 301, 451

Ghisellini G. & Tavecchio F., 2008, *MNRAS*, 387, 1669

Ghisellini G. & Tavecchio F., 2009, *MNRAS*, 397, 985

Giuliani A., D'Ammando F., Vercellone S. et al., 2009, *A&A*, 494, 509

Goldwurm A. et al., 2003, *A&A*, 411, 223

Grandi P., Maraschi L., Urry C.M. & Matt G., 2001, *ApJ*, 556, 35

Grandi P. & Palumbo G.C., 2004, *Science*, 306, 998

Grandi P., Malaguti G. & Fiocchi M., 2006, *ApJ*, 642, 113

Grupe D., Mathur S., Wilkes B. & Osmer P., 2006, *AJ*, 131, 55

Guilbert P.W. & Rees M.J., 1988, *MNRAS*, 233, 475

Haardt F. & Maraschi L., 1993, *ApJ*, 413, 507

Haardt F., Maraschi L. & Ghisellini G., 1994, *ApJ*, 432, 95

Hartmann R.C. et al., 2001, *ApJ*, 553, 683

Hoyle F. & Fowler W.A., 1963, *MNRAS*, 125, 169

Kaspi S., Maoz D., Netzer H. et al., 2005, *ApJ*, 629, 61

Kataoka J., Madejski G., Sikora M. et al., 2008, *ApJ*, 672, 787

Kellermann K.I., Sramek R., Schmidt M. et al., 1989, *AJ*, 98, 1195

Kirsch M.G.F., Becker W., Larsson S. et al., 2004, ESASP, 552, 863
Kirsch M.G.F., Briel U.G., Burrows D. et al., 2005, SPIE, 5898, 22
Kormendy J. & Gebhardt K., 2001, AIPC, 586, 363
Laor A., 2003, ApJ, 590, 86
Lawson A.J. & Turner M.J.L., 1997, MNRAS, 288, 920
Lebrun F., Leray J.P., Lavocat P. et al., 2003, A&A, 411, 141
Lightman A.P. & White T.R. 1988, ApJ, 335, 57
Lumsden S.L., Heisler C.A., Bailey J.A. et al., 2001, MNRAS, 327, 459
Lund N. et al., 2003, A&A 411, L231
MacLeod J.M. & Andrew B.H., 1968, ApL, 1, 243
Magdziarz P. & Zdziarski A.A. 1995, MNRAS, 273, 837
Mannheim K. & Biermann P.L., 1992, A&A, 253, 21
Maraschi L., Ghisellini G. and Celotti A., 1992, ApJ, 397, L5
Maraschi L., Foschini L., Ghisellini G. et al., 2008, MNRAS, 391, 1981
Maraschi L. & Tavecchio F., 2003, ApJ, 593, 667
Mas-Hesse J.M. et al., 2003, A&A 411, L261
Masetti N., Palazzi E., Bassani L. et al., 2004, A&A, 426, 41
Masetti N., Mason E., Morelli L. et al., 2008, A&A, 482, 113
Matt G., 2001, AIPC, 599, 209
Mushotzky R.F., Done C., Pounds K.A. 1993, ARA&A 31, 717
O'Flaherty K.S. & Jakobsen P., 1997, ApJ, 479, 673
Padovani P., 1997, MmSAI, 68, 47
Page K.L., Turner M.J.L., Reeves J.N. et al., 2003, MNRAS, 338, 1004
Page K.L., Reeves J.N., O'Brien P.T. & Turner M.J.L., 2005, MNRAS, 364, 195
Peterson B.M., 1993, PASP, 105, 247
Pittori C., Verrecchia F., Chen A.W. et al., 2009, A&A 506, 1563
Polletta M., Bassani L., Malaguti G. et al., 1996, ApJS, 106, 399
Polletta M., Farrah D., Hoenig S. et al., 2007, Spitzer Proposal, ID.40398
Rees M.J., 1984, ARA&A, 22, 471

Rees M.J., 1966, *Nature*, 211, 468

Reimers D., Bade N., Schartel N. et al., 1995, *A&A*, 296, 49

Richstone D.O., 2002, *RvMA*, 15, 57

Risaliti G., Elvis M., Fabbiano G. et al., 2005, *astro-ph*, 3351

Risaliti G., Elvis M., Fabbiano G. et al., 2007, *ApJ*, 659, 111

Rudy R.J., Cohen R.D., Ake T.B., 1988, *ApJ*, 332, 172

Rybicki & Lightman, 1979, "Radiative processes in Astrophysics", Wiley publication

Sambruna R.M. & Eracleous M., 1999, *arXiv:astro-ph/9911503*

Sambruna R.M., Eracleous M. & Mushotzky R.F., 1999, *ApJ*, 526, 60

Sambruna R.M., Gliozzi M., Tavecchio F. et al., 2006, *ApJ*, 652, 146

Sambruna, R.M., Markwardt C.B., Mushotzky R.F. et al. 2006, *ApJ*, 646, 23

Schmidt M., 1963, *Nature*, 197, 1040

Schmidt J.L., 1968, *Nature*, 218, 663

Schmitt H.R. & Kinney A.L., 1995, *AAS*, 187, 5006

Schödel R., Ott T., Genzel R. et al., 2002, *Nature*, 419,694

Shakura N.I., 1973, *SvA*, 16, 756

Siebert J., Brinkmann W., Morganti R. et al., 1996, *MNRAS*, 279, 1331

Sikora M., Begelman M.C. & Rees M.J., 1994, *ApJ*, 421, 153

Stickel M., Padovani P., Urry C.M., Fried J.W., & Kuhr H., 1991, *ApJ*, 374, 431

Tavani M. et al. 2008, *Nucl. Instrum. Methods Phys. Res. A*, 588, 52

Tavecchio F., Maraschi L., Ghisellini G. et al., 2007, *ApJ*, 665, 980

Tueller J., Mushotzky R.F., Barthelmy S. et al., 2008, *ApJ*, 681, 113

Tueller J., Baumgartner W.H., Markwardt C.B. et al., 2009, *arXiv0903.3037*

Ubertini P., Lebrun F., Di Cocco G. et al., 2003, *A&A*, 411, 131

Urry M.C. & Padovani P., 1995, *PASP*, 107, 803

Vedrenne G., Roques J.-P., Schonfelder V. et al., 2003, *A&A* 411, 63

Vignali C., Brandt W.N., Schneider D.P. et al., 2003, *AJ*, 125, 2876

Vignali C., Brandt W.N., Schneider D.P. and Kaspi S., 2005, *AJ*, 129, 2519

- Visvanathan N., 1969, ApJ, 155, 133
- White R.L., Becker R.H., Gregg M.D. et al., 2000, ApJS, 126, 133
- Winkler C., Courvoisier T.J.-L., Di Cocco G. et al., 2003, A&A 411, L1
- Worrall D.M., Tananbaum H., Giommi P. et al., 1987, ApJ, 313, 596
- Yuan W., Brinkmann W., Siebert J. & Voges W., 1998, A&A, 330, 108
- Yuan W. & Brinkmann W., 1999, Proceedings of the Symposium "Highlights in X-ray Astronomy", eds. B. Aschenbach & M.J. Freyberg, MPE Report 272, 240
- Yuan W., Fabian A.C., Worsley M.A. & McMahon R.G., 2006, MNRAS, 368, 985
- Zamorani G., Henry J.P., Maccacaro T. et al., 1981, ApJ, 245, 357
- Zhang S., Chen Y., Collmar W. et al., 2008, ApJ, 683, 400
- Zwaan M.A., Verheijen M.A.W. & Briggs F.H., 1999, PASA, 16, 100

List of Figures

1.1	Modified figure, corresponding to the scheme of an AGN, as taken from Urry & Padovani 1995. The radio lobes are not shown in this picture.	12
1.2	Classification scheme for the AGNs based on radio and optical properties.	14
1.3	Spectral energy distribution (SED) of the Blazar 3C 279 in two different gamma-ray intensity states, from Hartmann et al. 2001.	17
1.4	Spectral energy distribution (SED) of a radio-quiet object (in red, Elvis et al. 1994) and of the Seyfert Galaxy Mrk 609 (black points) constructed from literature values (Polletta et al. 1996; Rudy et al. 1988). The values are compared with average SEDs from normal galaxies, starbusts and LINERs.	18
1.5	Broad-band X-ray spectrum of a Seyfert active galaxy.	22
1.6	Broad-band X-ray spectrum of a radio-loud active galaxy.	23
2.1	An example of the SED for blazar (the objects 3C 279, see http://heasarc.nasa.gov/docs/cgro/epo/posters/). The results shown in this plot summarize several multi-wavelength campaigns covering the frequency regions from the radio through the gamma-ray range observed by EGRET.	28
2.2	Representation of the physical interactions that give the non-thermal spectral features observed in the SED of the Blazar-type sources.	29
2.3	A phenomenological sequence discovered by Fossati and collaborators (1998) that shows that the values of the peak frequency are fixed by the radio luminosity: higher radio luminosity objects peak at lower frequencies.	32
3.1	An INTEGRAL payload modules view.	38
3.2	Schematic diagram of the a coded aperture camera working principle	40
3.3	IBIS coded mask patterns	42
4.1	The light curves (0.2–10 keV) of the sources observed with XMM-Newton MOS1 camera.	58

4.2	The light curves (0.2–10 keV) of the sources observed with Swift/XRT instruments.	58
4.3	The data to model <i>A</i> as obtained by fitting a simple power-law over the observed frame 3–100 keV and extrapolating over the 0.2–100 keV range.	63
4.4	The νF_ν plot (in keV cm ⁻² s ⁻¹) of the sources obtained by fitting the spectrum with a power-law and an intrinsic cold absorption in excess to the Galactic one. Left column, from top to bottom: 1ES0033+595, PKS2149-307, PKS0537-286 and BL Lac; right column, from top to bottom: IGRJ22517+2218, 3C279, QSOB0836+710 and SwiftJ1656-3302.	64
4.5	The νF_ν plot (in keV cm ⁻² s ⁻¹) of the sources obtained by fitting the spectrum with a broken power-law. Left column, from top to bottom: 1ES0033+595, PKS2149-307, PKS0537-286 and BL Lac; right column, from top to bottom: IGRJ22517+2218, 3C279, QSOB0836+710 and SwiftJ1656-3302.	65
4.6	The νF_ν plot of PKS 1830-211 obtained by fitting the spectrum with a broken power-law and an absorption associated to the lens galaxy ($z \sim 0.89$).	66
4.7	The νF_ν plot of 4C 04.42 obtained by fitting the spectrum with two different best-fit models: a broken power-law model (on the left) and a power-law model with a simple thermal emission of black-body (on the right).	70
4.8	The νF_ν plot of 3C 273 obtained by fitting the spectrum with a broken power-law model and a multi-temperature disk emission.	73
4.9	Distribution of the X-ray absorption column density (N_H) for our sample objects over the 0.2 – 100 keV energy range.	74
4.10	The N_H distributions of a sample of 16 RL objects observed in the 0.2 – 10 keV energy range from XMM-Newton.	75
4.11	The X-ray absorption column density N_H as a function of the redshift for our sample.	76
4.12	The X-ray absorption column density N_H as a function of the redshift, combining the results of our sources (empty red rhombs) and ones of a larger sample (blue plus and green cross signs) analyzed in the soft X-ray energy range.	76
4.13	Distribution of the power-law photon-index for our sample in the 0.2 – 100 keV energy range.	78
4.14	Distribution of the photon-index resulting by the analysis performed in the works of Page et al. (2005), Galbiati et al. (2005) and Yuan et al. (2006).	78
4.15	Photon-index distribution for the sources of the larger sample identified as Blazar.	79
4.16	Photon-index distribution for the sources of the larger sample identified as FSRQ.	79

5.1 Bulk Compton feature (Celotti, Ghisellini & Fabian 2007) 85

List of Tables

3.1	An overview of the IBIS scientific capabilities.	41
3.2	An overview of the SPI scientific capabilities.	43
3.3	An overview of the JEM-X scientific capabilities.	44
3.4	XMM-Newton and Swift/XRT parameters.	48
3.5	An overview of the Swift/BAT and INTEGRAL Surveys. . .	49
4.1	Most relevant information for the sample of blazars observed with INTEGRAL, Swift and XMM-Newton.	52
4.2	Information about the XMM-Newton observations and source observed count rates.	55
4.3	Information about the Swift/XRT observations and source observed count rates.	56
4.4	Best fit parameters of a simple power-law model in 3 – 100 keV energy range (model <i>A</i>).	61
4.5	Best fit parameters of an absorbed power-law model (model <i>B</i>). . .	67
4.6	Best fit parameters of a broken power-law model (model <i>C</i>). . . .	68
4.7	Best fit parameters of a broken power-law model with an absorption in excess for PKS 1830-211 (model <i>D</i>).	69
4.8	Best fit parameters of the models for 4C 04.42.	71
4.9	Best fit parameters of the models for 3C 273.	72